Changes in the El Niño-Southern Oscillation under climate regime shift and increased greenhouse gases

by

ZHENGQING YE

B.Sc., The Nanjing Institute of Meteorology, 1989

M.Sc., The Nanjing Institute of Meteorology, 1992

A THESIS SUBMITTED IN PARTIAL FULFILMENT OF

THE REQUIREMENTS FOR THE DEGREE OF

DOCTOR OF PHILOSOPHY

in

THE FACULTY OF GRADUATE STUDIES

(Oceanography)

The University of British Columbia

April, 2007

Abstract

The observed El Niño/Southern Oscillation (ENSO) has shown eastward displacements of the zonal wind stress anomalies and surface heat flux anomalies in the equatorial Pacific during El Niño episodes in the 1981-1995 regime relative to the 1961-1975 regime. Numerical experiments with a modified Zebiak-Cane intermediate complexity coupled model generally reproduced such displacements when the model climatological fields were replaced by the observed and simulated climatologies for the 1981-1995 regime. The later regime climatology resulted in eastward shifts in the ENSO system during El Niño but not La Niña, through the eastward shift of the atmosphere convergence heating rate in the coupled model. The ENSO period and ENSO predictability were also enhanced in the coupled model under the later regime climatology. A similar behavior was found in the Lorenz (1963) 3-component chaos system, i.e. in both the ENSO and Lorenz systems, stronger nonlinearity appears to lengthen the period thereby enhancing the predictability.

Using nonlinear principal component analysis, we demonstrated that the leading ENSO mode had changed on a physical basis since the late 1970s. The ENSO modes resembled the destabilized 'ocean basin mode' and 'the recharge-mode' in the pre- and post-1980s regimes, respectively. The surface zonal current acted as an intensifier of ENSO in the earlier regime and played a role in the transition of the ENSO cycle in the later regime.

With data from an ensemble of coupled general circulation models in the IPCC-AR4 project, climate under year 2000 greenhouse gas (GHG) level was compared with climate

under pre-industrial conditions. In the tropical Pacific, the warming in the mean sea surface temperatures (SST) was found to have an El Niño-like pattern, in agreement with the observed SST data (1900-1999). The models showed that both the equatorial zonal overturning circulation and the shallow meridional overturning circulation weakened under increased GHG forcing.

For ENSO, the asymmetry in the SST anomalies between El Niño and La Niña was found to be enhanced under increased GHG, for both the ensemble model data and the observed data. The enhanced asymmetry was mainly caused by the intensified vertical nonlinear dynamic heating. Furthermore, the enhanced GHG simulations showed that the asymmetry between El Niño and La Niña increased in the zonal wind stress anomalies, the equatorial undercurrent anomalies and the shallow meridional overturning circulation anomalies.

Table of Contents

List of Tables

List of Figures

List of Acronyms

ENSO El Niño/Southern Oscillation

EOF Empirical Orthogonal Function

ERSST Extended Reconstructed Sea Surface Temperature

GHG greenhouse gas

ICOADS International Comprehensive Ocean-Atmosphere Data Set

IPCC-AR4 the 4th Assessment Report of Intergovernmental Panel on Climate Change

MSE Mean Squared Error

NLCCA nonlinear canonical correlation analysis

NLPCA Nonlinear Principal Component Analysis

NN Neural Network

OCEE Oceanic Convergence zone - Eastern Edge

PCA Principal Component Analysis

PC Principal Component

PDF Probobility Density Function

SLP Sea Level Pressure

SST Sea Surface Temperature

WS Wind Stress

Acknowledgements

I would like to thank my supervisor Prof. William Hsieh for his help and guidance during the course of this work. Thanks are also due to Dr. Soon-Il An, who collaborated much of the work presented in Chapter 4. I am grateful to Dr. Stephen Zebiak for providing the Zebiak-Cane coupled model. As well, I am sincerely thankful for the constructive suggestion and comments from the members of my committee – Dr. Phil Austin and Dr. Rich Pawlowicz. I also acknowledge the modeling groups for providing their data for analysis, the Program for Climate Model Diagnosis and Intercomparison (PCMDI) for collecting and archiving the model output, and the JSC/CLIVAR Working Group on Coupled Modelling (WGCM) for organizing the model data analysis activity. The multi-model data archive is supported by the Office of Science, U.S. Department of Energy.

I thank Dr. Aiming Wu and Dr. Youmin Tang for many fruitful and stimulating discussions which greatly benefit the work.

Most of all, I would like to express my love and gratitude to my family. Without their understanding and support, it would be impossible for me to finish the thesis.

Chapter 1

Introduction

1.1 Scientific background: the physics of ENSO

The El Niño-Southern Oscillation (ENSO) phenomenon is the most important inter-annual component in the tropical atmosphere-ocean coupled system. It has important global effects on climate (Wallace and Gutzler, 1981). A better understanding of the ENSO physics could therefore have useful societal payoffs in addition to being a scientifically interesting problem.

Much progress has been made in ENSO theory and predictability (Neelin et al. 1998; Battisti et al, 1995; Latif et al. 1998) during the past decades. Several hypotheses about the ENSO mechanism have been proposed:

Bjerknes hypothesis:

The earliest hypothesis about an ENSO mechanism dates back to a theory of Bjerknes (Bjerknes, 1969). The essence of Bejerknes postulate is that the trade winds and zonal sea surface temperature (SST) affect each other in the tropical Pacific. A change towards a steeper (flatter) zonal pressure gradient strengthens (slackens) the Walker Circulation which results in an increase (decrease) of equatorial easterly winds. An increase (decrease) of equatorial easterly winds produces an increase (decrease) in upwelling at the eastern equatorial Pacific and hence provides for an increase (decrease) in east-west SST contrast which then strengthens (decrease) the zonal pressure gradient. This hypothesis is able to

describe the self-sustainment or growth in the warm or cold phase of ENSO. It cannot explain the turnabout between phases.

The canonical ENSO:

Another ENSO mechanism hypothesis, called the "canonical ENSO" by Cane (Cane, 1983), describes the different ENSO phases by summarizing a composite picture (Rasmusson and Carpenter, 1982). A canonical ENSO episode develops as follows:

The prelude stage: This stage includes a long period (more than 18 months) of "build-up" in the equatorial Pacific. During this period, stronger than normal easterly winds move the water from the eastern tropical Pacific to the western tropical Pacific. There also is a stronger than normal upwelling in eastern equatorial Pacific and hence a stronger than normal zonal SST gradient. The sea level increases in the western Pacific and decreases in the eastern Pacific. Thermocline at the equator is deepened in the western Pacific and depressed in the eastern Pacific.

The onset stage: The onset occurs during the boreal fall before a warm event. In this phase the rapid collapse of the easterly wind stress excites an equatorial Kelvin wave in September or October. The easterly wind stress is replaced by westerly wind stress in October or November, leading to a relaxation of the sea level slope.

The event stage: Warming off the coast of South America begins in December or January and continues on until June of the following year. Accompanying the positive SST anomalies in the central equatorial Pacific are large positive SST anomalies in the equatorial eastern Pacific area which reach their maxima in April, May or June. Positive SST anomalies extend westward or northwestward from the area off the coast of South America into the central equatorial Pacific in subsequent months. During this time sea level in the equatorial eastern Pacific is anomalously high and the westerly trade winds are intensified in the central

equatorial Pacific.

The mature stage: The positive SST anomalies concentrate on the central equatorial Pacific during the winter and reach their peaks. The mature phase is followed, one season later, by a rapid decline to cool SSTs , with the central Pacific cooling.

Delayed oscillator:

Delayed oscillator theory (Suarez and Schopf, 1988; Battisti and Hirst, 1989) explains the observed ENSO phenomena with Kelvin and Rossby Wave propagation across the Pacific. It assumes the strongest coupling between the wind stress anomaly and the equatorial SST pattern takes place in the central equatorial Pacific. An initial westerly wind stress anomaly induced by a positive SST perturbation in the central Pacific leads to the generation of an eastward propagating downwelling Kelvin wave with maximum signal on the equator and an upwelling Rossby wave with maximum signal symmetrically located on either side of the equator. The Kelvin wave causes the thermocline to deepen in the eastern equatorial Pacific, thereby increases the warming. In the meantime, the Rossby wave traveling westward is reflected off the western boundary as an upwelling Kelvin wave. The reflected upwelling Kelvin wave returns the SST and thermocline back to normal, terminating the warm event.

Western Pacific oscillator:

The western Pacific oscillator hypothesis (Weisberg and Wang, 1997) obviates the need for a reflecting weastern boundary by emphasizing the atmosphere-ocean interaction in the western Pacific. An initial westerly wind stress anomaly induced by a positive SST anomaly leads to off-equator cyclones in the western central equatorial Pacific. The westerly anomaly increases the thermocline depth and SST, resulting in positive feedback in the eastern and central equatorial Pacific. In the meantime, the enhanced westerly anomaly produces a high sea level pressure (SLP) over the western Pacific through Ekman pumping, hence

off-equator anti-cyclones appear in the western tropical Pacific. Then the off-equator anti-cyclones cause thermocline and SST to decrease in the western Pacific. As a result of the off-equator anti-cyclones, an equatorial easterly wind is generated in the western Pacific. The upwelling region initiated by the easterly wind evolves eastward along the equator, providing a negative feedback in the eastern equatorial Pacific area.

Recharge-discharge oscillator:

The recharge-discharge oscillator model does not emphasize the explicit role of wave propagation (Jin, 1997). The tropical Pacific heat content is of essential importance in the ENSO dynamical adjustment. The tropical subsurface ocean heat content is recharged after a mature ENSO cold phase and is discharged after a mature ENSO warm phase. An initial westerly anomaly wind stress induced by a SST anomaly in the western central equatorial Pacific leads to a positive SST anomaly and a positive thermocline depth anomaly in the central and eastern Pacific. Such a process involves a positive feedback between a westerly wind stress anomaly in the central equatorial Pacific and a positive SST anomaly in the central and eastern equatorial Pacific. The positive feedback continues until the ENSO oscillation develops into its mature warm phase. At the same time, the wind stress also gradually reduces the thermocline depth in the western Pacific, leading to a negative zonal mean thermocline depth anomaly across the Pacific. The tropical subsurface heat content is discharged during this period, and is only replenished when the ENSO oscillation develops into its mature cold phase.

Advective-reflective oscillator:

In this model (Picaut, 1997), an initial westerly wind anomaly drives a local zonal current that advects the oceanic convergence zone-eastern edge (OCEE) of the warm pool against the weaker mean zonal current. The eastward warm pool displacement decreases the

east-west SST gradient and strengthens the equatorial westerly wind anomaly. The positive feedback increases the SST in the eastern Pacific. ENSO is in its warm phase. At the same time, the westerly wind anomaly also excites Rossby waves and Kelvin waves. Downwelling Kelvin waves propagate eastward and upwelling Rossby waves propagate westward. There are three sets of currents in the equatorial Pacific. One set is generated by the Kelvin waves coming from the western boundary. One set is generated by the Rossby waves coming from the eastern boundary. Another set is the mean zonal current. The combination of currents in the equatorial Pacific stops the movement of the OCEE. Eventually, the OCEE moves westward and finally moves back toward the middle of the Pacific. Once the midpoint is crossed, the wind shifts from westerly to easterly and El Niño turns into La Niña; then La Niña turns into El Niño and the ENSO phases repeat indefinitely.

Unified oscillator:

The delayed oscillator, the western Pacific oscillator, the recharge-discharge oscillator, and the advective-reflective oscillator have previously been proposed to interpret the oscillatory nature of ENSO. Motivated by the existence of these different ENSO oscillators, Wang (Wang, 2001) developed a unified ENSO theory that includes the physics of the previous ENSO oscillators. In this model, if the western Pacific wind-forced response is neglected, thermocline and zonal wind stress anomalies in the western Pacific are decoupled from the coupled system, and the unified oscillator reduces to the delayed oscillator. If wave reflection at the western boundary is neglected, the unified oscillator reduces to the western Pacific oscillator. Most of the physics of the advective-reflective oscillator are implicitly included in the unified oscillator.

Linear system with the stochastic forcing:

Another theory assumes that the ENSO is generated by a damping linear system with

stochastic atmospheric forcings (Penland and Sardeshmukh, 1995; Moore and Kleeman, 1999; Thompson and Battisti, 2001). Thompson and Battisti (2001) stochastically forced a linear model that originally did not sustain internally generated variability and found that it reproduces all of the basic features of ENSO, suggesting that the essential characteristics of ENSO appear to be governed by linear processes.

1.2 ENSO decadal variability

Besides interannual variability, the Pacific Ocean has decadal/interdecadal climate variability, leading to long-term modulation of ENSO (Zhang et al, 1997; Wang and An, 2001; Rodgers et al, 2004). Zhang et al. (1997) argued that besides the well-known abrupt climate regime shifts towards a warmer tropical eastern Pacific and a colder extratropical central North Pacific in the mid 1970s, the global SST also has experienced an analogous shift during 1920s and an opposite polarity shift during the 1940s. The rebound of the climatological state in the Pacific Ocean since 1998 can be viewed as another opposite shift relative to the shift in the mid 1970s (McPhaden and Zhang, 2004). Like the interannual ENSO dynamics mentioned in the previous section, the fundamental dynamics of ENSO decadal variability is still not settled. We do not know what causes the ENSO decadal variability. The current literature includes a number of studies proposing mechanisms for this. The prevailing mechanisms for ENSO decadal variability can be separated into two broad categories: (1) tropical-extratropical interactions and (2) purely tropical processes. Within these two broad categories there are a number of competing hypotheses. For example, regarding the mechanism for the first category, there have been a number of studies emphasizing the importance of oceanic processes (Gu and Philander, 1997; Kleeman et al, 1999; McPhaden and Zhang, 2002). Atmospheric tropical-extratropical bridge processes

have also been considered as a potential mechanism for ENSO decadal variability (Barnett et al, 1999).

For the second category mechanism, some studies suggested that the decadal variability in the tropical Pacific can be generated by purely tropical nonlinear processes (Knutson and Manabe, 1998; Jin, 2001), while others proposed it comes from atmospheric noise and unrelated to low-frequency changes in the tropical Pacific mean state (Thompson and Battisti, 2001; Flügel et al, 2004).

Deser et al (2004) also examined the linkage between the tropical interdecadal variability and the interdecadal climate fluctuations over the North Pacific during boreal winter based on the analysis of a wide variety of observational datasets in the 20th century. Their study showed that the interdecadal variability over the tropical Pacific can impact the interdecadal variability over the North Pacific. Thus the interdedacal variability over the tropical Pacific and that over the North Pacific may influence each other.

1.3 Interdecadal ENSO nonlinearity and predictability

The topic of nonlinearity and predictability in ENSO has advanced significantly in recent years. Predicting the future state with a given initial state is a fundamental problem in climate research. The nonlinearity and predictability of ENSO is quite different in the numerical models at the decadal/interdecadal time scale (Ji et al, 1996; Chen et al, 2004). Chen et al (2004) made retrospective 148-year SST hindcasts using an intermediate coupled model with a specific lead time in the tropical Pacific. The model successfully predicted all prominent El Niño episodes within 148 years at a lead time up to 2 years. The predictability of the Nino3.4 index (averaged SST over 5°S-5°N, 170°W-120°W) varied decade by decade in their coupled model. An (2004) mentioned that the interdecadal change in the predictability

was related to the interdecadal change in ENSO asymmetry (between the warm El Niño and the cold La Niña states). Eccles and Tziperman (2004) found that the ENSO period was affected by ENSO's nonlinearity in a delayed oscillator model. They calculated the dependence of the ENSO period on its amplitude in both the strongly nonlinear regime and the weakly nonlinear regime. The ENSO period was found to decrease with increasing ENSO amplitude in the strongly nonlinear regime. In contrast, in the weakly nonlinear regime, the period tended to increase with the amplitude. They concluded that the weakly nonlinear case reflected "the dependence of the period on the ocean-atmosphere coupling strength rather than the dependence on the amplitude."

1.4 Response of ENSO to global warming

How ENSO responds to global warming is still an open question. Some climate models suggest that global warming will foster stronger and more frequent El Niños (Timmermann et al., 1999; Collins 2000). Collins (2000) argued that increased greenhouse gases may result in ENSO events becoming larger in amplitude and more frequent than present episodes in the climate model simulations based on version 2 of the Hadley Centre coupled model (HadCM2). However, in a subsequent analysis based on version 3 of the Hadley model (HadCM3), Collins et al (2005) found that he could not detect a change in magnitude or frequency of ENSO as greenhouse gases increased, thus contradicting the results of his earlier study. These differences highlight the level of uncertainty associated with ENSO under global warming.

On the other hand, the circulations associated with ENSO over the tropical Pacific has changed with global warming (Vecchi et al, 2006). McPhaden and Zhang (2002) also pointed out that the shallow meridional overturning circulation has slowed down in the

recent decades.

1.5 Objectives of the thesis

The first thesis objective is to investigate ENSO decadal/interdecadal variability and its possible cause in the tropical Pacific. As the tropical Pacific climatology is calculated from individual ENSO episodes, it is affected by changes in the properties of ENSO. On the other hand, does the climatology have an influence on the properties of individual ENSO episodes? Some studies have shown that ENSO properties such as the period and amplitude have changed with different climatologies. Fedorov and Philander (2001) found that the changes in the mean state played critical roles in determining the stability of the tropical ocean-atmosphere coupling modes. Their theoretical studies displayed the changes in ENSO properties caused by background changes in the wind stress intensity, thermocline depth and temperature difference across the thermocline. They concluded that the observed ENSO property changes since the 1960s were consistent with their theory.

In this thesis, how the climatological state impacts the ENSO characteristic properties is illustrated based on observational data and outputs from an intermediate coupled model. The nonlinearity and predictability of ENSO are investigated as well. The role of heat flux is examined in both the observational data and modeling results.

Next, the role of ocean surface current in ENSO is also studied under the 2 different climatological states (before and after the climate regime shift of the mid 1970s).

As aforementioned, ENSO changes its characteristic properties (such as the period, intensity, nonlinearity and predictability) on the decadal/interdecadal time scale. Our studies show that changes in the climatology can, at least in part, cause changes in the ENSO properties. The next step is to investigate the mean state change in the tropical Pacific due to

global warming. Thus the second objective of this thesis is to study how global warming affects the tropical mean state and ENSO properties.

The thesis is structured as follows: Chapter 2 illustrates the impact of regime shift in the mean state on ENSO properties (including predictability). Chapter 3 compared the nonlinearity and predictability in the ENSO system with that of the Lorenz (1963) nonlinear system. The role of surface currents in ENSO is discussed over the different climatological states based on the observed data in Chapter 4. The effects of increased greenhouse gas on ENSO and associated ocean circulations are shown in Chapter 5. Summary and discussion are given in Chaper 6.

1.6 References

Barnett T. P., D. W. Pierce, M. Latif, D. Dommenget and R. Saravanan, 1999: Interdecadal interactions between the tropics and midlatitudes in the Pacific basin. *Geophys. Res. Lett.*, 26, 615-618. DOI:10.1029/1999GL900042.

Battisti D. S., and A. C. Hirst, 1989: Interannual variability in the tropical atmosphere-ocean system: Influence of the basic state, ocean geometry, and nonlinearity, *J. Atmos. Sci.*, 46, 1687-1712.

Battisti D. S., and E. S. Sarachik, 1995: Understanding and predicting ENSO. *Rev. Geophys.*, (Suppl.), 1367-1376.

Bjerknes J., 1969: Atmospheric teleconnections from the equatorial Pacific, *Mon. Wea. Rev.*, 97, 163-172.

Cane M. A., 1983: Oceanographic events during El Niño, *Science*, 222, 1189-1195.

Chen D, M. A. Cane, A. Kaplan, S. E. Zebiak, and D. Huang, 2004: Predictability of El Niño in the past 148 years. *Nature* 428, 733-736.

Collins M., 2000: The El Niño Southern Oscillation in the second Hadley center coupled model and its response to greenhouse warming. *J. Climate*, 13, 1299-1312.

Collins M. and the CMIP Modelling Groups, 2005: El Niño- or La Niña-like climate change?. *Climate Dyn.*, 24, 89-104.

Deser C, A. S. Phillips and J. W. Hurrell, 2004: Pacific interdecadal climate variability: linkages between the Tropics and the North Pacific during boreal winter since 1900. *J. Climate*, 17, 3109-3124.

Eccles F. and E. Tziperman, 2004: Nonlinear effects on ENSO's period. *J. Atmos. Sci.*, 61, 474-482.

Fedorov A. V. and S. G. H. Philander, 2001: A stability analysis of tropical ocean-atmosphere interactions: Bridging measurements and theory for El Niño). *J. Climate*, 14, 3086-3101.

Flügel M., P. Chang and C. Penland, 2004: The role of stochastic forcing in modulating ENSO predictability. *J. Climate*, 17, 3125-3140.

Gu D. and S. G. H. Philander, 1997: Interdecadal climate fluctuations that depend on exchanges between the tropics and extratropics. *Science*, 275, 805-807.

Ji M., A. Leetmaa and V. E. Kousky, 1996: Coupled model predictions of ENSO during the 1980s and the 1990s at the National Centers for Environmental Prediction, *J. Climate*, 9, 3105-3120.

Jin F.-F., 1997: An Equatorial Ocean Recharge Paradigm for ENSO Part I: Conceptual Model, *J. Atmos. Sci.*, 54, 811-829.

Jin F.-F., 2001: Low-frequency modes of tropical ocean dynamics, *J. Clim.*, 14, 3874-3881.

Kleeman R., J. P. McCreary and B. A. Klinger, 1999: A mechanism for generating ENSO decadal variability. *Geophys. Res. Lett.*, 26, 1743-1746.

Knutson T. R. and S. Manabe, 1998: Model assessment of decadal variability and trends in the tropical Pacific Ocean. *J. Climate*, 11, 2273-2296.

Latif M., and T. P. Barnett, 1996: Decadal climate variability over the North Pacific and North America: Dynamics and predictability. *J. Climate*, 9, 2407-2423.

Latif M., D. Anderson, T. P. Barnett, M. A. Cane, R. Kleeman, A. Leetmaa, J. J. O'Brien, A. Rostati, and E. K. Schneider, 1998: Predictability and Prediction. *J. Geophys. Res.*, 103, 14375-14394.

McPhaden M. J., and D. Zhang, 2002: Slowdown of the meridional verturning circulation in the upper Pacific Ocean. *Nature*, 415, 606-608.

McPhaden M. J. and D. Zhang, 2004: Pacific Ocean circulation rebounds, *Geophys. Res. Lett.*, 31, L18301. DOI:10.1029/2004GL020727.

Moore A. M. and R. Kleeman, 1999: Stochastic forcing of ENSO by the intraseasonal oscillation. *J. Climate* 12, 1199-1220.

Neelin J. D., D. S. Battisti, A. C. Hirst, F.-F. Jin, Y. Wakata, T. Yamagata, and S. E. Zebiak, 1998: ENSO theory. *J. Geophys. Res.*, 103, 14261-14292.

Penland C. and P. D. Sardeshmukh, 1995: The optimal-growth of tropical sea-surface temperature anomalies, *J. Climate*, 8, 1999-2024.

Picaut J., F. Masia, Y. Dupenhoat, 1997: An advective-reflective conceptual-model for the oscillatory nature of the ENSO, *Science*, 277, 663-666. DOI:10.1126/science.277.5326.663.

Rasmusson E. M. and T. H. Carpenter, 1982: Variations in tropical sea surface temperature and surface wind fields associated with the Southern Oscillation/El Niño, *Mon. Wea. Rev.*, 110, 345-384.

Rodgers K. B., P. Friederichs and M. Latif, 2004: Tropical Pacific decadal variability and its relation to decadal modulations of ENSO. *J. Climate*, 17, 3761-3774.

Suarez M. J. and P. S. Schopf, 1988: A delayed action oscillator for ENSO, *J. Atmos. Sci.*, 45, 3283-3287.

Thompson C. J. and D. S. Battisti, 2001: A linear stochastic dynamical model of ENSO. Part II: Analysis. *J. Climate* 14, 445-466.

Timmermann A, Oberhuber, J., Bacher, A., Esch, M., Latif, M. and Roeckner, E. 1999: Increased El Niño frequency in a climate model forced by future greenhouse warming. *Nature*, 398, 694-696.

Vecchi G. A., B. J. Soden, A. T. Wittenberg, I. M. Held, A. Leetmaa and M. J. Harrison, 2006: Weakening of tropical Pacific atmospheric circulation due to anthropogenic forcing. *Nature*, 44, 73-76.

Wallace J. M. and D. S. Gutzler, 1981: Teleconnections in the geopotential height field during the Northern Hemisphere winter. *Mon. Wea. Rev.*, 109, 784-812.

Wang B. and S.-I. An, 2001: Why the properties of El Niño changed during the late 1970s. *Geophys. Res. Lett.*, 28, 3709-3712.

Wang C., 2001: A unified oscillator model for the El Niño-Southern Oscillation, *J. Climate*, 14, 98-115.

Weisberg R. H., C. Wang, 1997: A western Pacific oscillator paradigm for the El Niño–Southern Oscillation. *Geophys. Res. Lett.*, 24, 779-782.

Zhang Y, J. M. Wallace and D. S. Battisti, 1997: ENSO-like interdecadal variability: 1900-93. *J. Climate*, 10, 1004-1020.

Chapter 2

The Influence of Climate Regime Shift on ENSO [1]

2.1 Introduction

The characteristics of the El Niño/Southern Oscillation (ENSO) have experienced an abrupt change or 'regime shift' in the mid 1970s, which is usually attributed to decadal/interdecadal climate variability in the Pacific Ocean (Zhang et al, 1997, Wang and An, 2001). Recent studies (McPhaden and Zhang, 2004) found that the Pacific Ocean has rebounded since 1998, where the rebound can be viewed as an opposite shift relative to the shift in the mid 1970s. There is no consensus on the fundamental dynamics of ENSO decadal variability. Some modeling results suggested that the decadal variability in the tropical Pacific originates from mid-latitude variability (Latif and Barnett, 1996), while others proposed it comes from tropical internal nonlinear instability (Knutson and Manabe, 1998) or uncoupled atmospheric noise (Thompson and Battisti, 2001; Flügel et al, 2004). Two hypotheses have been proposed to explain the linkage between the extratropical decadal variability and the tropical decadal variability, one by an oceanic teleconnection pathway (Gu and Philander, 1997; Kleeman et al, 1999), the other by an atmospheric bridge (Barnett et al, 1999).

[1] A version of this chapter has been published. Ye, Z. and Hsieh, W. W. (2006) The influence of climate regime shift on ENSO. *Climate Dyn.*, 26: 823-833. DOI:10.1007/s00382-005-0105-5.

Since a decadal/interdecadal change in the tropical Pacific amounts to a change in the background mean state for the ENSO phenomenon, how the background state affects ENSO properties has become an area of active investigation. Studies have shown that changes in the background state would alter ENSO in period, intensity, direction of propagation and spatial structure. For instance, Fedorov and Philander (2001) studied theoretically the changes in ENSO properties caused by background changes in the wind stress intensity, thermocline depth and temperature difference across the thermocline, and concluded that the observed ENSO property changes since the 1960s are consistent with their theory. Wang and An (2002) proposed that the changes in the background winds and the corresponding ocean dynamic fields played the dominant role in the abrupt change in ENSO properties since the late 1970s. A caveat is that the periods used to calculate the mean states are relatively short, and the presence of an extra El Niño or a very strong El Niño during a particular decadal period could introduce a difference in the calculated mean states, i.e. the mean decadal states are themselves influenced by ENSO episodes.

Recently, the nonlinearity and asymmetry of decadal variability in the tropical Pacific were recognized (Rodgers, 2004). Jin et al (2003) suggested that nonlinear dynamic heating in the tropical Pacific ocean heat budget is essential in generating the nonlinearity and asymmetry of the decadal-scale ENSO. Changes in the asymmetry and nonlinearity of ENSO over different climate regimes have also been studied. Wu and Hsieh (2003) examined that the leading nonlinear canonical correlation analysis (NLCCA) mode between the tropical Pacific sea surface temperature (SST) and wind stress (WS), which showed that after the climate regime shift of the mid 1970s, there was an eastward shift in the westerly anomalies during warm ENSO episodes, but no shift in the easterly anomalies during the cold ENSO episodes, thereby enhancing the asymmetry between El Niño and La Niña in the post-shift

regime compared to the pre-shift regime. ENSO predictability has been found to be higher during the decades when the ENSO asymmetry is large (An, 2004).

In this chapter, by analyzing a coupled model of intermediate complexity and observed data, we investigate how changes in the background climate state affect properties of ENSO, especially the asymmetry between El Niño and La Niña, zonal shifts in the observed net shortwave radiation flux and latent heat flux, shifts in the model convergent heating rate, and ENSO predictability. This chapter is organized as follows: In Section 2.2, we introduce the datasets and the nonlinear data analysis method. Section 2.3 describes the revised coupled model. In Section 2.4, observed data are first analyzed for the 'regime shift' in the asymmetry of ENSO, then the intermediate coupled model is run to see how different background states (of surface wind, heat fluxes, and sea surface temperatures) change the ENSO properties. A discussion follows in Section 2.5.

2.2 Data and methods

2.2.1 Data

The National Oceanic and Atmospheric Administration (NOAA) extended reconstructed SST dataset was used in this study. The extended reconstructed sea surface temperature (ERSST) was constructed using the most recently available international comprehensive ocean-atmosphere data set (ICOADS) SST data and improved statistical methods that allow stable reconstruction using sparse data. This monthly analysis begins in January 1854, but because of sparse data the analyzed signal was heavily damped before 1880 (Smith and Reynolds, 2004). The monthly WS was objectively analyzed at Florida State University (Bourassa et al, 2001), while the sea surface heat flux data is from da Silva et al

(1994) (which terminated after 1993). The climatological monthly mean was removed from the data to obtain the monthly anomaly.

2.2.2 Nonlinear principal component analysis

For the time series data $\mathbf{x}(t) = [x_1, ..., x_l]$, where each variable x_i is a time series containing n observations, the principal components analysis (PCA) method looks for u, a linear combination of the x_i, and an associated vector $\mathbf{a}$, with

$$u(t) = \mathbf{a} \cdot \mathbf{x}(t)$$

so that

$$J = \left\langle \|\mathbf{x}(t) - \mathbf{a}u(t)\|^2 \right\rangle$$

is minimized. Here $\langle ... \rangle$ denotes a sample or time mean, u, the first principal component (PC), is a time series, while $\mathbf{a}$, the first empirical orthogonal function (EOF), describes a spatial pattern.

The fundamental difference between nonlinear principal components analysis (NLPCA) and PCA is that NLPCA allows a nonlinear mapping from $\mathbf{x}$ to u and a nonlinear inverse mapping from u to $\mathbf{x}'$, whereas PCA only allows linear mapping (Kramer, 1991; Hsieh, 2004). For NLPCA,

$$u = F(\mathbf{x}), \quad \mathbf{x}' = \mathbf{G}(u)\,,$$

where F and $\mathbf{G}$ denote the nonlinear mapping and inverse mapping functions respectively (Fig. 2.1). For more details, see Appendix B.

The NLPCA method is used to analyze the nonlinear modes of SST and WS in the tropical Pacific. Prior to NLPCA, combined PCA, also called combined EOF analysis,

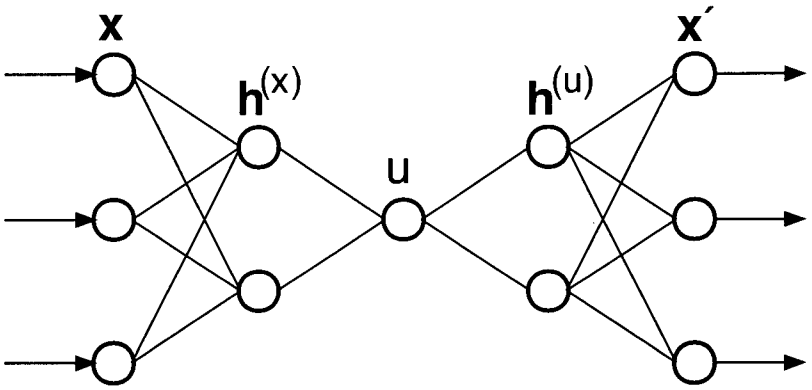

Figure 2.1: A schematic diagram illustrating the neural network(NN) model for performing the NLPCA. The model is a standard feedforward NN (i.e. multi-layer perceptron) (Bishop, 1995), with 3 'hidden' layers of variables or 'neurons' (denoted by circles) sandwiched between the input layer $\mathbf{x}$ on the left and the output layer $\mathbf{x}'$ on the right. Next to the input layer is the encoding layer, followed by the 'bottleneck' layer with a single neuron u, then the decoding layer, and finally the output layer, i.e. a total of 4 layers of transfer functions are needed to map from the inputs to the outputs. A neuron v_i at the ith layer receives its value from the neurons $\mathbf{v}_{i-1}$ in the preceding layer, i.e. $v_i = f_i(\mathbf{w}_i \cdot \mathbf{v}_{i-1} + b)$, where $\mathbf{w}_i$ is a vector of weight parameters and b a bias parameter, and the transfer functions f_1 and f_3 are the hyperbolic tangent functions, while f_2 and f_4 are simply the identity functions. Effectively, a nonlinear function $u = F(\mathbf{x})$ maps from the higher dimension input space to the lower dimension bottleneck space, followed by an inverse transform $\mathbf{x}' = \mathbf{G}(u)$ mapping from the bottleneck space back to the original space, as represented by the outputs. To make the outputs as close to the inputs as possible, the cost function $J = \langle \|\mathbf{x} - \mathbf{x}'\|^2 \rangle$ (i.e. the mean square error, MSE) is minimized. Through the optimization, the values of the weight and bias parameters are solved. See Appendix B for details.

is performed on the SST and WS anomalies in order to reduce the data dimension – we performed PCA analysis on the combined field of SST anomalies and WS anomalies, with each variable first normalized by its standard deviation, then, the leading 6 PCs are used as the inputs to the NLPCA model, which finds a curve in the 6-dimensional PC space.

2.3 Coupled model

The coupled model is based on the Zebiak-Cane model (Zebiak and Cane, 1987), where the atmospheric component consists of steady-state, linear shallow-water equations on an equatorial beta plane with a nonlinear convergence feedback, while the oceanic component is a linear reduced-gravity model (see Appendix A for details). With a time step of (about) 10 days, the ocean model domain covers the tropical Pacific from 29°S to 29°N, and from 124°E to 80°W, where the grid for ocean dynamics is 2° longitude by 0.5° latitude, and the grid for SST physics and the atmospheric model is 5.625° longitude by 2° latitude.

The temperature equation for the surface layer follows Zebiak and Cane (1987):

$$\begin{aligned}\frac{\partial T}{\partial t} &= -\mathbf{u}_1 \cdot \nabla(\overline{T}+T) - \overline{\mathbf{u}}_1 \cdot \nabla T - \{M(\overline{w}_s + w_s) - M(\overline{w}_s)\} \times \frac{\partial \overline{T}}{\partial z} \\ &\quad -M(\overline{w}_s + w_s)\frac{T-T_e}{H_1} - \alpha_s T - K_t \frac{T-T_e}{H_1} + A_h \triangle_h T\,, \end{aligned} \tag{2.1}$$

where we have added the last two terms to simulate vertical mixing and horizontal diffusion in the temperature equation (Boulanger and Menkes, 2001). Here $\overline{\mathbf{u}}_1(x,y,t)$ and $\overline{w}_s(x,y,t)$ are the prescribed climatological monthly mean horizontal current and upwelling in the surface layer respectively, $\overline{T}(x,y,t)$ is the prescribed mean SST, $\partial\overline{T}(x)/\partial z$ the prescribed mean vertical temperature gradient, the mean surface layer depth $H_1 = 50$ m, the diffusion coefficient $\alpha_s = (125 \text{ day})^{-1}$, $K_t = 2.5 \times 10^{-5}\text{m s}^{-1}$, $A_h = 2000\text{m}^2\text{s}^{-1}$, the function M is

defined by

$$M(x) = \begin{cases} 0, & x \leq 0 \\ x, & x > 0\,, \end{cases} \tag{2.2}$$

and the entrainment velocity is

$$w_s = H_1(\frac{\partial u_1}{\partial x} + \frac{\partial v_1}{\partial y})\,. \tag{2.3}$$

The entrainment temperature anomaly, T_e, is given by

$$T_e = \gamma T_{\text{sub}} + (1-\gamma)T\,, \tag{2.4}$$

The subsurface temperature anomaly T_{sub} is assumed to arise from depressing or raising the thermocline according to the anomalous inflow or outflow of mass in the upper layer. This corresponds roughly to considering vertical displacements of the mean subsurface temperature profile in accordance with the anomaly in the upper layer depth. To quantify this, the mean vertical temperature profile is approximated by the analytic form of a hyperbolic tangent function. Thus, T_{sub} originally has the empirical parameterization form (Zebiak and Cane, 1987) :

$$T_{\text{sub}} = \begin{cases} T_1 \left\{\tanh[b_1(\overline{h}+h)] - \tanh(b_1\overline{h})\right\}, & h > 0 \\ T_2 \left\{\tanh[b_2(\overline{h}-h)] - \tanh(b_2\overline{h})\right\}, & h < 0 \end{cases} \tag{2.5}$$

with $\overline{h}(x)$ the prescribed mean upper layer depth, $\gamma = 0.75$, $T_1 = 28°\text{C}$, $T_2 = -40°\text{C}$, $b_1 = (80\text{ m})^{-1}$ and $b_2 = (33\text{ m})^{-1}$.

Here an empirical parameterization scheme was developed to estimate T_{sub} in terms of other ocean dynamical variables in the temperature equation (2.1). With the ocean model forced by the observed WS during 1964-1998, The equation (2.1) was inverted for T_{sub} using the observed SST for T and the model anomalous currents (Zhang et al, 2005). PCA was separately applied to the simulated upper layer depth anomalies h, and to T_{sub} to extract

the leading PCs. The nonlinear regression relationships between the first three PCs of h (the predictors) and the first three PCs of T_{sub} (the predictands) were obtained by a neural network method (Tang and Hsieh, 2002; Li et al, 2005). Then the nonlinear regression relationships were used to replace equation (2.5) in the coupled model. Nonlinear relations between the leading PCs of T_{sub} and those of h can be seen in Fig. 2.2. Li et al (2006) found that the nonlinear regression was better than the linear regression, although Fig. 2.2 does not exhibit strong nonlinear relationship between h and T_{sub}. The nonlinear regression improves the SST simulation in the coupled model.

The observed SST averaged in equatorial area (5°S-5°N) showed that during almost each El Niño between 1960-2000 the warm maximum SST anomalies occupied the whole eastern Pacific. The El Niño of 1997/1998 was the only one where the maximum SST anomalies were located in the eastern boundary area (Fig. 2.3). During La Niña, the observed minimum SST anomalies were located further west than the maximum SST anomalies during El Niño.

Fig. 2.4 gives an example of the simulated SST and WS anomalies during model years 280-300 in the coupled model to compare the original parameterization with the new one. The simulated SST anomalies in the equatorial area (5°S-5°N) were always manifested mainly in the eastern area in the original coupled model during both El Niño and La Niña (Fig. 2.4b). However, the simulated maximum SST anomalies for the new parameterization extended much further west into the central equatorial Pacific (Fig. 2.4d), close to the observations (Fig. 2.3). The maximum westerly WS anomalies (Fig. 2.4a) for the original parameterization were located around 160°W-140°W during El Niño, exhibiting an eastward shift relative to the observed WS anomalies located around 180°W-160°W (not shown). Under the new parameterization, the model maximum WS has shifted to the correct location of 180°W-160°W during El Niño (Fig. 2.4c). The negative (i.e. easterly) WS anomalies

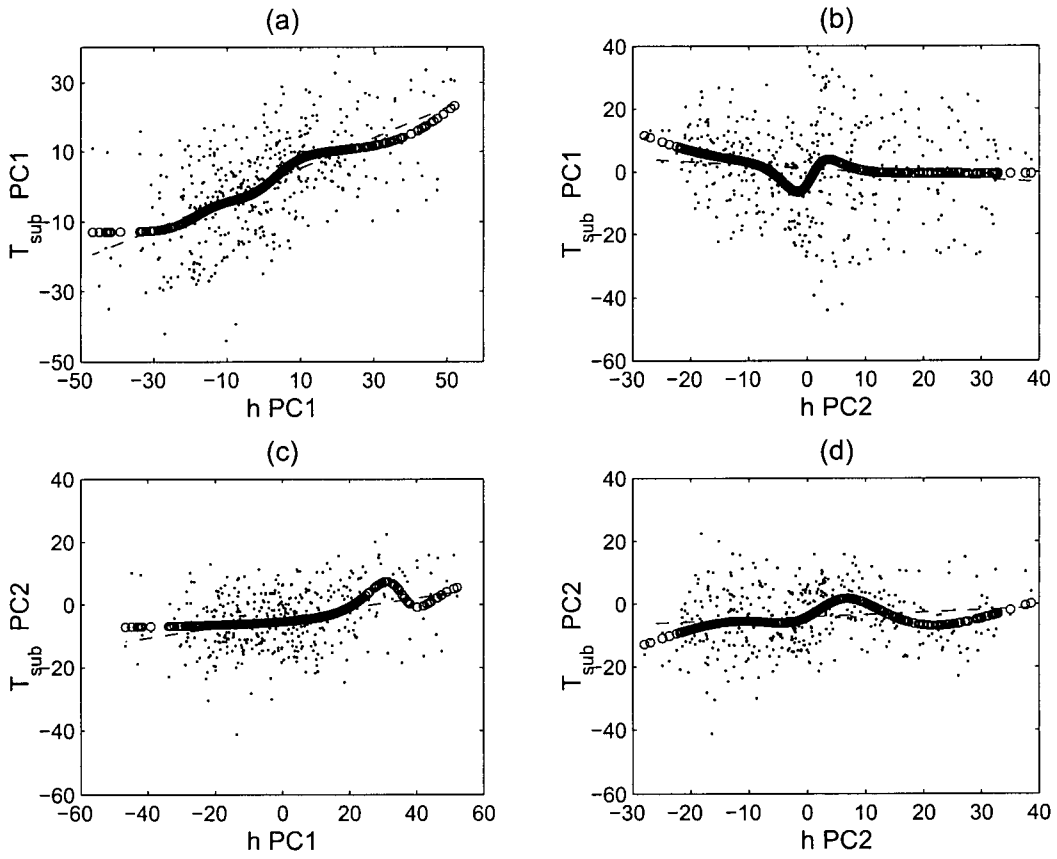

Figure 2.2: Relations between PC1 of the T_{sub} anomalies and (a) PC1 and (b) PC2 of the h anomalies, as found by nonlinear regression via neural networks (overlapping circles), and linear regression (dashed lines), with the data shown as dots. The corresponding relations for PC2 of the T_{sub} anomalies are shown in (c) and (d).

in the model with the new parameterization have also strengthened and shifted westward compared to the original parameterization (2.4a and c). Thus the new parameterization has corrected the original coupled model bias where the variability (for both SST and WS) was located too far east. Note that there are unrealistic significant easterly wind stress anomalies in the equatorial area near 130°W in the model with the new parameterization. Such easterly wind stress anomalies are absent in the observations (Deser and Wallace, 1990). These spurious anomalies of zonal wind are a known problem of the Gill atmospheric model that ties atmospheric heating too closely to SST anomalies.

To analyze the cause of shifts in SST and WS anomalies in the new coupled model, both the simulated subsurface temperature and thermocline anomalies with the original and the new parameterization in the coupled model are shown in Fig. 2.5. In the new coupled model, the thermocline depth anomalies extend further west during El Niño than in the original model (2.5a and c). The maximum thermocline anomalies were located between longitude 180° and 120°W under the new parameterization. The corresponding positive subsurface temperature anomalies extended to the central equatorial Pacific (Fig. 2.5d), whereas in the original model, the maximum subsurface temperature anomalies appeared further east during El Niño with double the amplitude. The change in subsurface temperature simulation in the new model led to the better SST simulation in the coupled model, since the subsurface temperature directly affected the SST via the upwelling in the eastern equatorial Pacific.

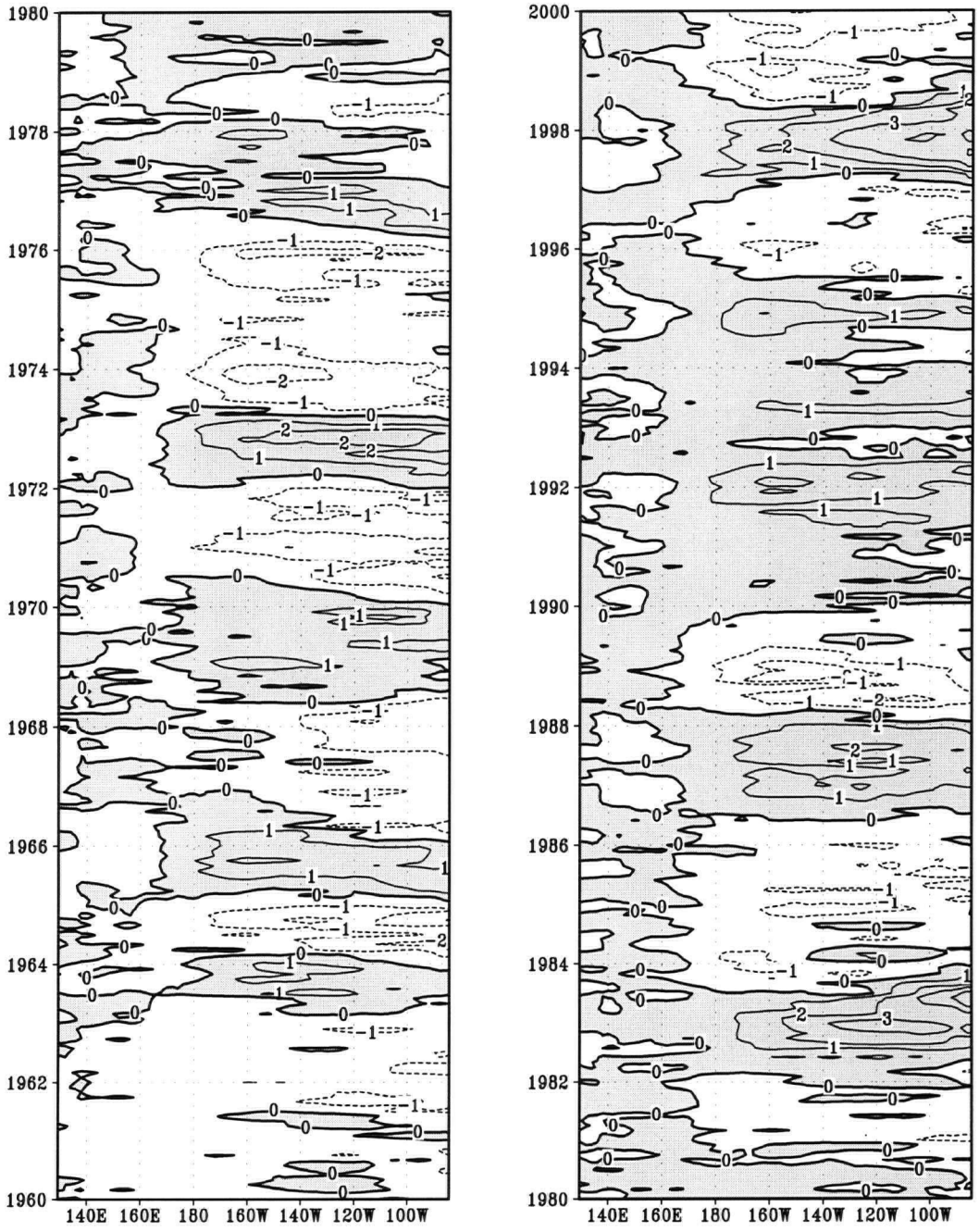

Figure 2.3: Observed SST (°C) anomalies along equator (averaged in 5°S-5°N). The contour interval is 1 °C with positive values shaded.

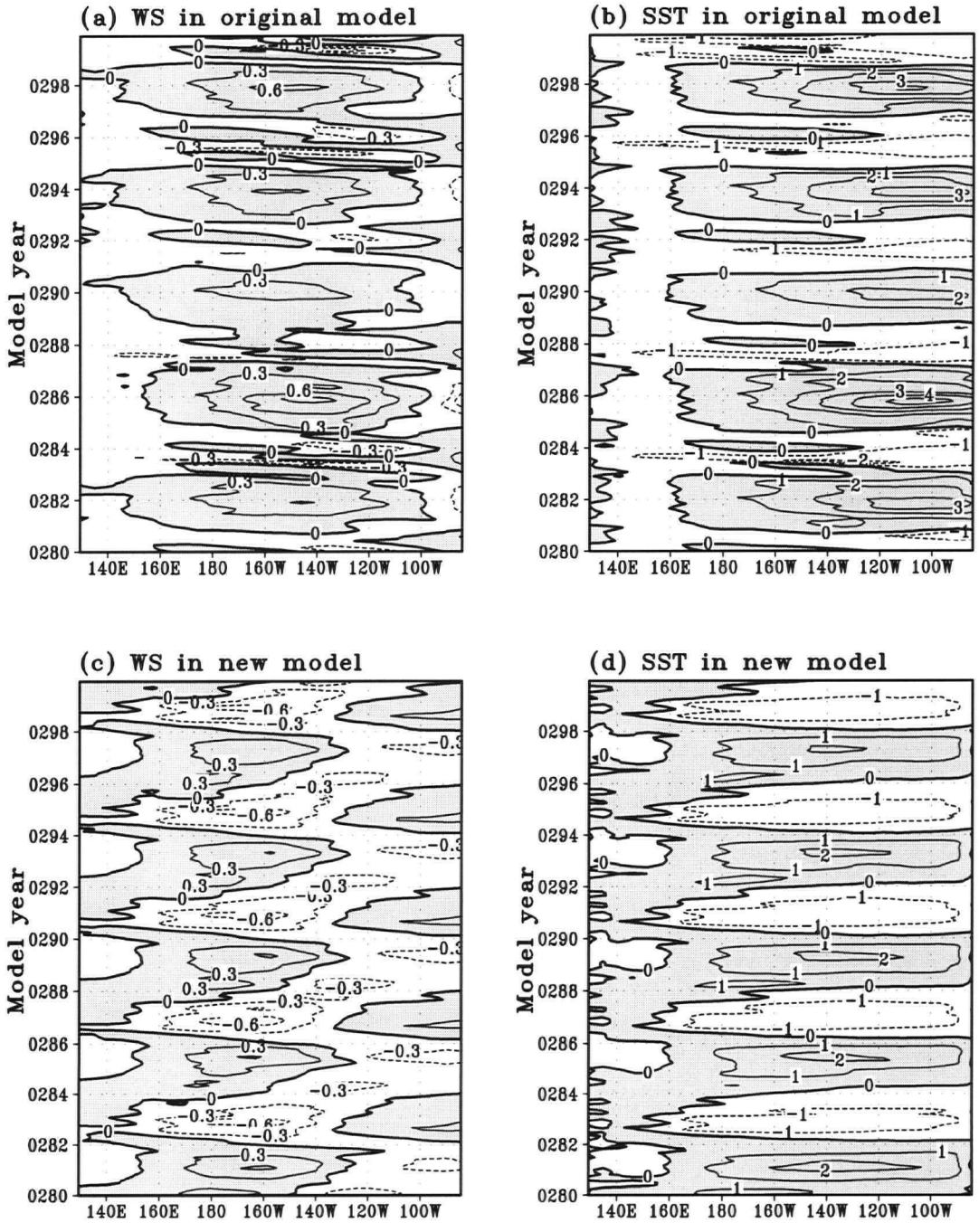

Figure 2.4: Zonal WS (dyn cm^{-2}) and SST (°C) anomalies along the equator (averaged over 5°S-5°N) in the coupled model from the original model (top panels) and the new model with the neural network parameterization (bottom panels). Positive values are shaded.

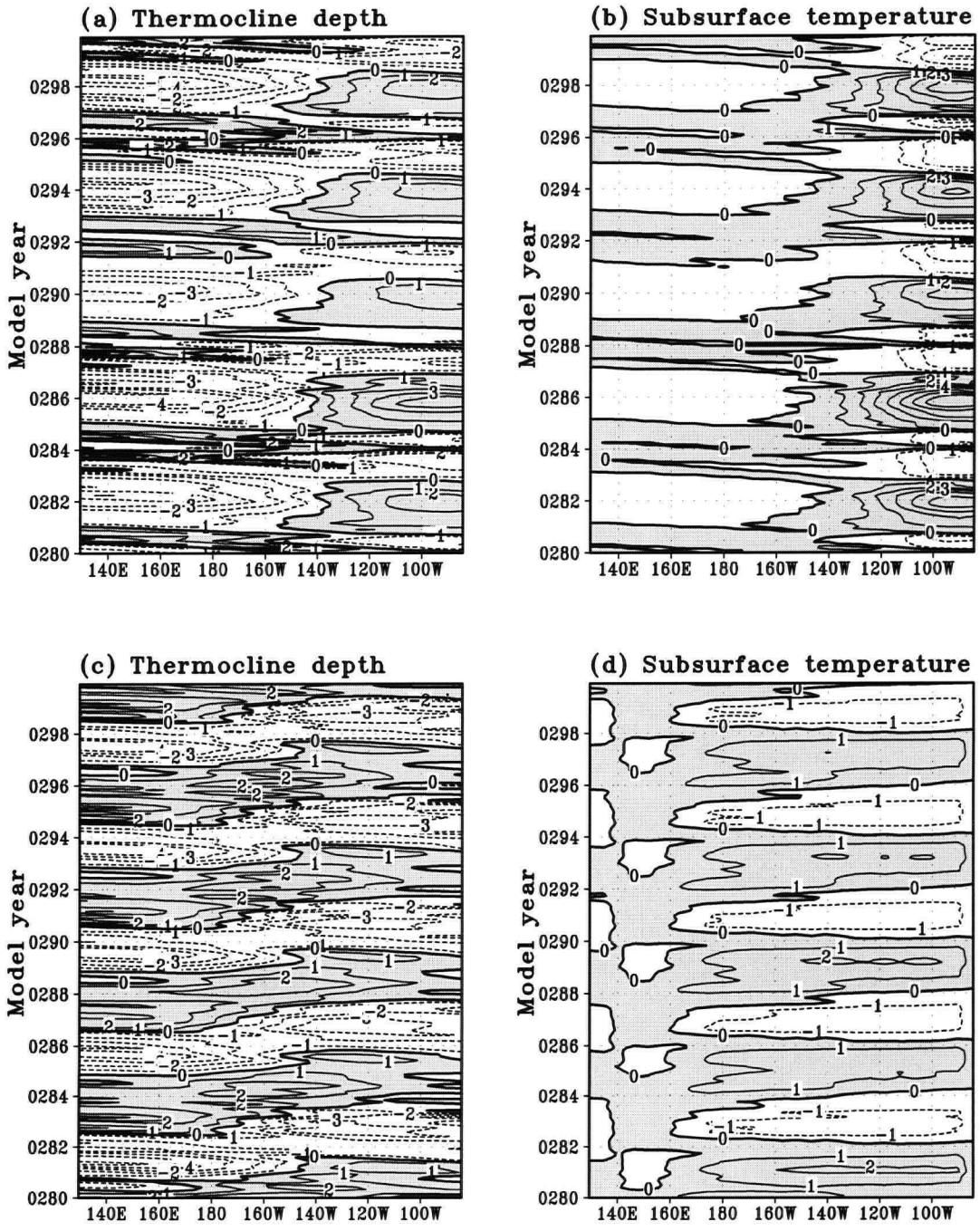

Figure 2.5: Thermocline depth (10 m) and the T_{sub} (°C) anomalies in the coupled model along the equator (averaged over 5°S-5°N) from the original model (top panels) and the new model (bottom panels). Positive values are shaded.

2.4 Results

2.4.1 Observational results

A shift in the ENSO properties, both atmospheric and oceanic, occurred in the mid 1970s (Zhang et al, 1997; An and Wang, 2000). Decadal differences in the SST and the surface WS field were calculated by subtracting the 1961-1975 mean from the 1981-1995 mean (Fig. 2.6). In the SST field (Fig. 2.6a), the decadal difference exhibits an ENSO-like pattern over the tropical Pacific. In the WS field, there are decadal westerly anomalies over the western equatorial Pacific and easterly anomalies over the eastern equatorial Pacific, resulting in a convergence region in the central equatorial Pacific (Fig. 2.6b).

Next, the NLPCA method was applied to analyze the observed tropical Pacific SST anomaly and WS anomaly during the 1961-1975 regime, and separately, the 1981-1995 regime. The 6 leading PCs of the combined PCA of the SST field and WS field were used as the inputs to the NLPCA model. NLPCA shows that there is an eastward shift by over 15° in the westerly WS anomaly field (associated with El Niño episodes) in the central equatorial Pacific in 1981-1995 regime (Fig. 2.7c) compared to that in 1961-1975 regime (Fig. 2.7a). However, there is no obvious zonal shift in the easterly WS anomaly field (associated with La Niña) in the central equatorial Pacific between the two regimes (Figs. 2.7b and d). The amplitudes of both the westerly and easterly WS were intensified during the 1981-1995 regime. These results are similar to the results found by using NLCCA on SST and WS fields in the 1961-1975 and 1981-1999 regimes (Wu and Hsieh, 2003).

The surface heat fluxes are also analyzed using the NLPCA. The 6 leading PCs of the combined PCA of the SST, net shortwave radiation and latent heat flux fields (with each field variable normalized by its standard deviation) are used as the inputs to the NLPCA

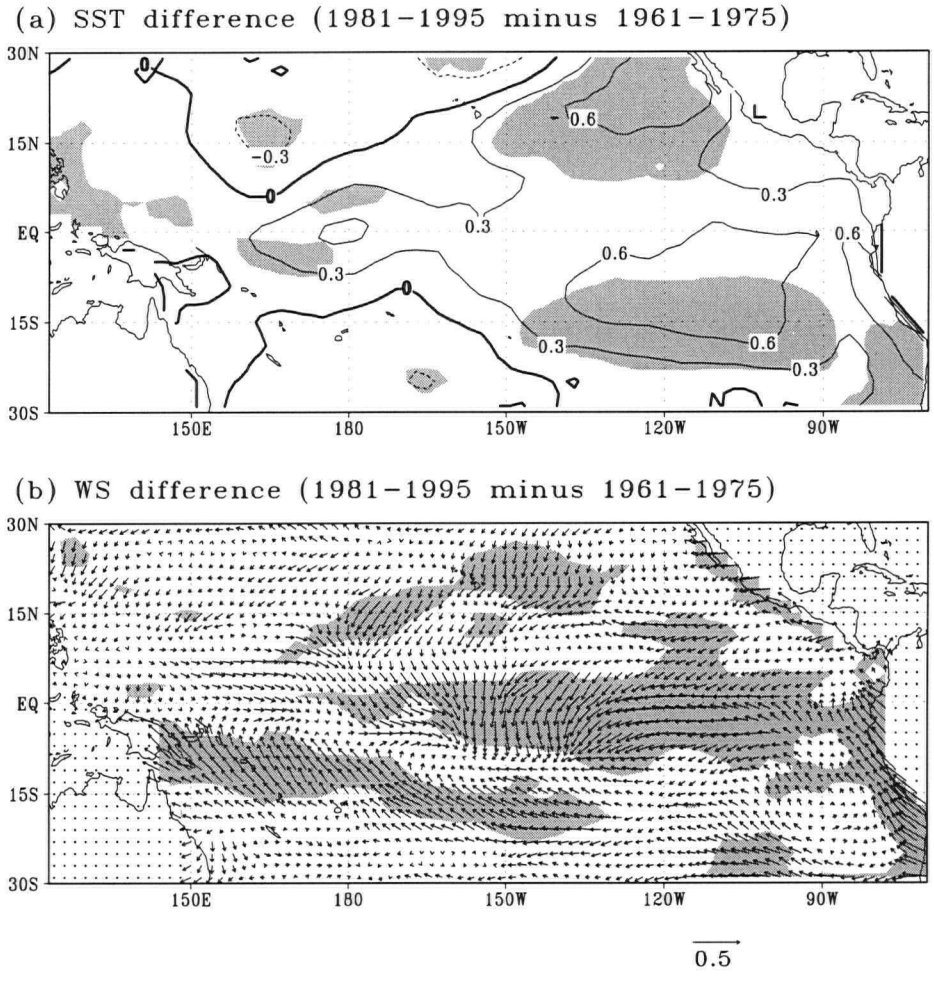

Figure 2.6: The decadal differences in the (a) SST (°C) and (b) WS (dyn cm^{-2}) over the tropical Pacific. Shaded regions indicate 95% significance by the corrected t test (Zwiers and Von Storch, 1995).

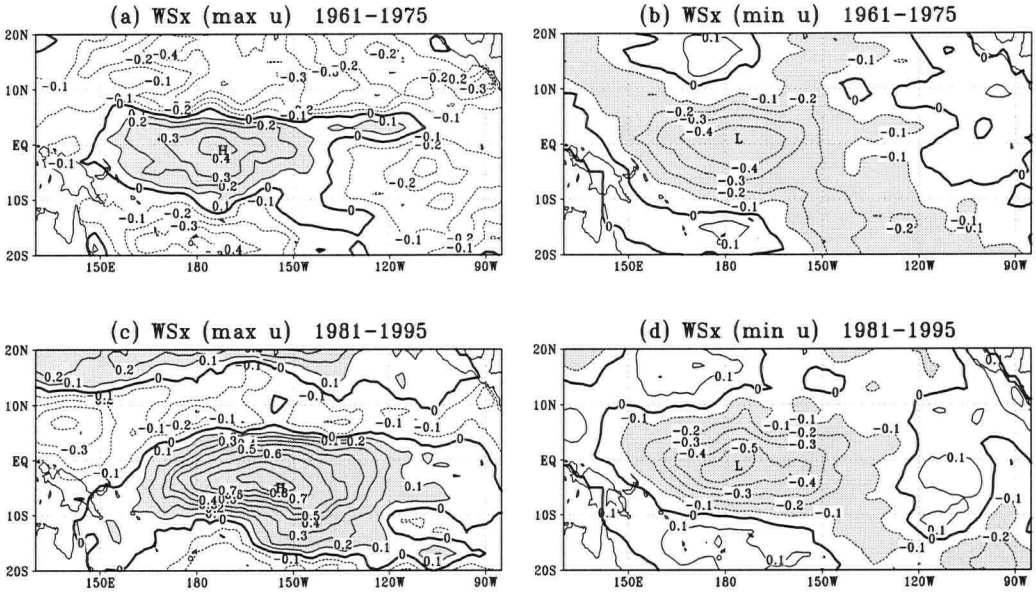

Figure 2.7: The observed zonal wind stress WSx (dyn cm^{-2}) anomaly patterns from the leading NLPCA mode for the 1961-1975 regime ((a) and (b)) and for the 1981-1995 regime ((c) and (d)), with panels in the left column showing the anomalies when the NLPC u assumes its maximum value (i.e. during strong El Niño), and the right column, the minimum value (strong La Niña). Regions with values greater than 0.1 dyn cm^{-2} or less than -0.1 dyn cm^{-2} are shaded. "L" and "H" mark the location of the lowest and highest values, respectively.

model. Similar eastward shifts (associated with El Niño episodes) can be seen in the net shortwave radiation field and, to a lesser extent, in the latent heat flux field in the later regime compared to the earlier regime. (Fig. 2.8). The eastward shift of the net shortwave radiation is the result of eastward shift of tropical clouds over the Pacific during El Niño episodes in the later regime. Similar shifts are also found in the composite maps of the net shortwave radiation field or the latent heat flux field for El Niño episodes in the two regimes (not shown). Hence the net shortwave radiation and latent heat flux fields together with the SST and zonal WS displayed greater asymmetry between El Niño and La Niña during the later regime as a result of the eastward shift in the anomalies during El Niño but not during La Niña. However, similar analyses on the net longwave radiation field and the sensible heat flux field did not reveal significant shifts in the later regime (not shown).

That the net shortwave radiation and latent heat flux fields appeared to shift eastward during El Niño in the post-shift regime, could be caused by the warmer and eastward-shifted SST anomalies over the eastern tropical Pacific in the post-shift regime during El Niño (Wu and Hsieh, 2003). The warmer and shifted SST anomalies would cause the convection and clouds to move eastward in the later regime during El Niño. Thus the surface latent heat flux related to the convection tends to shift eastward during El Niño. The surface net radiation flux also tends to shift eastward since the clouds reflect the solar (shortwave) radiation back into space. However, it is more complicated for the warmer and shifted SST anomalies to affect the net longwave radiation flux. On one hand, the warmer, shifted SST anomalies in the eastern tropical Pacific would increase the upward surface longwave radiation flux there, but on the other hand, the clouds induced by the warmer and shifted SST anomalies in the eastern tropical Pacific would trap the radiation and increase the downward surface longwave radiation flux. That is probably the reason why there is no

shift in the longwave radiation flux in the later regime relative to that in the earlier regime. The surface sensible heat flux is related to the temperature difference between surface ocean and lower atmosphere, and the surface wind. We do not have the data to analyze why the warmer and shifted SST anomalies and the eastward shift of westerly WS anomalies in the later regime failed to induce an eastward shift in the surface sensible heat flux field during El Niño in the tropical Pacific.

2.4.2 Model simulation results

The Zebiak-Cane coupled model, with the new subsurface temperature parameterization by neural networks, is used to study the influence of the climate shift in the mid 1970s on ENSO properties. In this model, the background seasonal climatology is prescribed, and can be changed for different climate regimes. Five sets of experiments were performed in this study.

The first set (set A) replaced the model oceanic monthly climatological fields (SST, oceanic surface layer currents and associated upwelling/downwelling) and the atmospheric climatologies (monthly surface WS fields and monthly surface wind divergence fields) with specified data for the 1961-1975 regime and the 1981-1995 regime in two separate model runs. Among these prescribed monthly climatological fields, the surface WS, surface wind divergence and SST were observed data, while the oceanic surface layer currents and associated upwelling/downwelling were computed for the two regimes from a run of the Zebiak-Cane ocean model forced by the observed WS during 1961-1995. Set B prescribed, in separate runs, the atmospheric monthly climatologies for the two regimes (but retained the original ocean climatologies), while set C prescribed the oceanic monthly climatologies for the two regimes (but retained the original atmospheric climatologies). Although the atmo-

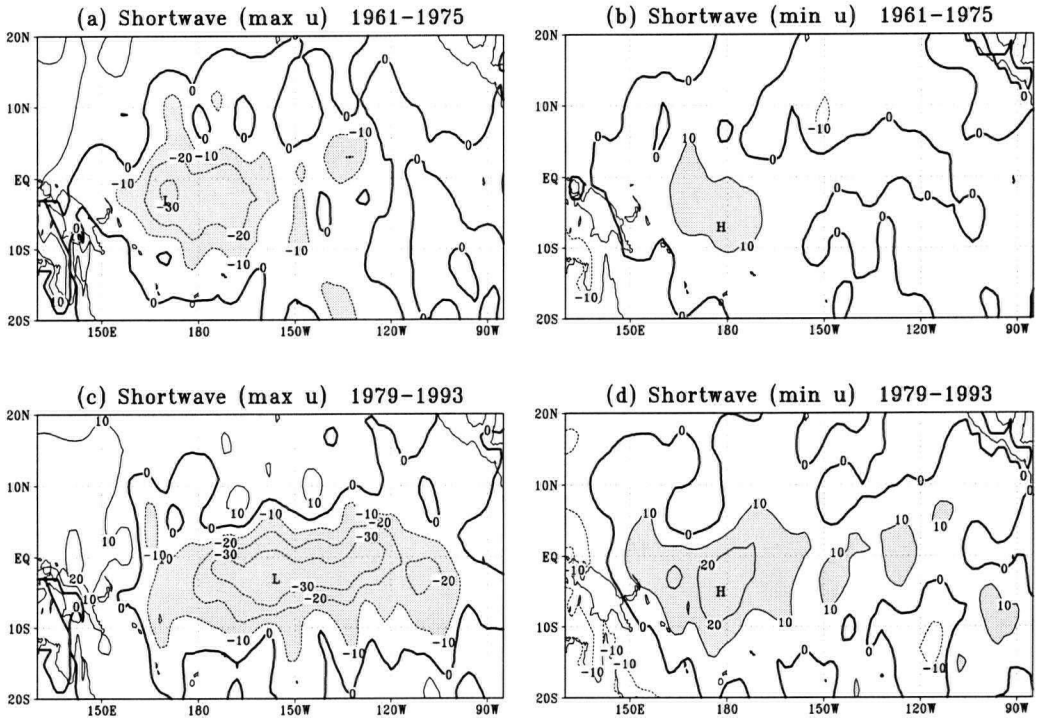

Figure 2.8: The net shortwave radiation flux (W m^{-2}) anomaly pattern ((a) - (d)) and latent heat flux (W m^{-2}) anomaly pattern ((e) - (h)) at the sea surface from the leading NLPCA mode in the 1961-1975 regime (top) and in the 1979-1993 regime (bottom) when the NLPC u assumes its maximum value (strong El Niño) and minimum value (strong La Niña). Regions with values greater than 10 W m^{-2} or less than -10 W m^{-2} are shaded. "L" and "H" mark the location of the lowest and highest values, respectively.

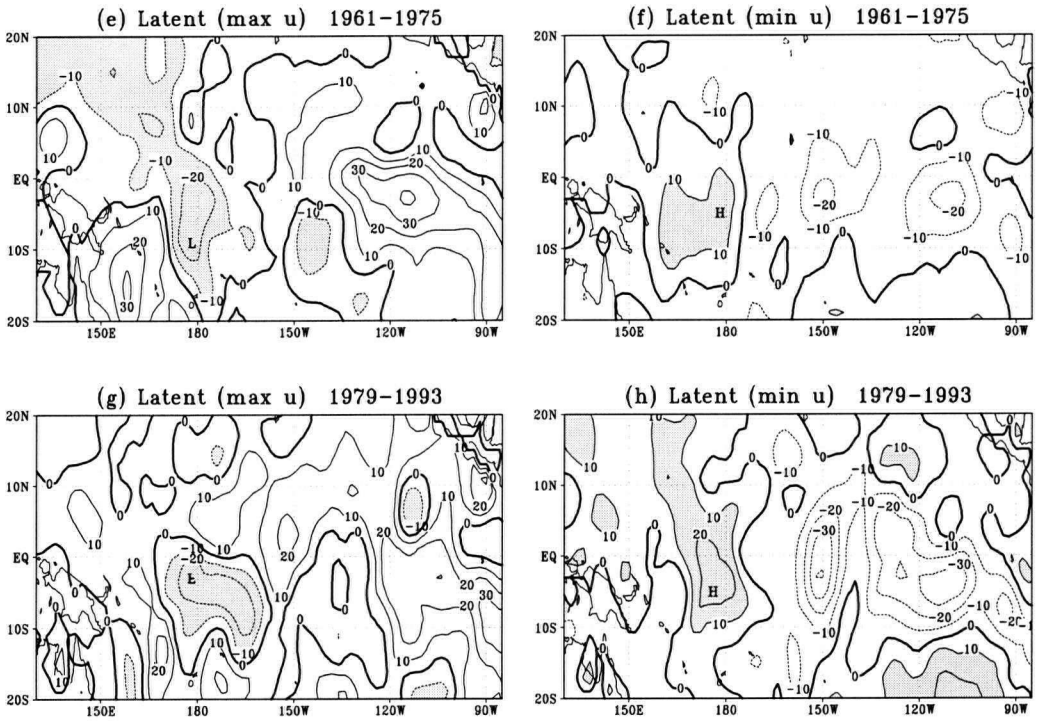

Figure 2.8 (Continued)

spheric and oceanic climatologies are in reality coupled, these additional sets try to identify the separate effects of changing the background state of the atmosphere and the ocean. Set D was similar to set A except that the oceanic monthly climatologies of the 1961-1975 regime were exchanged with those of the 1981-1995 regime, i.e., the model was prescribed with the atmospheric climatologies from the 1961-1975 regime and the oceanic climatologies from the 1981-1995 regime in D1, while in D2, the 1981-1995 atmospheric climatologies were paired with the 1961-1975 oceanic climatologies. Recent studies (McPhaden and Zhang, 2005) showed that Pacific Ocean circulation rebounded between July 1992 - June 1998 and July 1998 - June 2003, resulting in anomalously cool tropical Pacific SST during the period July 1998 - June 2003. This rebound can be viewed as an opposite shift relative to the shift in the mid 1970s. To study the effects of this opposite shift, set E used the atmospheric and oceanic monthly climatologies from the July 1992-June 1998 regime and the July 1998-June 2003 regime in two separate runs. For each experiment, the coupled model was run for 300 years and the statistical behavior of the model ENSO was examined using the model output from the last 200 years.

The NLPCA was applied to SST and WS anomalies from set A to study the combined effect of the atmospheric climatology and the oceanic climatology in the 1961-1975 regime and in the 1981-1995 regime. Fig. 2.9 shows that for strong El Niño the center of the SST anomalies (defined by the maximum value of the anomalies, as marked by the "H" in Fig. 2.9c) under the 1981-1995 regime climatology had an eastward displacement of about 11° relative to that under the 1961-1975 regime climatology (as marked by the "H" in Fig. 2.9a). In contrast, the center of the SST anomalies corresponding to strong La Niña did not show zonal displacement after the regime shift (as indicated by the location of the two "L" in Figs. 2.9b and d). There is evidence for a displacement in the zonal location of the

westerly WS anomaly centers as well. During strong El Niño, the westerly WS anomalies for the case using the 1981-1995 regime climatologies (Fig. 2.9e) were also enhanced in the eastern equatorial Pacific and the anomaly center shifted eastward by over 11° compared to that of the earlier regime (Fig. 2.9g). During strong La Niña, easterly anomaly WS centers were virtually at the same zonal locations for both cases (Figs. 2.9f and h). Though the extents of the eastward shifts in the SST and WS anomaly centers during strong El Niño were somewhat weaker in our experiments than in the observed data (Fig. 2.7), they indicated enhanced asymmetry between El Niño and La Niña after the regime shift.

Table 2.1 summarizes the amount of eastward shift in the SST and zonal WS anomaly centers in the post-shift regime (relative to those in the pre-shift regime) during strong El Niño and during strong La Niña, as determined from NLPCA.

In the B experiments (Table 2.1) where the atmospheric climatologies for the two regimes were prescribed, during strong El Niño, the westerly WS anomaly center shifted eastward by 11° in the later regime relative to the earlier regime (2.10 e and g), while the SST anomaly center was displaced by only 6° eastward (2.10 a and c). During strong La Niña, neither the easterly WS anomaly center nor the cool SST anomaly center was displaced after the regime shift (2.10b and d, f and h).

In the C experiments (Table 2.1) where the oceanic climatologies for the two regimes were prescribed, during strong El Niño, the zonal WS anomaly center showed weaker displacement compared to experiments A and B (2.11 e and g), while the SST anomaly center shifted eastward by 6° after the regime shift (2.11 a and c). Again, during strong La Niña no displacement in the zonal WS and SST anomaly centers can be found after the regime shift (2.11b and d, f and h). A caveat is that as the prescribed oceanic climatology was calculated from an ocean model driven by atmospheric forcing, it is not totally unaffected by

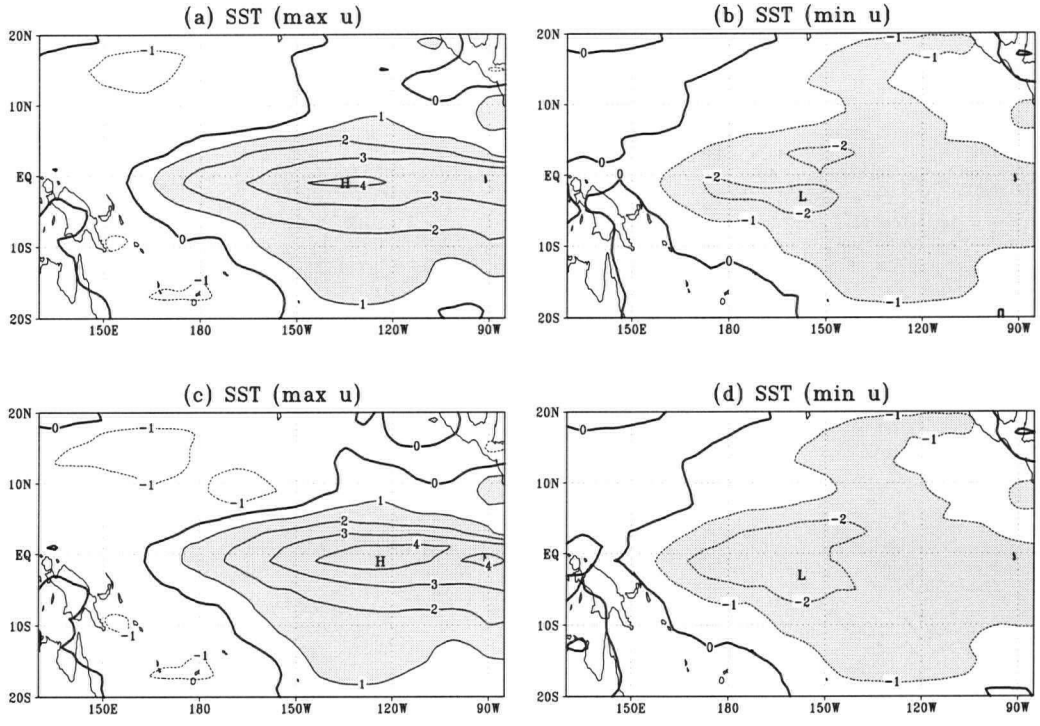

Figure 2.9: Set A experiments using the climatology of the oceanic and the atmospheric fields for the 1961-1975 regime (top panels (a), (b), (e) and (f)) and for the 1981-1995 regime (bottom panels ((c), (d), (g) and (h)): The SST anomaly pattern ((a)-(d)) and zonal WS anomaly pattern ((e)-(h)) from the leading NLPCA mode when the NLPC u takes its maximum value (strong El Niño) and minimum value (strong La Niña). Regions with anomaly magnitude exceeding 1.0 °C or 0.2 dyn cm^{-2} are shaded. "L" and "H" mark the location of the lowest and highest values, respectively.

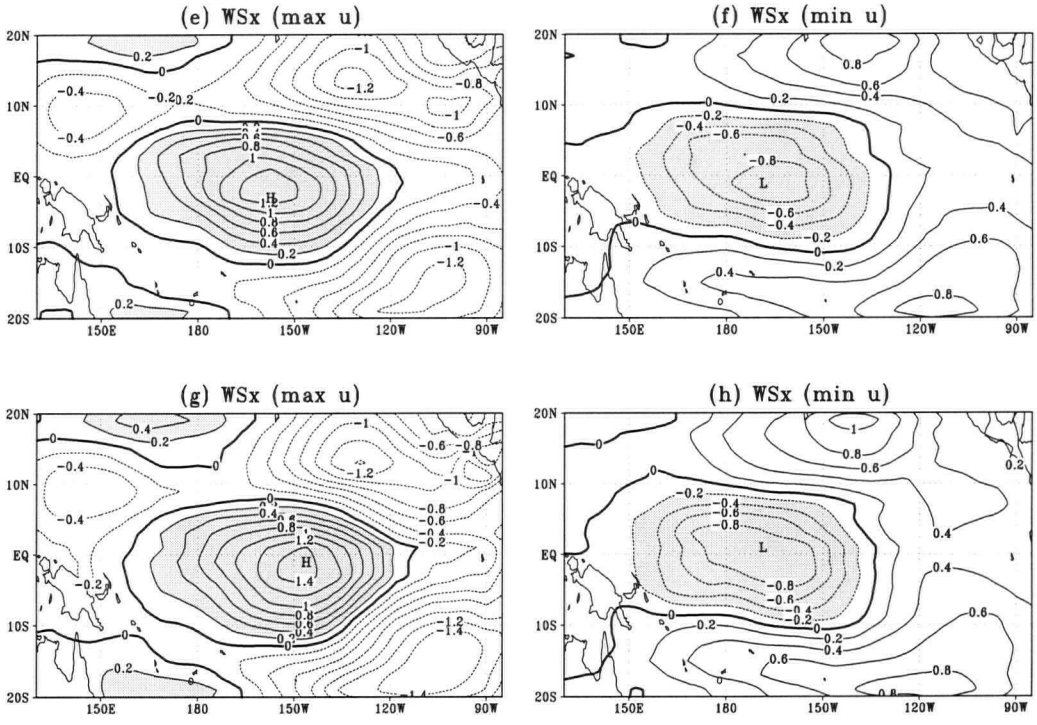

Figure 2.9 (Continued)

	El Niño		La Niña	
Exp.	SST	WSx	SST	WSx
A	11	11	0	0
B	6	11	0	0
C	6	6	0	0
D	0	11	0	0
E	-11	-11	0	0

Table 2.1: The eastward shift (in degrees longitude) of the SST and zonal WS anomaly centers in the post-shift regime (1981-1995 for A, B, C, D; 1998-2003 for E) relative to the pre-shift regime (1961-1975 for A, B, C, D; 1992-1998 for E) during strong El Niño and strong La Niña, as determined from NLPCA. In set A, atmospheric and oceanic monthly climatology were prescribed for both regimes, in B only the atmospheric, and in C only the oceanic. See text for set D and E. The quantized nature of the shift values arose from the model atmospheric zonal grid being 5.625°.

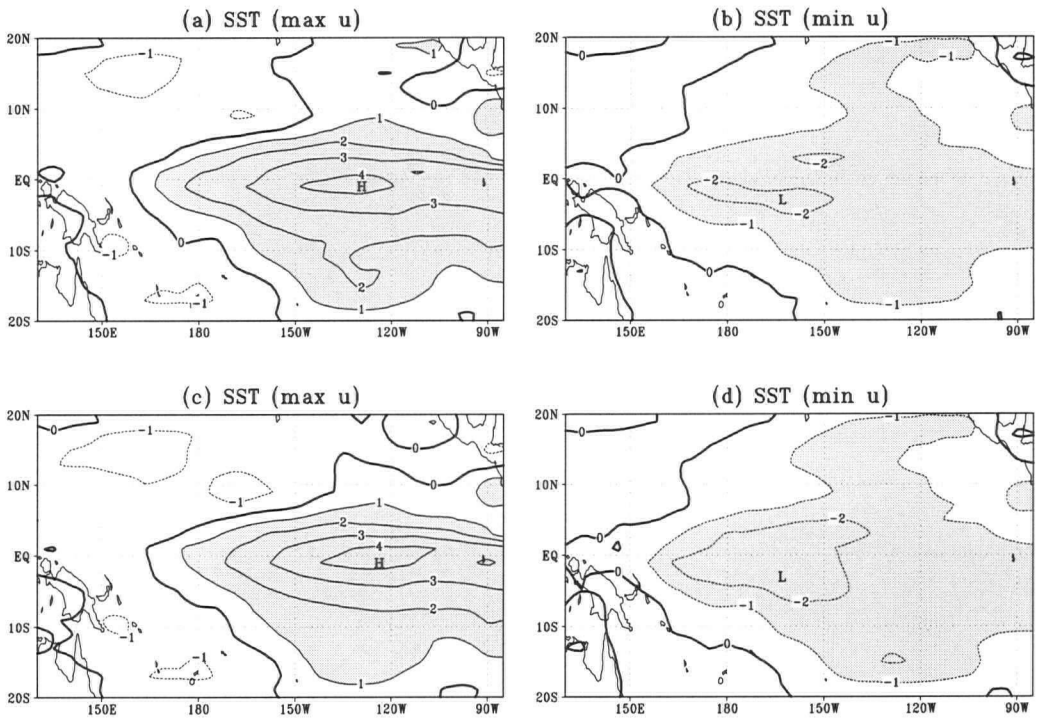

Figure 2.10: As in Fig. 2.9, but for set B experiment.

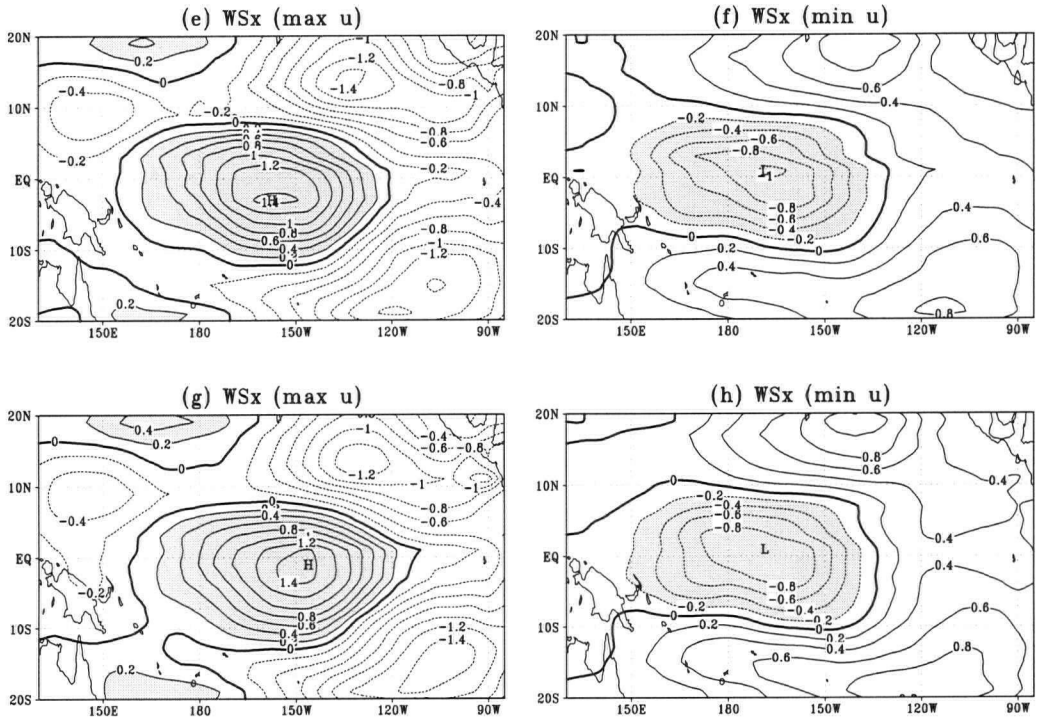

Figure 2.10 (Continued)

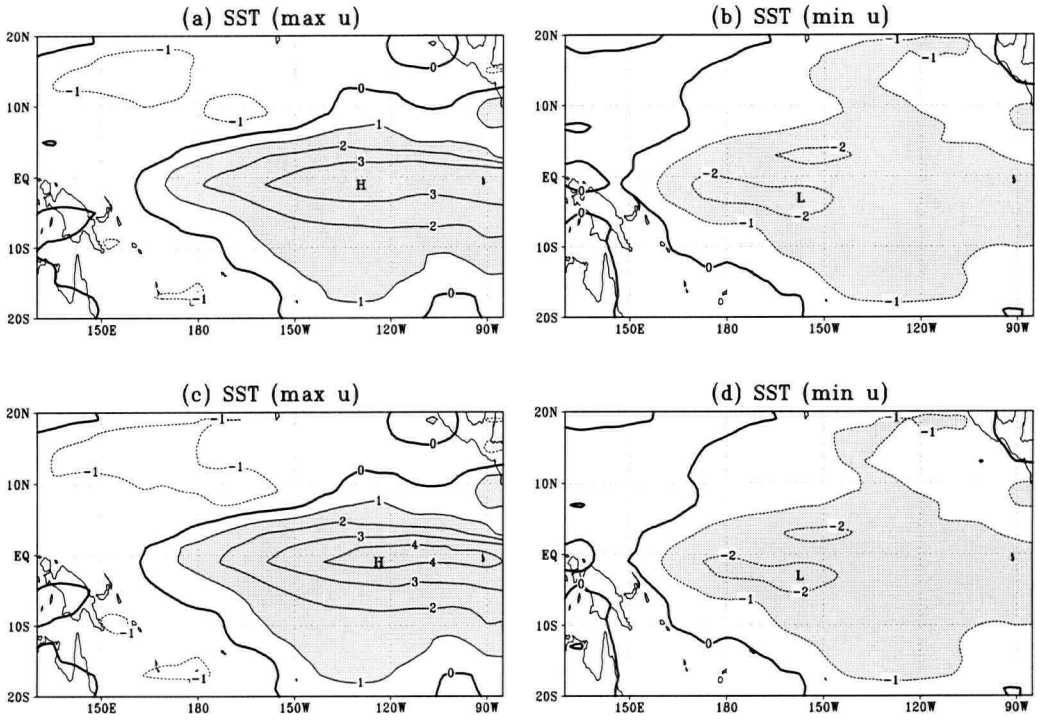

Figure 2.11: As in Fig. 2.9, but for set C experiment.

the atmospheric climatology. The D experiments will show that this "indirect atmospheric climatology effect" through the oceanic climatology is minor.

In the D experiments, where D1 has the 1961-1975 atmospheric climatology and the 1981-1995 oceanic climatology prescribed, and D2 the 1981-1995 atmospheric climatology paired with the 1961-1975 oceanic climatology, during strong El Niño the westerly center shifted eastward by 11° in D2 relative to D1 (Table 2.1), demonstrating that the atmospheric climatology was primarily responsible for the eastward shift of the westerly WS anomaly. Also these mixed climatology experiments showed that the "indirect atmospheric climatology effect" through the oceanic climatology is minor— if this indirect effect were as strong as the direct effect, then we would see no shift in the WS and SST anomaly centers between D2 and D1, as the the 1981-1995 atmospheric climatology would exert its direct

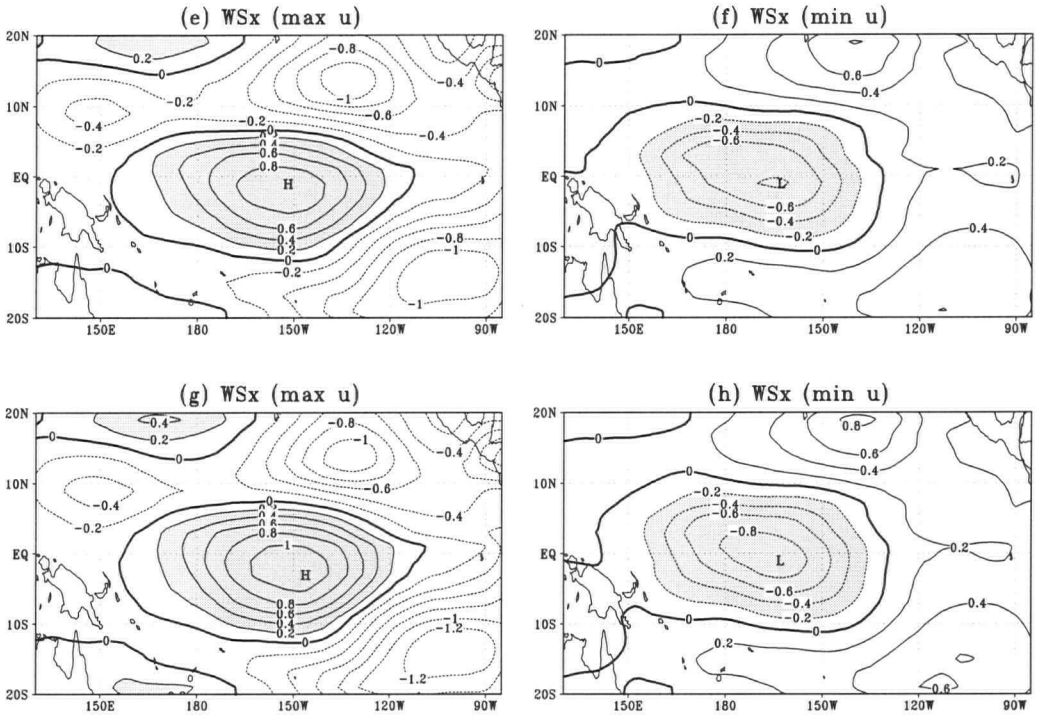

Figure 2.11 (Continued)

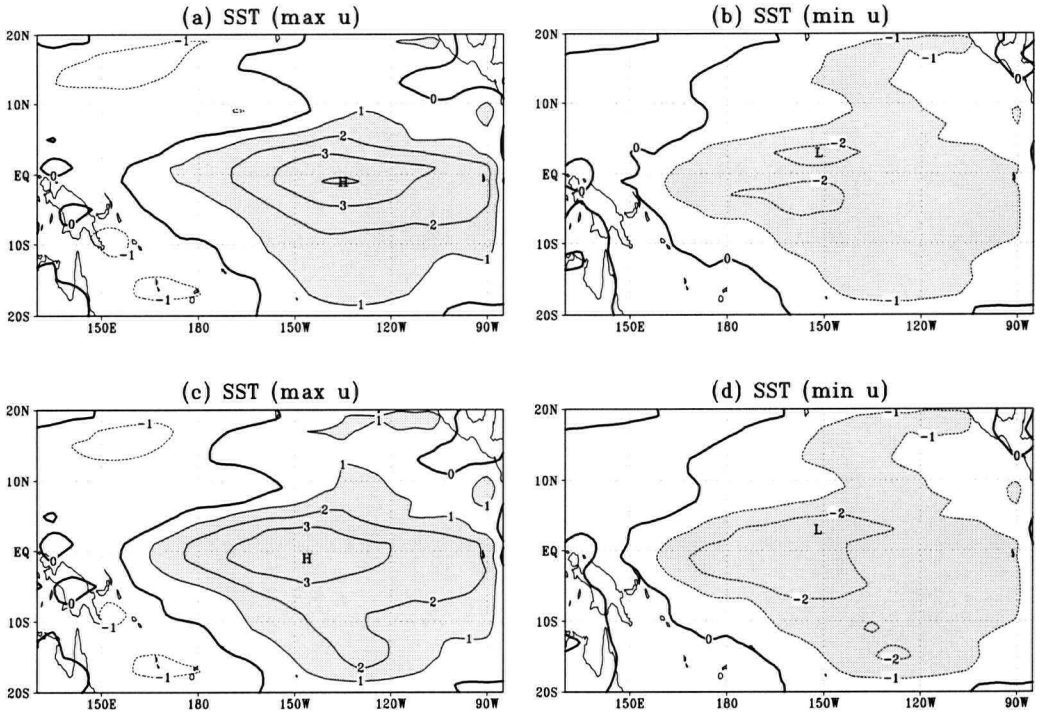

Figure 2.12: As in Fig. 2.9, but for set E experiment.

effect in D2 and its indirect effect (via the oceanic climatology) in D1.

The E experiments (Table 2.1) showed that opposite zonal shifts in the WS and SST anomaly centers can be produced by the rebound mean state (Fig. 2.12). Both SST and WS anomaly centers during strong El Niño shifted westward by 11 degrees (in longitude) in the regime July 1998 - June 2003 relative to the regime July 1992 - June 1998, whereas neither the SST anomaly center nor the WS anomaly center during strong La Niña was displaced between these 2 regimes. Hence the WS and SST anomaly shifts during strong El Niño induced by a change in the mean state are actually reversible, allowing both eastward and westward shifts to occur. However, throughout experiments A to E, the changes in the mean state did not induce shifts in the WS and SST anomaly centers during La Niña.

We also tested the sensitivity of the T_{sub} parameterization based on data from the ocean

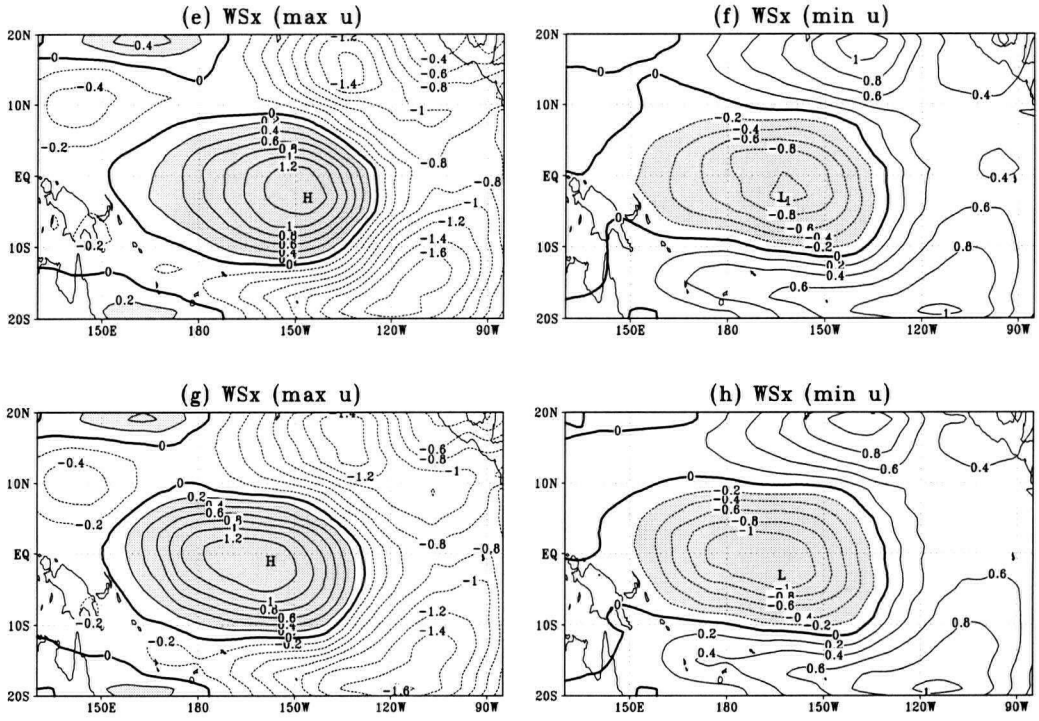

Figure 2.12 (Continued)

model forced by the observed wind stress before and after the mid 1970s. The nonlinear regression relationships were derived from the pre- and post-shift regimes separately. Westerly anomaly shifts similar to those seen in set A were found regardless whether the T_{sub} parameterization were derived from the periods 1964-75, 1981-95 or from the longer period of 1964-98. Thus the westerly anomaly shifts were caused by changes in the climatology rather than parameterization, thereby justifying our use of the single T_{sub} parameterization during the different regimes.

ENSO is an interactive thermodynamic system between the atmosphere and ocean, where the atmosphere dynamically forces the ocean by the surface WS, while the ocean thermally affects the atmosphere by heating/cooling. In the Zebiak-Cane coupled model, there are two heating anomaly terms in the atmospheric model (see Zebiak and Cane, 1987): the surface heating rate (Q_s) due to the SST and the convergence heating rate (Q_c) due to the moisture procedure. In our set A experiments, NLPCA revealed that during strong El Niño, the Q_c anomaly center intensified strongly and shifted eastward by about 28° in the later regime (Fig. 2.13c) relative to the earlier regime (Fig. 2.13a), while no significant eastward shift was found for the Q_s field (Fig. 2.14a and c). During strong La Niña, westward shift was found in the Q_c field (Fig. 2.13b and d). However, no shift was found in the Q_s field during strong La Niña. ((Fig. 2.14b and d). Hence it appears that Q_c played a role in altering the atmospheric circulation during El Niño in the later regime.

Sensitivity experiments were also used to identify the impact of the heating rate Q_c. When the Q_c term was deleted in the coupled model for the A experiments, there were no WS westerly anomaly shifts in the later regime relative to the pre-shift regime (Fig. 2.15). Thus the heating rate Q_c played a critical role in the WS westerly anomaly shift.

That ENSO predictability appeared to have changed following the mid 1970s regime shift

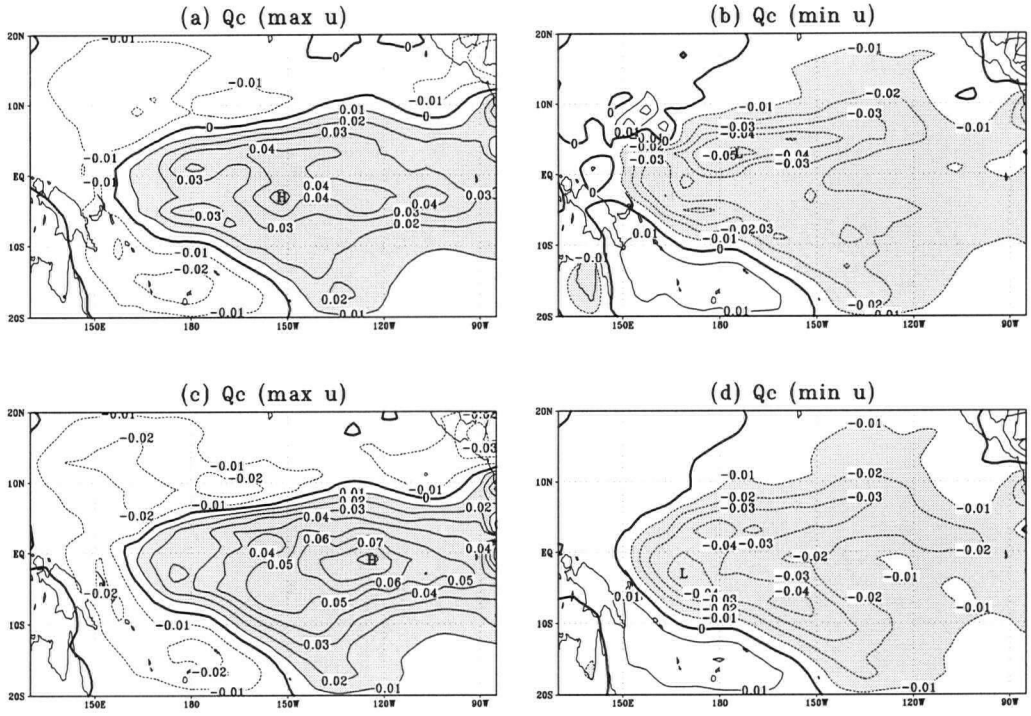

Figure 2.13: The model convergence heating rate field Q_c (m^2s^{-3}) from the leading NLPCA mode when the NLPC takes its maximum value (i.e. strong El Niño, left panels) and its minimum value (i.e. strong La Niña, right panels) when the 1961-1975 (top panels) and 1981-1995 (bottom panels) climatologies were used. Regions with anomaly magnitude exceeding 0.01 m^2s^{-3} are shaded.

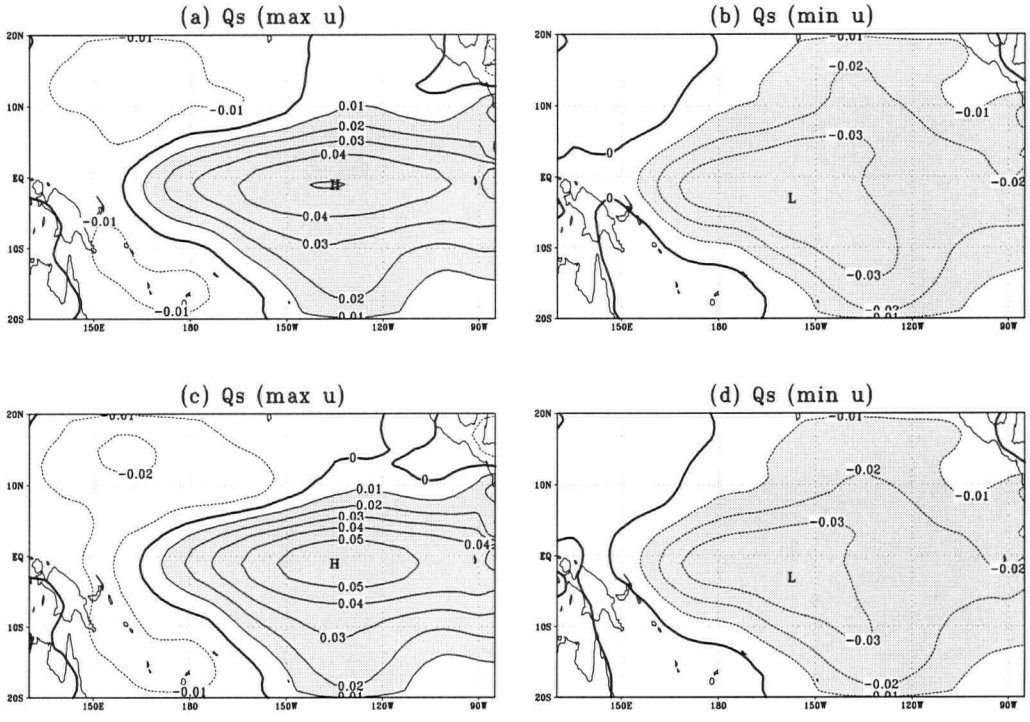

Figure 2.14: As in Fig. 2.13, but for Q_s.

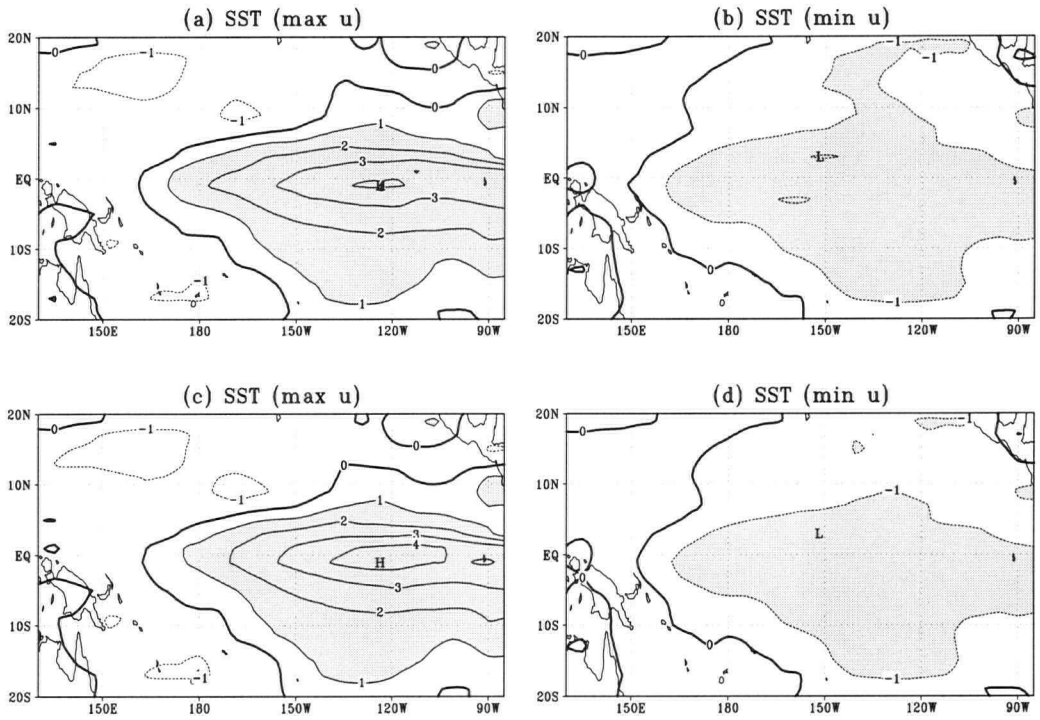

Figure 2.15: As in Fig. 2.9, but without Qc.

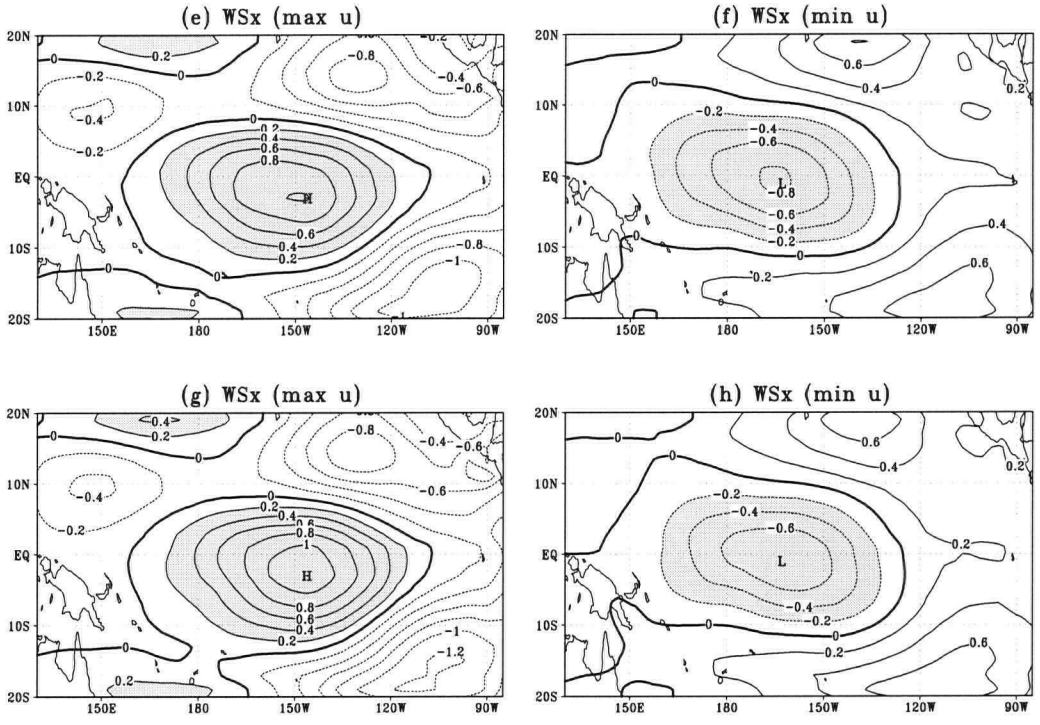

Figure 2.15 (Continued)

has been pointed out by Chen et al (2004) and An (2004). We next compute the change in the predictability in our set A coupled model experiments. The average SST anomaly in the Niño 3.4 region was predicted at lead times from 0 to 12 months by linear regression models using the 6 leading SST anomaly PCs and 6 leading WS anomaly PCs as predictors. The cross-validated correlation coefficients between the predicted and actual Niño 3.4 indices from our coupled model over 150 years can be used to represent predictability. Fig. 2.16 shows enhanced predictability in the post-shift climatology when the lead time is greater than 5 months. Fourier spectral analysis was also performed on the Niño 3.4 indices from the set A coupled model runs, where the spectral peak shifted from a period of 48 months under the pre-shift climatology to 52 months under the post-shift climatology (Fig. 2.17). Thus under the post-shift climatology, the ENSO mode has enhanced asymmetry between El Niño and La Niña (Fig. 2.9), increased ENSO period and enhanced predictability, relative to the earlier regime.

2.5 Discussion

Observations have revealed eastward shifts in the location of the zonal wind stress anomalies and the surface shortwave and latent heat flux during strong El Niño episodes after the mid 1970s climate regime shift. Using a modified Zebiak-Cane coupled model, we found that eastward shifts in the surface westerly anomalies and heating rate anomalies during the warm episodes were indeed found in the model when the 1981-1995 climatology was used instead of the 1961-1975 climatology. Our sensitivity studies indicated that it was mainly the change in the atmospheric climatology which caused the eastward shifts in the westerly anomalies and convergence heating rate anomalies, with the change in the upper ocean climatology being of minor importance. A caveat is that in the Zebiak-Cane model

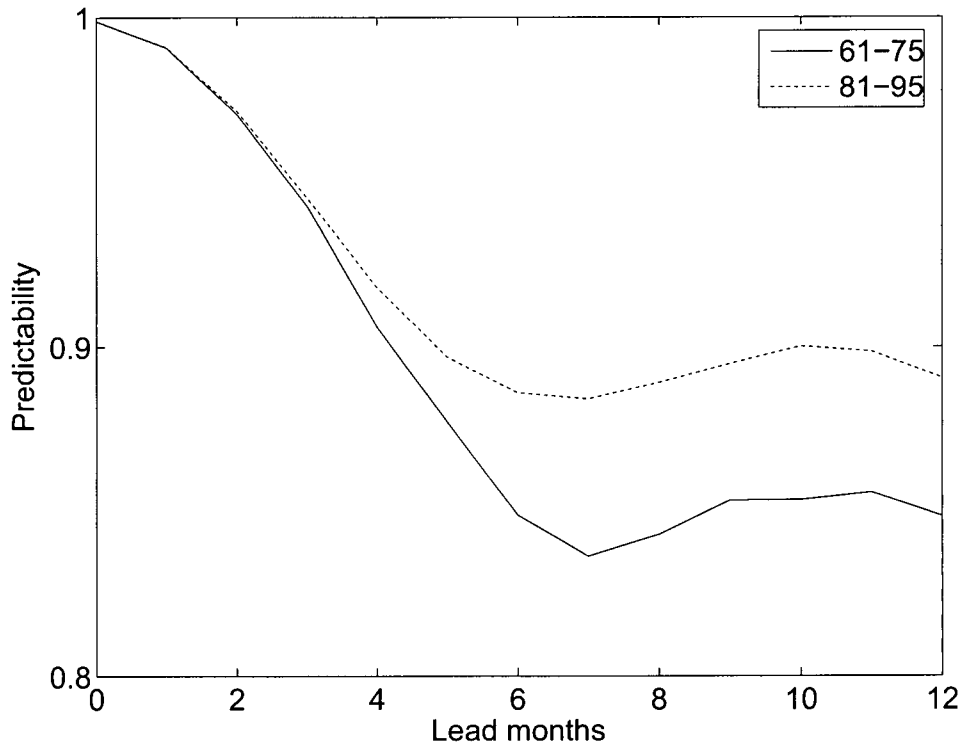

Figure 2.16: Predictability of the Niño 3.4 SST anomaly index, as given by the cross-validated correlation between the predicted and actual index in the coupled model using climatologies from the pre-shift and post-shift regimes. Cross-validation was performed by dividing the 150 years into five segments, where for each segment chosen to test the forecast correlation skills, the other four were used to build the forecast models.

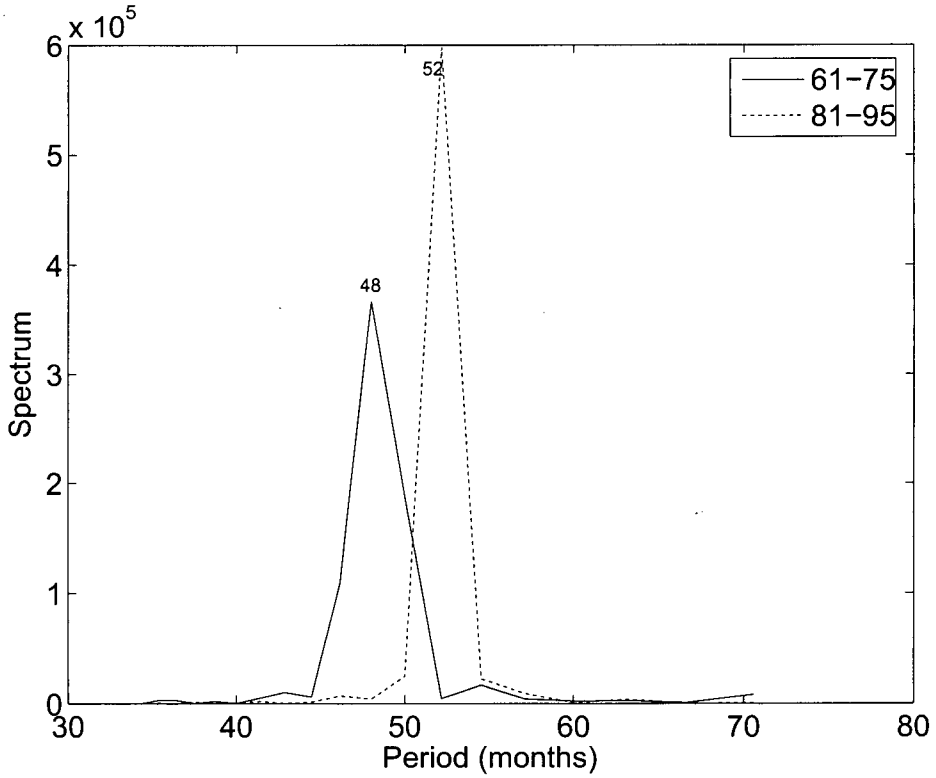

Figure 2.17: Spectrum of the Niño 3.4 SST anomaly index in the coupled model using climatologies from the pre-shift regime (solid curve) and post-shift regime (dashed curve).

the most important climatology field affecting ENSO property is known to be the surface wind divergence (Tziperman et al, 1997), so perhaps our findings are due to the particular formulation used in this model.

While the change in the surface background wind resulted in the eastward shifts in the surface wind anomalies and convergence heating rate anomalies during strong El Niño, during strong La Niña the eastward shifts were not evident in the 1981-1995 regime. Thus the asymmetry between the El Niño state and the La Niña state has been enhanced in the 1981-1995 regime, which also suggests enhanced nonlinearity in the ENSO system [An and Jin (2004) have found the asymmetry of ENSO was caused by the *nonlinear* dynamical heating terms]. Also consistent with observations are the enhanced predictability and lengthened ENSO period found when the model was run with the 1981-1995 climatology. All these agreements with observations suggest that despite the uncertainties in using climatologies calculated from relatively short records, using the 1981-1995 climatology in the coupled model did induce changes in ENSO properties consistent with observed changes.

The presence of stronger or more frequent El Niño episodes during the 1981-1995 regime could, through simple averaging, produce a change in the calculated SST mean state somewhat similar to that found (Fig. 2.6a). However, the change in the wind stress mean state (Fig. 2.6b) did not bear resemblance to the wind stress anomalies found during El Niño (Tang, 1995), so the change could not have been caused by the presence of stronger or more frequent El Niño episodes during the 1981-1995 regime. One possibility is that the change in the wind stress mean state was transmitted into the tropics by the atmospheric bridge from the extratropics (Barnett et al, 1999).

This chapter has advanced beyond An (2004) in at least three ways: (1) We examined the behaviour of additional variables (e.g. zonal shifts in the observed net shortwave radiation

flux and latent heat flux, shifts in the model convergent heating rate). (2) We corrected the bias in the original Zebiak-Cane model by using an inverse method to estimate the subsurface temperature, T_{sub}, and using neural networks to nonlinearly relate T_{sub} to the upper layer depth anomaly. Without these steps and the use of nonlinear PCA, we would not have been able to extract accurately the asymmetry between the El Niño and La Niña patterns. (3) While previous studies have noted the enhanced ENSO predictability after the mid 1970s, this result is not firm as the data record is short. Our use of 200 years of coupled model runs with the 1981-95 climatology has solidly confirmed this result.

2.6 References

An S.-I., 2004: Interdecadal changes in the El Niño La-Niña asymmetry. *Geophys. Res. Lett.*, 31, L23210. DOI:10.1029/2004GL021699.

An S.-I., and F.-F. Jin, 2004: Nonlinearity and asymmetry of ENSO. *J. Climate*, 17, 2399-2412.

An S.-I. and B. Wang, 2000: Interdecadal change of the structure of the ENSO mode and its impact on the ENSO frequency. *J. Climate* 13, 2044-2055.

Barnett T. P., D. W. Pierce, M. Latif, D. Dommenget and R. Saravanan, 1999: Interdecadal interactions between the tropics and midlatitudes in the Pacific basin. *Geophys. Res. Lett.*, 26, 615-618. DOI:10.1029/1999GL900042.

Bishop C. M., 1995: Neural Networks for Pattern Recognition, *Clarendon Press*, 482 pp.

Boulanger J.-P. and C. Menkes, 2001: The Trident Pacific model. Part 2: role of long equatorial wave reflection on sea surface temperature anomalies during the 1993-1998

TOPEX/POSEIDON period. *Climate Dyn.* 17, 175-186.

Bourassa M. A., S. R. Smith and J. J. O'Brien, 2001: A new FSU winds and flux climatology. 11th Conference on Interations of the Sea and Atmosphere. San Diego, CA, *Amer. Meteor. Soc.*, 912.

Chen D, M. A. Cane, A. Kaplan, S. E. Zebiak, and D. Huang, 2004: Predictability of El Niño in the past 148 years. *Nature* 428, 733-736.

daSilva A, A. C. Young and S. Levitus, 1994: Atlas of surface marine data 1994. Tech Rep 6, US Department of Commerce, NOAA, NESDIS.

Deser C and J. M. Wallace 1990: Large-Scale Atmospheric Circulation Features of Warm and Cold Episodes in the Tropical Pacific. *J. Climate*, 3, 1254-1281.

Fedorov A. V. and S. G. H. Philander, 2001: A stability analysis of tropical ocean-atmosphere interactions: Bridging measurements and theory for El Niño). *J. Climate*, 14, 3086-3101.

Flügel M., P. Chang and C. Penland, 2004: The role of stochastic forcing in modulating ENSO predictability. *J. Climate*, 17, 3125-3140.

Gu D. and S. G. H. Philander, 1997: Interdecadal climate fluctuations that depend on exchanges between the tropics and extratropics. *Science*, 275, 805-807.

Hsieh W. W., 2004: Nonlinear multivariate and time series analysis by neural network methods. *Rev. Geophys.*, 42, RG1003. DOI:10.1029/2002RG000112.

Jin F.-F., S.-I. An, A. Timmermann and J. Zhao, 2003: Strong El Niño vents and nonlinear dynamical heating. *Geophys. Res. Lett.* 30, 1120. OI:10.1029/2002GL016356.

Kleeman R., J. P. McCreary and B. A. Klinger, 1999: A mechanism for generating ENSO decadal variability. *Geophys. Res. Lett.*, 26, 1743-1746.

Knutson T. R. and S. Manabe, 1998: Model assessment of decadal variability and trends in the tropical Pacific Ocean. *J. Climate*, 11, 2273-2296.

Kramer M. A., 1991: Nonlinear principal component analysis using autoassociative neural networks. *AIChE. J.*, 37, 233-243.

Latif M., and T. P. Barnett, 1996: Decadal climate variability over the North Pacific and North America: Dynamics and predictability. *J. Climate*, 9, 2407-2423.

Li S, W. W. Hsieh and A. Wu, 2005: Hybrid coupled modeling of the tropical Pacific using neural networks. *J. Geophys. Res.*, 110, C09024, DOI:10.1029/2004JC002595.

McPhaden M. J. and D. Zhang, 2004: Pacific Ocean circulation rebounds, *Geophys. Res. Lett.*, 31, L18301. DOI:10.1029/2004GL020727.

Rodgers K. B., P. Friederichs and M. Latif, 2004: Tropical Pacific decadal variability and its relation to decadal modulations of ENSO. *J. Climate*, 17, 3761-3774.

Smith T. M. and R. W. Reynolds, 2004: Improved extended reconstruction of SST, 1854-1997). *J. Climate* 17, 2466-2477.

Tang B., 1995: Periods of linear development of the ENSO cycle and POP forecast experiments. *J. Climate*, 8, 682-691.

Tang Y. and Hsieh W. W., 2002: Hybrid coupled models of the tropical Pacific – ENSO prediction. *Climate Dyn.*, 19, 343-353.

Thompson C. J. and D. S. Battisti, 2001: A linear stochastic dynamical model of ENSO. Part II: Analysis. *J. Climate* 14, 445-466.

Tziperman E., S. E. Zebiak and M. A. Cane, 1997: Mechanisms of Seasonal - ENSO interaction. *J. Atmos. Sci.*, 54, 61-71.

Wang B. and S.-I. An, 2001: Why the properties of El Niño changed during the late 1970s. *Geophys. Res. Lett.*, 28, 3709-3712.

Wang B. and S.-I. An, 2002: A mechanism for decadal changes of ENSO behavior: Roles of background wind changes. *Climate Dyn.*, 18, 475-486. DOI:10.1007/s00382-001-0189-5.

Wu A. and W. W. Hsieh, 2003: Nonlinear interdecadal changes of the El Niño-Southern Oscillation. *Climate Dyn.*, 21, 719-730. DOI:10.1007/s00382-003-0361-1.

Zebiak S. E. and M. A. Cane, 1987: A model El Niño-Southern Oscillation. *Mon. Wea. Rev.*, 115, 2262-2278.

Zhang R.-H., R. Kleeman, S. E. Zebiak, N. Keenlyside and S. Raynaud, 2005: An empirical parameterization of subsurface entrainment temperature for improved SST anomaly simulations in an intermediate ocean model. *J. Climate*, 18, 350-371.

Zhang Y, J. M. Wallace and D. S. Battisti, 1997: ENSO-like interdecadal variability: 1900-93. *J. Climate*, 10, 1004-1020.

Zwiers F. W. and H. von Storch, 1995: Taking serial correlation into account in tests of the mean. *J. Climate* 8, 336-351.

Chapter 3

Changes in the Nonlinearity and Predictability [2]

3.1 Introduction

Predicting the future state of the El Niño-Southern Oscillation (ENSO), given its present state, is an important problem in climate research. Interdecadal changes in ENSO predictability are widely noted in different numerical models (Ji et al, 1996; Chen et al, 2004). An (2004) pointed out that the interdecadal change in predictability was related to the interdecadal change in ENSO asymmetry (between the warm El Niño states and the cool La Niña states) and nonlinearity. Changes in the mean climate state could produce changes in ENSO properties, including predictability (Kirtman and Schopf, 1998; An and Wang, 2000; Chapter 2).

There is evidence that nonlinear effects play an important role in ENSO properties. Münnich et al. (1991) suggested that nonlinear effects, more specifically a period-doubling bifurcation, led to the 4-yr ENSO period, based on their simple delayed-oscillator model. Nonlinear effects on the ENSO period were also discussed by Eccles and Tziperman (2004), while An and Jin (2004) showed that the nonlinear terms in the heat equation were respon-

[2] A version of this chapter will be submitted for publication. Ye, Z. and Hsieh, W. W. (2006) Can nonlinearity enhance predictability?.

sible for the remarkable asymmetry between the warm and cool ENSO states. However, there has been some debate on whether ENSO is primarily a self-sustained nonlinear system (Zebiak and Cane, 1987; Jin et al. 1994) or a damped linear system with stochastic atmospheric forcing (Penland and Sardeshmukh 1995), i.e. whether the role of nonlinearity in ENSO is primary or secondary. In this Chapter, we concentrate on the first possibility to explore the nonlinearity and ENSO interdecadal predictability. An intermediate coupled model data based on two different climatological mean states (corresponding to the 1961-75 and the 1981-1995 climate regimes) were used to analyze the nonlinearity, period and predictability. We also examined the well-known Lorenz nonlinear system (Lorenz, 1963) for comparison. Section 3.2 contains the results from the coupled model, where the nonlinearity, period and predictability of ENSO based on different climatological mean states are shown. Section 3.3 presents the results from the Lorenz system.

3.2 Intermediate coupled results

The modified Zebiak and Cane (1987) coupled model (see Chapter 2) was used to simulate ENSO for 2300 years, with the last 2100 years of data analyzed. In this model, the background seasonal climatologies (sea surface temperature (SST), oceanic surface layer currents and associated upwelling/downwelling, surface wind stress (WS) and surface wind divergence) were prescribed with the data from the 1961-1975 regime and the 1981-1995 regime in two separate model runs. A 13-month running mean was applied to the coupled model data. The 2100-year data record was divided into 21 equal segments, allowing us to compute ensemble means over 21 members, instead of the single runs reported in Chapter 2.

For an example of an individual ensemble member, the spatial patterns from the first

NLPCA mode in the last 100-year data for strong El Niño and La Niña are shown in Fig. 3.1. For strong El Niño the center of the SST anomalies (defined by the maximum value of the anomalies, as marked by the "H" in Fig. 3.1c) under the 1981-1995 climatology had an eastward displacement of about 23° relative to that under the 1961-1975 climatology (as marked by the "H" in Fig. 3.1a). As there was no displacement in the La Niña case (Fig. 3.1b and d), the asymmetry between El Niño and La Niña , hence the nonlinearity increased under the 1981-1995 climatology.

The histogram of the first PC (time series) for all ensemble members are shown in Fig. 3.2. The frequency of occurrence for the strong El Niño (corresponding to the large positive PC1) is higher under the 1985-1995 climatology. A similar conclusion can be obtained from the Niño3 index results (averaged SST anomalies in 90°-150°W, 5°S-5°N). The number of times when the Niño3 indices are greater than 3°C are 163 and 238 months for the pre-shift and post-shift regimes, respectively. The ensemble mean of the 21 members' spatial pattern also shows a eastward displacement in the "H" during strong El Niño and no shift in the "L" during strong La Niña under the post-shift climatology (Fig. 3.3), although the displacement in "H" here is less than in Fig. 3.1.

One way to characterize the nonlinearity in the data is to compare the percentage variance explained by the first mode from PCA with that from NLPCA (which fits a curve instead of a straight line to account for the maximum variance in the dataset) (Hsieh, 2004). Let

$$\delta = (P_{NL} - P_L)/P_L, \tag{3.1}$$

where P_{NL} is the percentage variance explained by the NLPCA mode 1, and P_L, by the (linear) PCA mode 1 (see Chapter 2).

The ensemble mean ± 1 standard error for δ is 8.1%±0.1% for the simulation under the

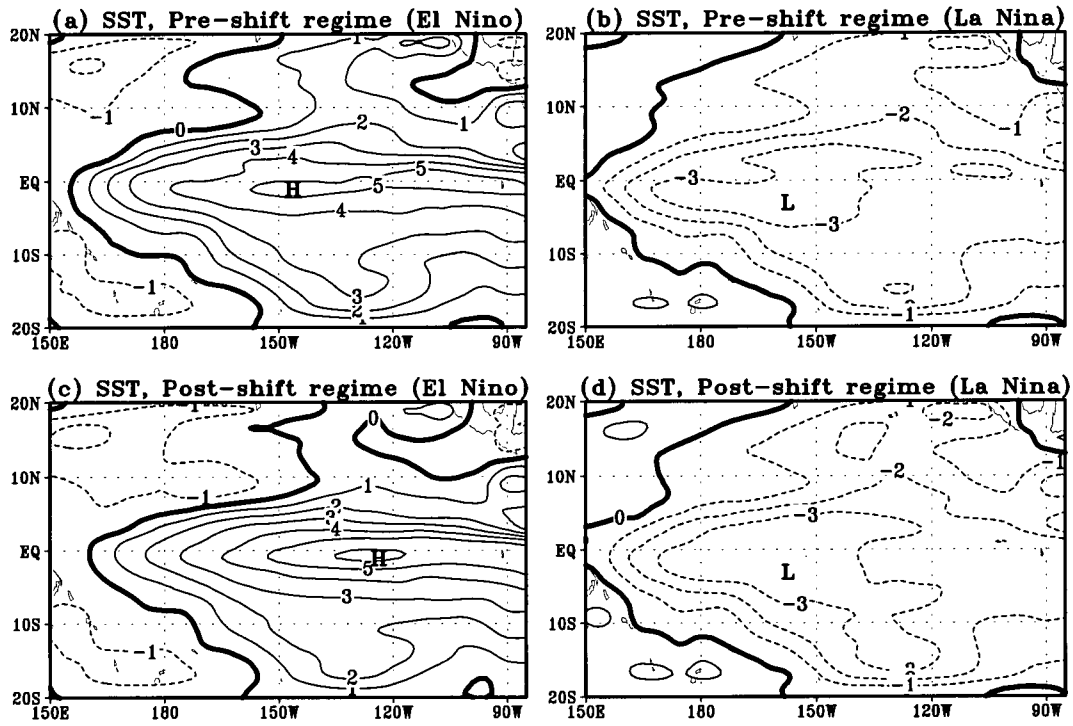

Figure 3.1: The SST anomaly (°C) pattern from the leading NLPCA mode when the NLPC takes its maximum value (strong El Niño) and minimum value (strong La Niña) for the last 100-year model output in the experiments using the climatology of the oceanic and the atmospheric fields for the 1961-1975 regime ((a)-(b)) and for the 1981-1995 regime ((c)-(d)). "L" and "H" mark the location of the lowest and highest values, respectively.

1961-75 climatology and 8.8%±0.1% under the 1981-95 climatology, indicating enhanced nonlinearity under the latter climatology. This enhanced nonlinearity arose from the greater asymmetry found in the SST anomaly patterns between El Niño and La Niña under the 1981-95 climatology (see Chapter 2). The asymmetry in turn is produced by the nonlinear terms in the heat budget of the upper ocean (An and Jin, 2004).

The average SST anomaly in the Niño 3.4 region (120°W-170°W, 5°S-5°N) was predicted at lead times from 0 to 15 months by nonlinear regression using Bayesian regularization neural network (NN) models (Bishop, 1995) provided by the MATLAB neural network toolbox. At time t, the 2 leading principal components from a combined PCA of the normalized SST, zonal and meridional WS anomalies were used as predictors to forecast the Niño 3.4 SST anomaly at t + lead time. The ensemble-averaged cross-validated correlation coefficients and mean squared error (MSE) between the predicted and actual Niño 3.4 indices from our coupled model can be used to characterize ENSO predictability (Fig. 3.4), where enhanced predictability under the 1981-95 climatology can be seen when the lead time exceeds 5 months. For comparison, the predictability based on linear regression (as used in Chapter 2) is lower than that based on nonlinear regression (Fig. 3.4), but gives the same conclusion, i.e. using the 1981-95 climatology in the coupled model enhanced the ENSO predictability.

Fourier spectral analysis performed on the Niño 3.4 indices from the 2 coupled model runs revealed that the main spectral peak shifted from a period of 49 months under the 1961-75 regime climatology to 52 months under the 1981-95 regime climatology (Fig. 3.5). The lead times for attaining a correlation skill of 0.95 by nonlinear regression (Fig. 3.4a) are 7.9 and 8.3 months for the pre- and post-1980 climatologies, respectively. Dividing these predictability lead times by the respective spectral periods of 49 and 52 months for the

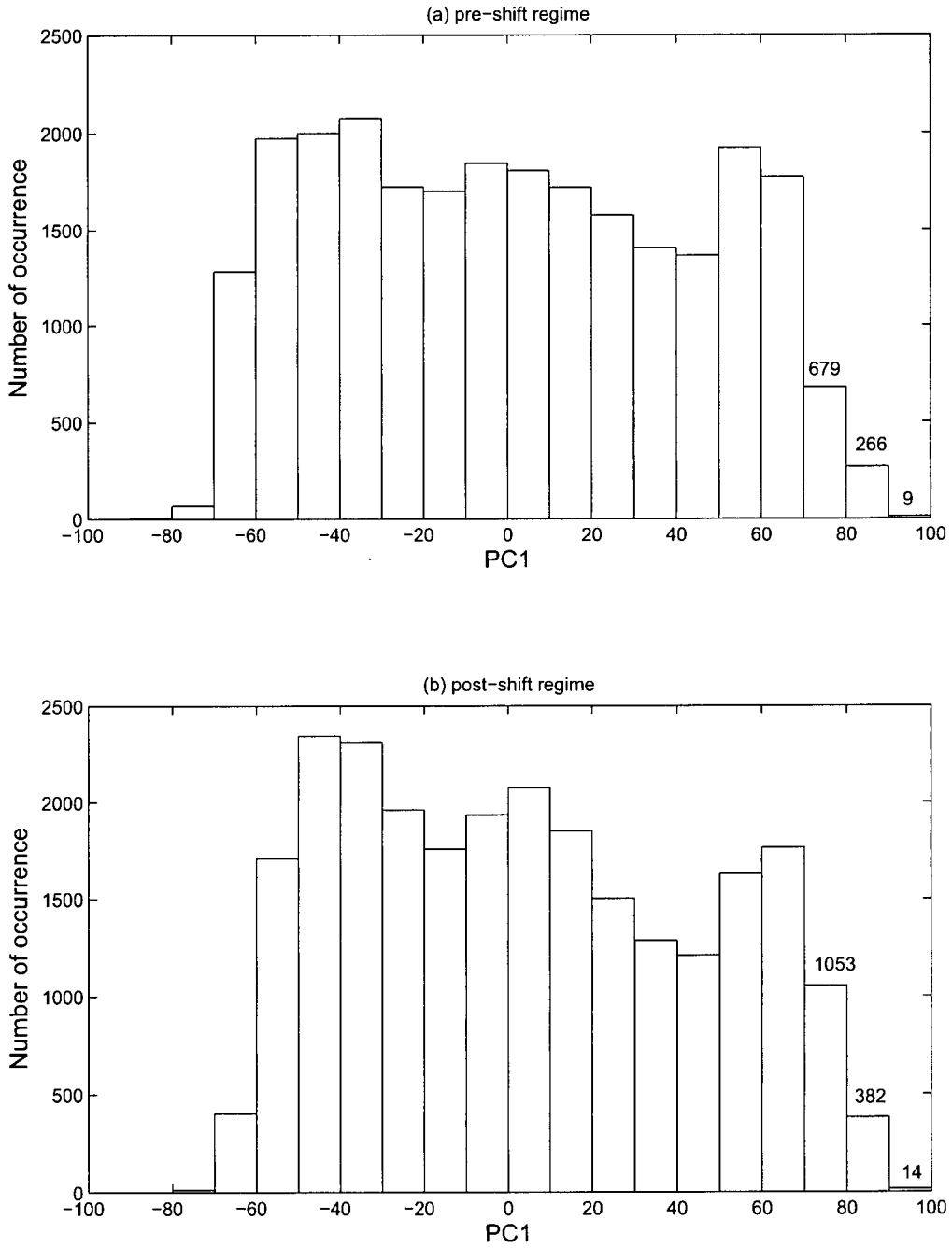

Figure 3.2: Histogram of the first PCs for all 21 members (a) for pre-shift climate state run and (b) for post-shift climate state run.

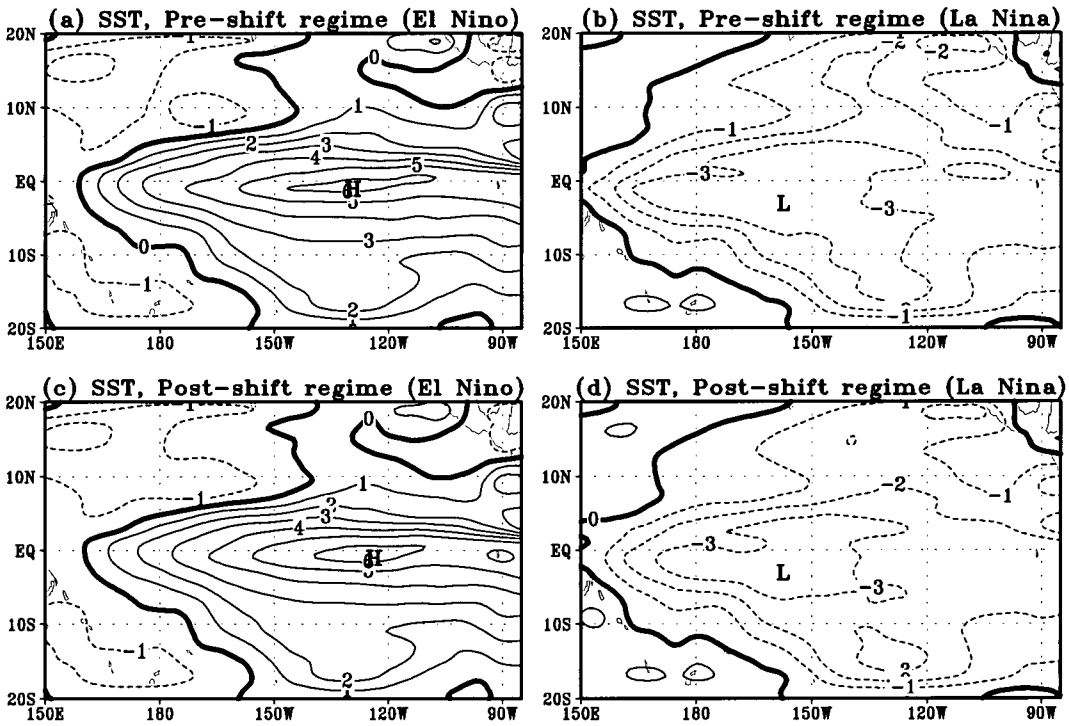

Figure 3.3: As in Fig. 3.1, but for the ensemble mean.

two regimes yielded a lead time equal to 0.16 periods for both regimes. In other words, when predicting 0.16 cycles ahead, the nonlinear regression method can attain a correlation skill of 0.95 in this noiseless coupled model of ENSO under both the pre- and post-1980 climatologies.

3.3 Lorenz attractor data

We next turn to a very different nonlinear system to see if the same behavior can be found. The Lorenz (1963) nonlinear system is given by

$$dx/dt = -ax + ay\,, \tag{3.2}$$

$$dy/dt = -xz + bx - y\,, \tag{3.3}$$

$$dz/dt = xy - cz\,, \tag{3.4}$$

where x, y, z are proportional to the intensity of convective motion, the temperature gradient in the horizontal and vertical directions, respectively. A fourth-order Runge-Kutta method was used to integrate the equations (from $t = -15$ to 60 at time steps of 0.05) from initial conditions $(x, y, z) = (-9.42, -9.43, 28.3)$, with parameters $a = 10$, $b = 28$, and $c = 8/3$. Data from $t = 0$ to 60 were analyzed.

The degree of nonlinearity of the system can be characterized by 2 parameters:

$$\beta_y = \frac{\langle |xz| \rangle}{\langle |bx| \rangle + \langle |y| \rangle}\,, \quad \beta_z = \frac{\langle |xy| \rangle}{\langle |cz| \rangle}\,, \tag{3.5}$$

where $\langle ... \rangle$ denotes the temporal mean, β_y measures the size of the nonlinear term relative to the size of the linear terms in (3.3), and similarly, β_z for (3.4).

We next perform four numerical experiments by varying the parameters (a, b, c): Case 1 uses the same parameters as in Lorenz (1963) (Table 3.1); Case 2 multiplies the parameters

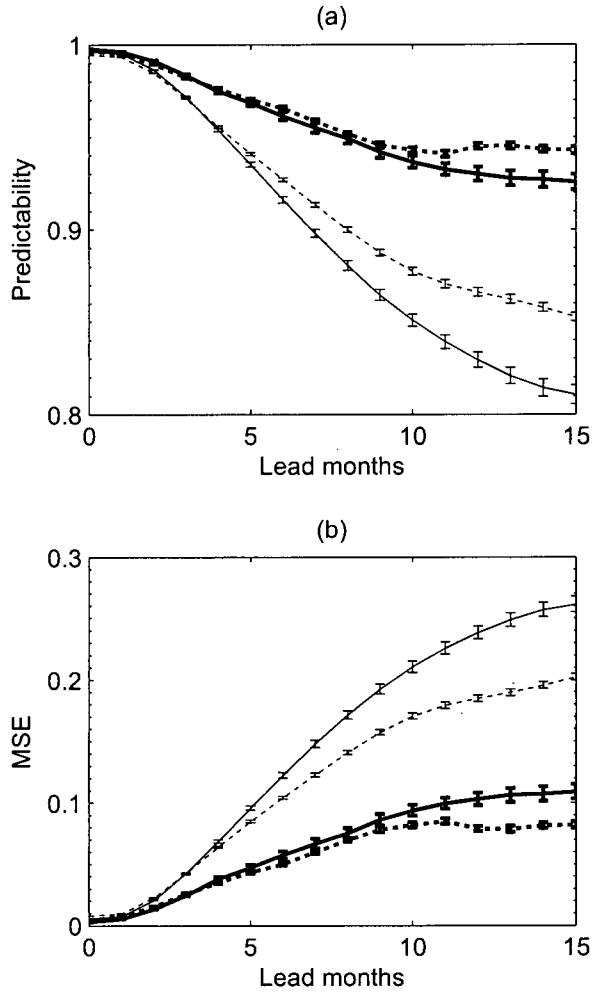

Figure 3.4: Ensemble mean predictability (top) and MSE (bottom) of the Niño 3.4 SST anomaly index, as given by the cross-validated correlation between the predicted and actual index in the coupled model using climatologies from the 1961-75 regime (solid lines) and the 1981-95 regime (dashed lines). The thick lines are from nonlinear regression, the thin lines, linear regression. Cross-validation was performed by dividing each 100-year data record into five segments, where for each segment chosen to test the forecast correlation skills, the other four were used to build the forecast model. Error bars indicate ± 1 standard error of the ensemble mean.

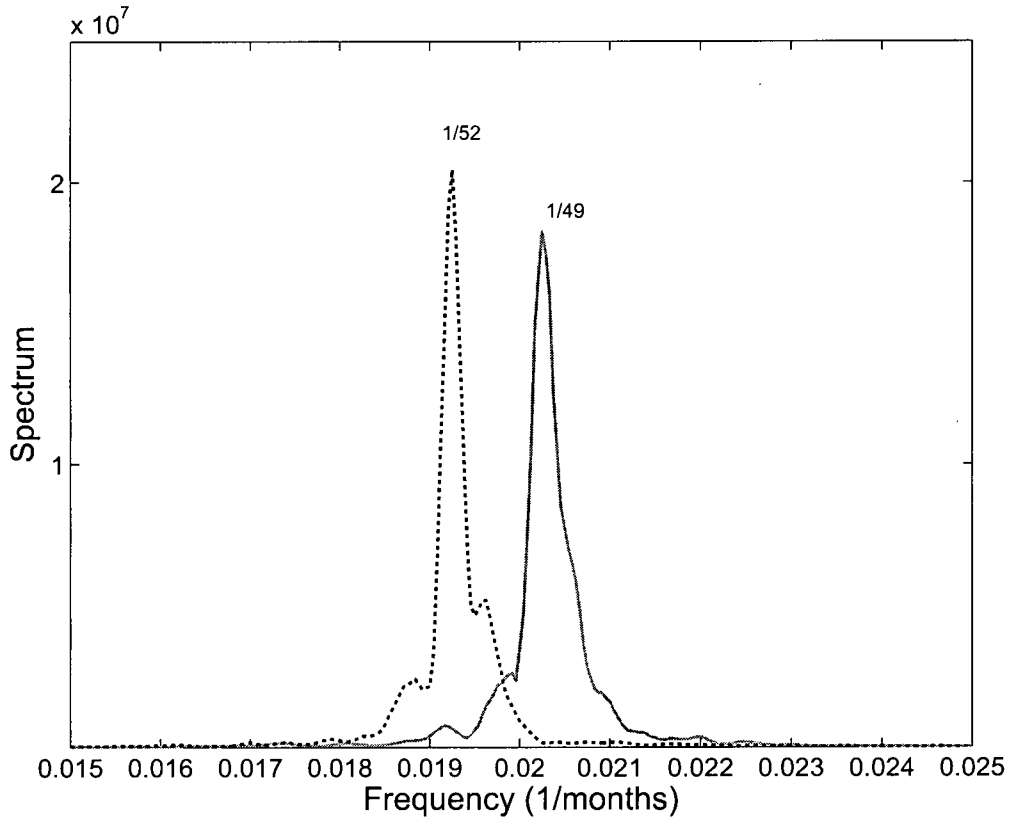

Figure 3.5: Spectrum of the Niño 3.4 SST anomaly index in the coupled model using climatologies from the pre-shift regime (solid curve) and post-shift regime (dashed curve).

of Case 1 by the uniform factor of 1.3; Case 3 uses the parameters from Basu and Foufoula-Georgiou (2002); and Case 4, from Elsner and Tsonis (1992). The nature of the oscillations varies among the four cases (Fig. 3.6). For each case, 21 ensemble runs were made by adding one percent stochastic noise onto the initial data (i.e., the initial data x_o, y_o, z_o were changed to $(1+0.01\alpha_1)x_o$, $(1+0.01\alpha_2)y_o$, $(1+0.01\alpha_3)z_o$, where α_1, α_2 and α_3 were Gaussian random numbers with zero mean and unit standard deviation).

Table 3.1 lists β_y and β_z calculated from (3.5) for the four cases. The main spectral periods T_x and T_z determined from the power spectra of x and z, respectively (Fig. 3.7) are also listed in Table 3.1. The spectral behavior of y (not shown) is basically the same as as that for x, but z shows sharper spectral peaks than x (Fig. 3.7). Proceeding inversely from Case 4 to Case 1, one finds a progressive increase in β_y and β_z, and in T_x and T_z, indicating that an increase in the nonlinearity of the system coincides with an increase in the spectral period of the oscillations.

Case	1 (Lorenz, 1963)	2	3 (Basu, 2002)	4 (Elsner & Tsonis, 1992)
param(a, b, c)	(10, 28, 8/3)	(13, 36.4, 3.47)	(16, 45.92, 4.0)	(16, 120.1, 4.0)
nonlinearity β_y	0.033	0.026	0.020	0.008
nonlinearity β_z	0.400	0.307	0.271	0.260
x period (step)	15.2	12.4	11.2	10.4
z period (step)	15.2	11.3	9.2	5.4

Table 3.1: Ensemble mean results for Lorenz systems with different parameter pairs.

Again (x, y, z) at time t were used as predictors in nonlinear regression models to separately predict these three variables at time t+lead time (where the lead time ranged from 0 to 20 time steps). Fig. 3.8 shows enhanced predictability (with higher correlation coefficient and lower MSE) for z as one proceeds inversely from Case 4 to Case 1, where the nonlinearity of the system increased. This behavior in predictability was also found for x (not shown), though for a given level of correlation skill, x tends to have longer lead times than z.

Since relative to x, the predictability lead time for z tends to be shorter, and its main spectral period T_z is also $\leq T_x$ and more sensitive to changes in the Lorenz system parameters (Table 3.1), we now focus on z. Its predictability lead time (for 0.80 correlation skill) divided by the main spectral period T_z is 0.69, 0.69, 0.70 and 0.65 for Cases 1 to 4, respectively, i.e. in all 4 cases, the nonlinear regression model when predicting ahead by 0.7 times the period in z can attain a correlation skill of 0.8 for all four cases, thereby demonstrating that the enhanced predictability was basically due to the lengthened period of the oscillations when the nonlinearity of the Lorenz system was enhanced from Case 4 to Case 1. For the correlation skill of 0.95, its predictability lead time divided by the main spectral period T_z is 0.51, 0.50, 0.50 and 0.46 for Cases 1 to 4, respectively. So a similar conclusion can be drawn regardless of the correlation skill level chosen.

A caveat on the Lorenz system: The system is chaotic only over a range of parameter values. Our numerical runs were done over a range where the Lorenz system was chaotic. If the parameters were increased or decreased by the right amount, the Lorenz system could simply converge from the initial state to a single point in the (x, y, z) space.

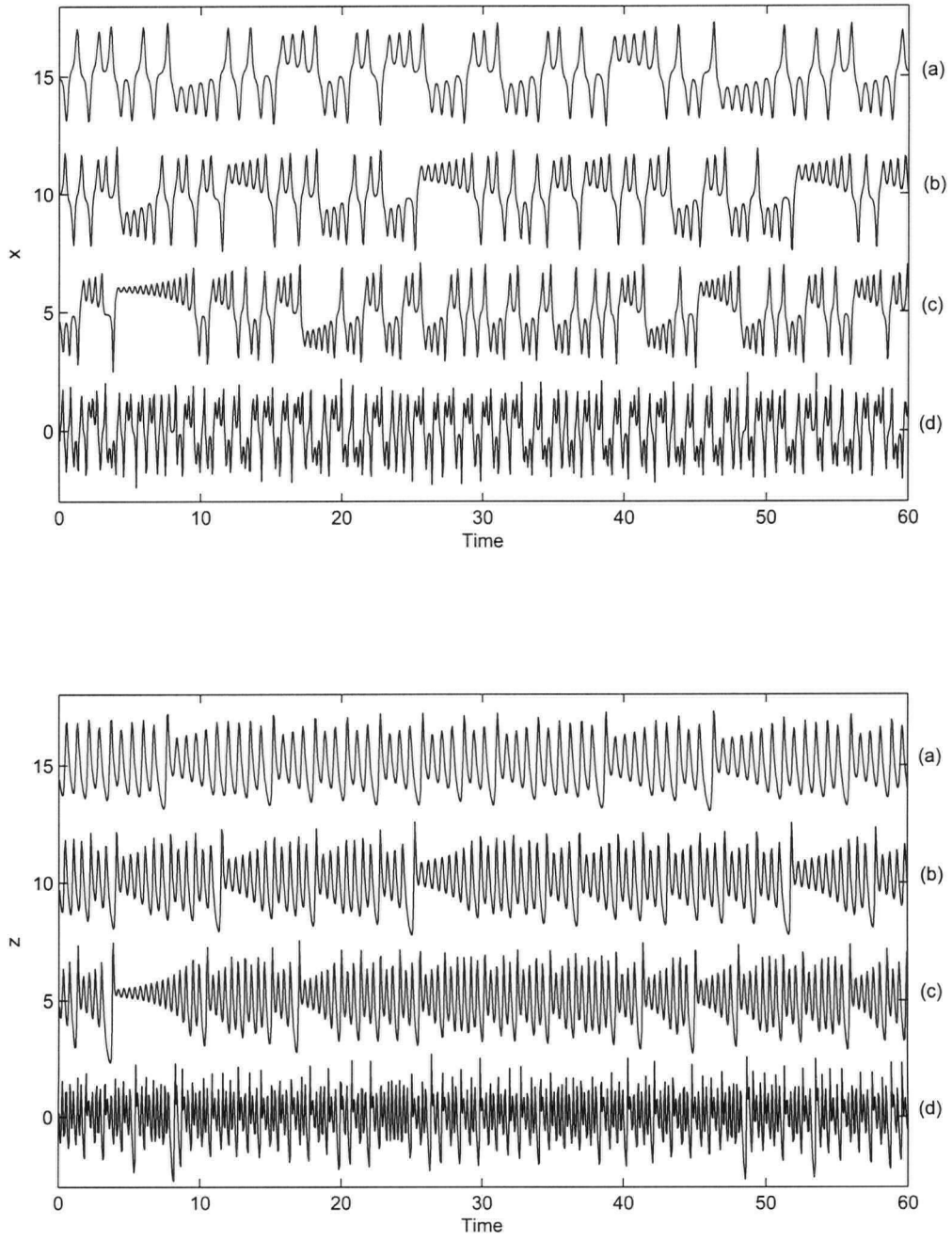

Figure 3.6: Normalized time series of x (top panel) and z (bottom panel) in the Lorenz model for (a) Case 1, (b) Case 2, (c) Case 3 and (d) Case 4, where the time series for different cases are vertically shifted by multiples of 5 for legibility.

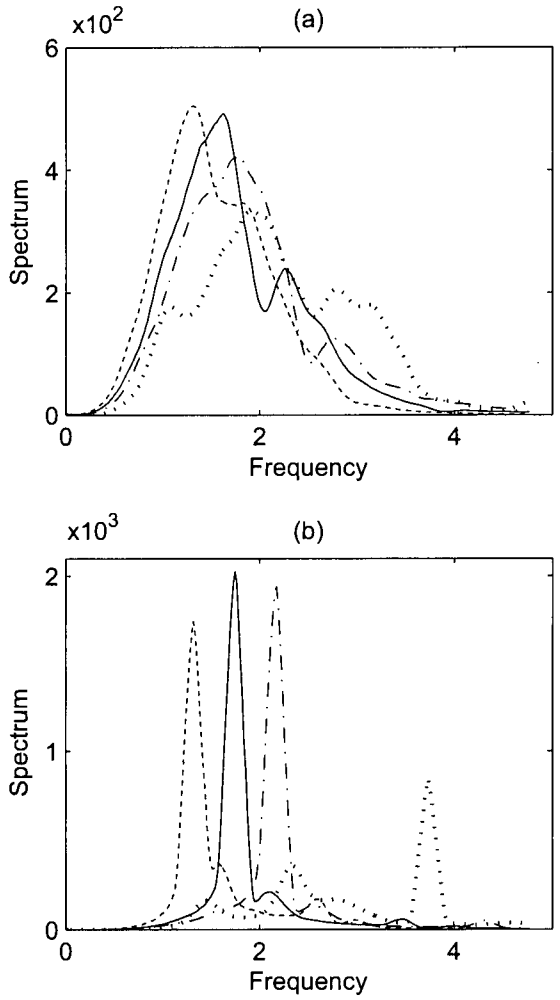

Figure 3.7: Ensemble mean power spectrum of the normalized (a) x and (b) z components. Dash, solid, dash-dot and dotted lines represent Case 1, 2, 3 and 4, respectively.

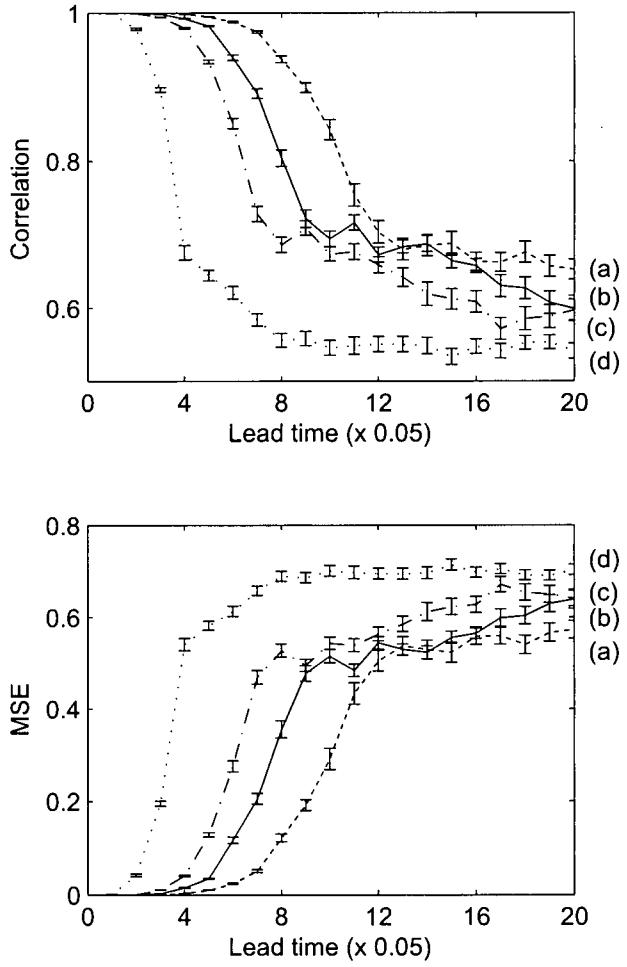

Figure 3.8: Ensemble mean predictability in terms of correlation skill (top) and MSE (bottom) of z in the Lorenz system, as given by the cross-validated correlation and MSE between the predicted and actual time series. Dash, solid, dash-dot and dotted lines represent Case 1 (a), 2 (b), 3 (c) and 4 (d), respectively, with error bars showing ± 1 standard error.

3.4 Summary and conclusion

Numerical coupled model results show that the predictability of ENSO is closely related to its nonlinearity and period. Under the post-1980s climatology, ENSOs have stronger nonlinearity and longer period. The longer period enhance the system persistence, leading to better predictability. This behavior was also found in the Lorenz chaotic system.

It is important to emphasize that it is not the stronger nonlinearity that causes the better predictability, nor vice versa. The dynamics have to adjust both the nonlinearity and the predictability to be consistent with each other according to the nonlinearity-predictability relation found here.

The ENSO system under different climate states and the Lorenz system with different parameters studied here were all in the chaotic domain. We did not discuss the 'extreme' nonlinear state like the limit cycle, where, the system becomes periodic.

3.5 References

An S.-I., 2004: Interdecadal changes in the El Niño La-Niña asymmetry. *Geophys. Res. Lett.*, 31, L23210. DOI:10.1029/2004GL021699.

An S.-I., and F.-F. Jin, 2004: Nonlinearity and asymmetry of ENSO. *J. Climate*, 17, 2399-2412.

An S.-I. and B. Wang, 2000: Interdecadal change of the structure of the ENSO mode and its impact on the ENSO frequency. *J. Climate* 13, 2044-2055.

Basu S. and E. Foufoula-Georgiou, 2002: Detection of nonlinearity and chaoticity in time series using the transportation distance function, *Phys. Lett. A*, *301*, 413-423.

Bishop C. M., 1995: Neural Networks for Pattern Recognition, *Clarendon Press*, 482 pp.

Chen D, M. A. Cane, A. Kaplan, S. E. Zebiak, and D. Huang, 2004: Predictability of El Niño in the past 148 years. *Nature* 428, 733-736.

Eccles F. and E. Tziperman, 2004: Nonlinear effects on ENSO's period. *J. Atmos. Sci.*, 61, 474-482.

Elsner J. B. and A. A. Tsonis, 1992: Nonlinear prediction, chaos and noise. *Bull Amer Meteor Soc*, 73, 49-60.

Hsieh W. W., 2004: Nonlinear multivariate and time series analysis by neural network methods. *Rev. Geophys.*, 42, RG1003. DOI:10.1029/2002RG000112.

Ji M., A. Leetmaa and V. E. Kousky, 1996: Coupled model predictions of ENSO during the 1980s and the 1990s at the National Centers for Environmental Prediction, *J. Climate*, 9, 3105-3120.

Jin F.-F., D. Neelin and M. Ghil, 1994: ENSO on the devil's staircase, *Science*, 264, 70-72.

Kirtman B. P. and P. S. Schopf, 1998: Decadal variability in ENSO predictability and prediction, *J. Climate*, 11, 2804-2822.

Lorenz E. N., 1963: Deterministic non-periodic flow. *J. Atmos. Sci.*, 20, 130-141.

Münnich M., M. A. Cane and S. E. Zebiak, 1991: A study of self-excited oscillations of the tropical ocean-atmosphere system. Part II: Nonlinear cases, *J. Atmos. Sci.*, 48, 1238-1248.

Penland C. and P. D. Sardeshmukh, 1995: The optimal-growth of tropical sea-surface temperature anomalies, *J. Climate*, 8, 1999-2024.

Ye Z. and W. W. Hsieh, 2006: The influence of climate regime shift on ENSO. *Climate Dyn.*, 26, 823-833. DOI:10.1007/s00382-005-0105-5.

Zebiak S. E. and M. A. Cane, 1987: A model El Niño-Southern Oscillation. *Mon. Wea. Rev.*, 115, 2262-2278.

Chapter 4

Changes in the leading ENSO modes: Role of surface zonal current [3]

4.1 Introduction

In the late 1970s, an abrupt change of the climate state in the midlatitude as well as in the tropical Pacific was observed (Nitta and Yamada, 1989; Trenberth and Hurrell, 1994). Together with this climate shift, the main characteristics of the interannual variability over the tropical Pacific have changed (Wang, 1995; An and Wang, 2000; An et al., 2005). On one hand, the multi-decadal variation in the climate state causes non-stationary characteristics of the El Niño-Southern Oscillation (ENSO) (e.g., Fedorov and Philander, 2000; An and Jin, 2000). On the other hand, the multi-decadal variation can also be attributed to the internal nonlinear process of ENSO in a certain parameter regime (Timmermann et al., 2003; An and Jin, 2004). Although it is still uncertain whether the ENSO system is linear or nonlinear (e.g., Philander and Fedorov, 2003; Eisenman et al., 2005), the late 1970s

[3] A version of this chapter has been published. An, S.-I., Ye, Z. and Hsieh, W. W. (2006) Changes in the leading ENSO modes associated with the late 1970s climate shift: Role of surface zonal current. Geophys. Res. Lett. 33, L14609, doi:10.1029/2006GL026604.

climate shift appears strong enough to change the leading ENSO mode.

An et al. (2005) obtained the nonlinear ENSO cycle in the evolution of tropical Pacific thermocline anomalies using a variant of the nonlinear principal component analysis (NLPCA) method, which performs a closed curve fit (see Appendix B.2) of the data in the multi-dimensional PC (principal component) space. Interestingly, the shape of the closed curve, especially its asymmetry, significantly changed since the late 1970s, from which we infer a change of the leading ENSO mode. An and Jin (2000) showed that the interdecadal change could lead to a quantitative change in the leading eigenmode of a stripped-down version of the intermediate ENSO model. In this chapter, observational evidence of the interdecadal change in the leading ENSO mode, especially in the role of the surface zonal currents, is revealed by NLPCA, while An et al (2006) also performed the eigenanalysis of the intermediate ENSO model linearized with respect to the two climatological mean background states.

4.2 Combined NLPCA of the sea level and current anomalies

The data used are the University of Maryland Simple Ocean Data Assimilation (SODA) monthly mean sea level height, SST and upper-50m surface zonal current for January 1958-December 2001 (Carton et al., 2000). The anomalies were obtained by removing the climatological monthly mean, and then a 7-month running mean was applied. A combined principal component analysis (CPCA) on the monthly mean sea level height, sea surface temperature (SST) and upper-50m surface zonal current anomalies was then performed. In Fig. 4.1, the main features of sea level height, SST and surface zonal current variability are

summarized by the two leading modes: the first and second modes of sea level height are respectively a zonal contrast mode (Fig. 4.1c) and an approximate zonal-symmetric mode (Fig. 4.1d) with respect to the equator; those of SST are a horseshoe pattern like the mature phase of ENSO (Fig. 4.1a) and an equatorially-confined pattern like an initial phase of ENSO (Fig. 4.1b), respectively; those of the surface current are a localized zonal/meridional contrast mode (Fig. 4.1e) and an equatorial basin-wide mode (Fig. 4.1f), respectively. Obviously, the first (leading) mode is highly correlated with the ENSO index, and the second mode shows a lead/lag relationship with the ENSO index.

The trajectory plot of the two leading PCs associated with CPCA is shown in Fig. 4.2. The mean location of the tracks for the pre-1980s (1958-1979) is located at the first quadrant in the PC1-PC2 plane, while that for the post-1980s (1980-2001) is located at the third quadrant, suggesting a possible regime shift.

From the first six PCs of the CPCA modes, we extracted the first combined NLPCA mode, giving a closed curve in the 6-dimensioned PC space. In Fig. 4.3, the time evolution of SST, sea level height and surface zonal current associated with the first NLPCA mode along the equatorial band over one cycle are shown. These modes explain 67.5% and 73.3% of total variance during the pre- and post-1980s, respectively, which are greater than those of the leading CPCA mode (36%). For the pre-shift regime, the standing-type oscillation in the sea level height with its node around the dateline and its center at 120°W is observed (Fig. 4.3b); the surface zonal current also shows a standing-type oscillation with a basin-wide pattern with its minimum at the boundaries; and SST anomalies (Fig. 4.3a) show a westward propagating tendency. The surface zonal current pattern is very similar to the so-called 'ocean basin mode' (Neelin and Jin, 1993). The ocean basin mode is a natural mode produced by the equatorial trapped waves and their reflection at boundaries: the equatorial

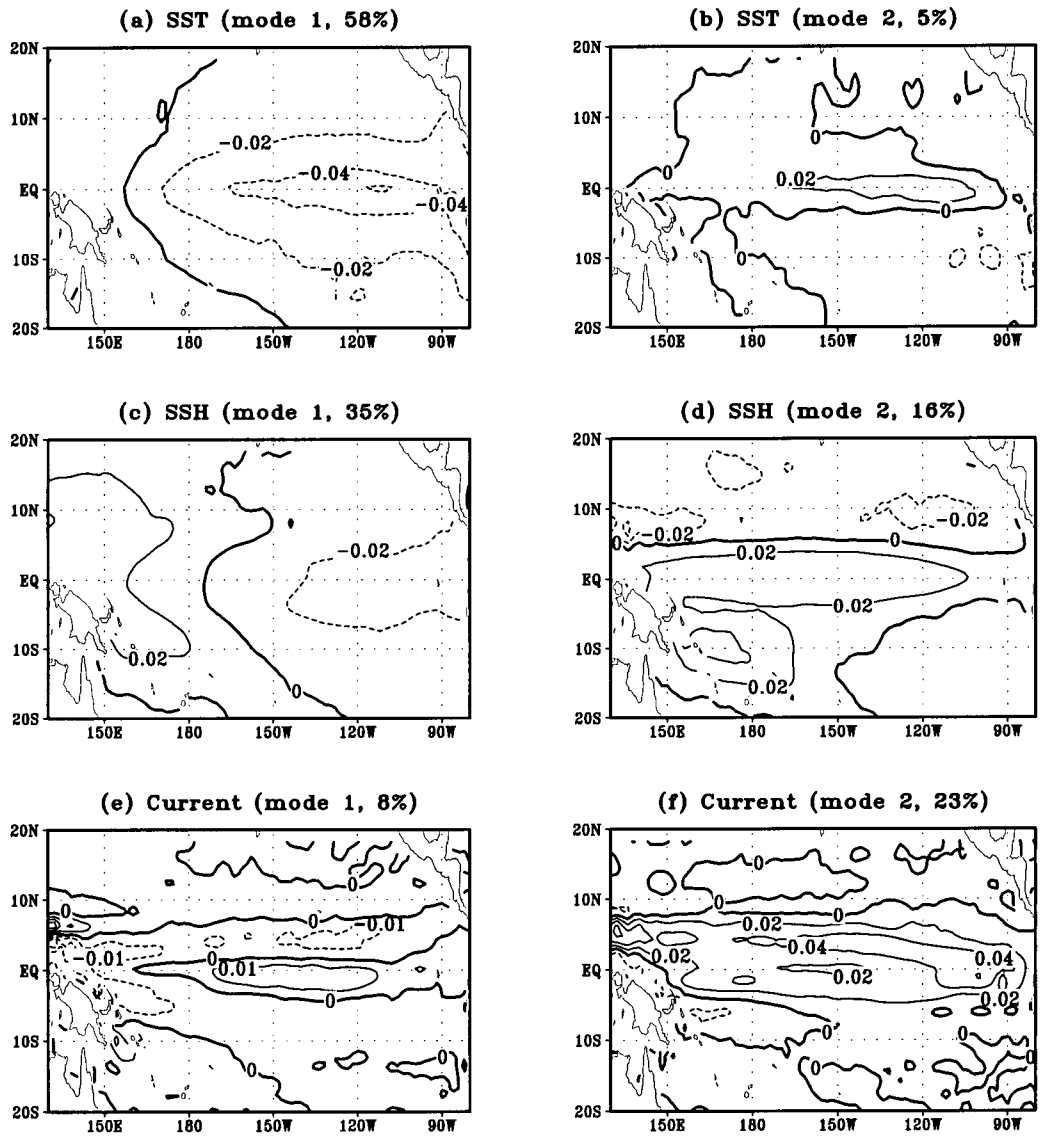

Figure 4.1: The first and second modes of the SST (top), sea level height (middle) and surface zonal current (bottom) anomalies obtained from a Combined Principal Component Analysis (CPCA). The percentage of overall variance explained is 36% by the first CPCA mode and 14% by the second mode. The percentage of variance explained for each variable is given in the title of each panel.

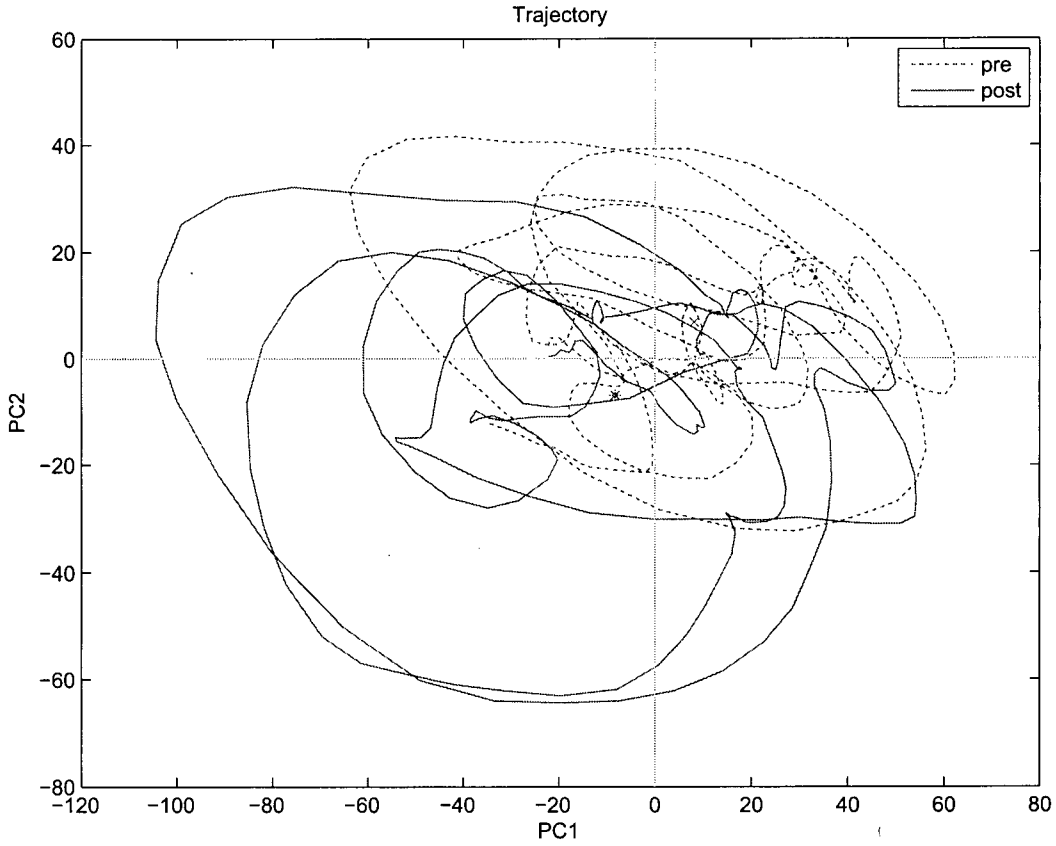

Figure 4.2: Trajectory plot of the principal components of the first and second PCs for the pre-1980s and the post-1980s. "x" and "*" mark the mean location in the PC space of the pre-1980s and the post-1980s data, respectively.

Kelvin wave travels eastward until it hits the eastern boundary where it is mainly reflected into an equatorially-trapped Rossby wave, which moves westward, reflecting at the western boundary into the Kelvin wave — thus completing a semi-closed loop by traveling-waves with 8-12 month period in the tropical Pacific basin (with some energy loss at the eastern boundary due to the poleward traveling coastal Kelvin wave; Jin, (1997)). Neelin and Jin (1993) mentioned that this ocean basin mode can be destabilized by the zonal advective feedback (i.e. zonal advection of the mean zonal temperature gradient by the anomalous zonal current). Once the ocean basin mode becomes unstable, it could be changed into the interannual mode, and have larger amplitude than the uncoupled ocean basin mode. An and Jin (2000) showed that the zonal temperature gradient of the mean SST during the 1961-75 is relatively larger than that during 1981-95, and it caused the destabilization of the ocean basin mode during the pre-1980s. In many respects, the leading NLPCA mode of the observations is consistent with such previous studies.

The evolution features are quite different for the post-1980s from those for the pre-1980s (Fig. 4.3). The standing structure in the sea level height has turned into eastward propagating patterns (Fig. 4.3e); the basin-wide pattern of the surface current disappears; and the westward moving tendency of SST changes to the eastward moving tendency (e.g., An and Wang 2000). The maximum surface current in the eastern Pacific (Fig. 4.3f) appears when the zonal gradient of the sea level height is at maximum (Fig. 4.3e), indicating that the surface current is mostly due to the local pressure gradient from the zonal mass difference than to the surface wind stress — the positive SST anomaly and the resulting convective atmospheric heat generate the positive wind stress anomaly in the western part of the center of the SST anomaly, which may enforce the westerly zonal surface current, but the zonal current anomaly is negative as shown here. An and Jin (2001), under the

two-box approximation of the intermediate ENSO model, theoretically proved this point, and mentioned that the two-box approximation could represent the ocean adjustment but not the ocean wave dynamics, thus only the recharge mode is possible. In this regard, the ENSO mode inferred from the NLPCA pattern for the post-shift regime is presumably the recharge mode due to the destabilization of ocean adjustment mode. Note that the lifetime and amplitude for the positive zonal current anomaly and those for the negative zonal current anomaly are not the same (Fig. 4.3f). This asymmetric oscillation was dominant during the post-1980s (An et al., 2005).

The phase relationships among the SST, sea level height, and surface zonal current appeared in the NLPCA mode give an idea on the role of the surface current for each decadal period. For the pre-1980s, as shown in Fig. 4.3, the sea level height anomalies over the equatorial eastern Pacific are almost in-phase with the surface zonal current anomalies. Since a positive (negative) surface zonal current anomaly generates a positive (negative) SST anomaly through the warm (cold) surface water advection by the eastward (westward) zonal current, the surface current plays a role in the intensification of this system. For the post-1980s, on the other hands, the surface zonal current anomalies in the equatorial Eastern Pacific lead the sea level height anomalies by about a quarter of a cycle. This suggests that the surface zonal current plays a role in the transition mechanism of this oscillation. Thus, in each climate regime, the role of the surface zonal current in ENSO evolution is different.

4.3 Summary

Using the nonlinear principal analysis (NLPCA) technique, we demonstrated that the leading ENSO mode in a physical basis changed since the late 1970s. The ENSO mode during the

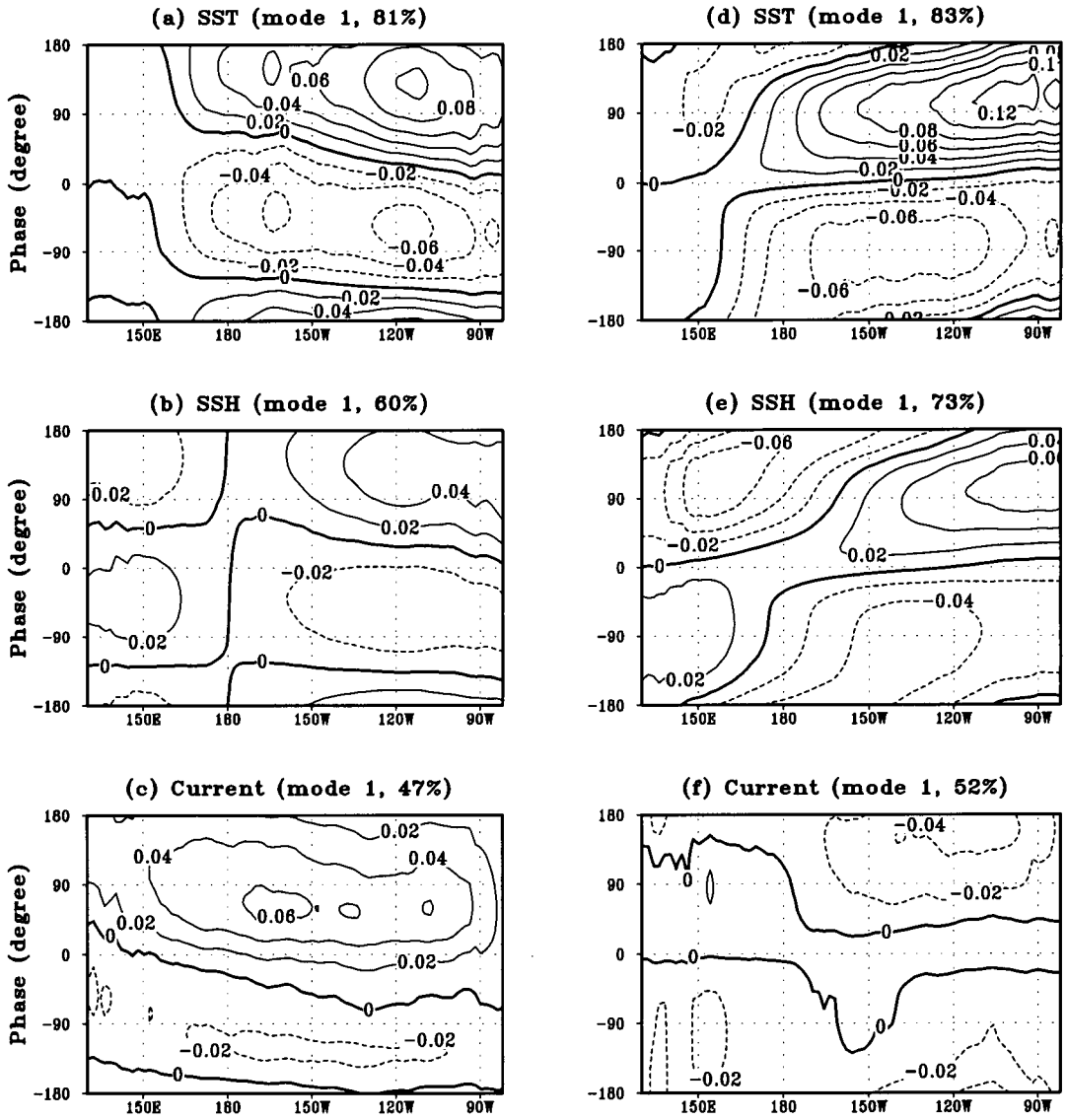

Figure 4.3: Phase-longitude section of the SST (top panels), sea level height (center panels), and the surface zonal current (bottom panels) anomalies over the equatorial band (5°S to 5°N) associated with the first NLPCA mode. (a) to (c) for the pre-1980s and (d) to (f) for the post-1980s.

pre-1980s resembles the destabilized 'ocean basin mode', while that during the post-1980s, 'the recharge-mode'. In particular, for the pre-1980s, the surface zonal current mainly acts as an intensifier of the ENSO, while that during post-1980s it plays a role in the transition of the ENSO cycle.

4.4 References

An S.-I., W. W. Hsieh, and F.-F. Jin, 2005: A nonlinear analysis of the ENSO cycle and its Interdecadal changes. *J. Climate*, 18, 3229-3239.

An S.-I., and F.-F. Jin, 2001: Collective role of thermocline and zonal advective feedbacks in the ENSO mode. *J. Climate*, 14, 3421-3432.

An S.-I., and F.-F. Jin, 2000: An eigen analysis of the Interdecadal changes in the structure and frequency of ENSO mode. *Geophy. Res. Lett.*, 27, 1573-1576.

An S.-I., and F.-F. Jin, 2004: Nonlinearity and asymmetry of ENSO. *J. Climate*, 17, 2399-2412.

An S.-I., A. Timmermann, L. Bejarano, F.-F. Jin, F. Justino, Z. Liu, and A. W. Tudhope, 2004: Modeling evidence for enhanced El Nino-Southern Oscillation amplitude during the Last Glacial Maximum. *Paleoceanography*, 19, PA4009, DOI:10.1029/2004PA001020.

An S.-I. and B. Wang, 2000: Interdecadal change of the structure of the ENSO mode and its impact on the ENSO frequency. *J. Climate* 13, 2044-2055.

Carton J., G. Chepurin, X. Cao, and B. Giese, 2000: A simple ocean data assimilation analysis of the global upper ocean 1950-95. Part I: Methodology. *J. Phys. Oceanogr.*, 30, 294-309.

Eisenman I., L. Yu, and E. Tziperman, 2005: Westerly wind bursts: ENSO's tail rather than the dog? *J. Climate*, 18, 5224-5238.

Fedorov A. V. and S. G. H. Philander, 2000: Is El Nino changing?. *Science*, 228, 1997-2000.

Jin F.-F., 1997: An Equatorial Ocean Recharge Paradigm for ENSO Part I: Conceptual Model, *J. Atmos. Sci.*, 54, 811-829.

Jin F.-F., and J. D. Neelin, 1993: Modes of interannual tropical ocean-atmosphere interaction - a unified view. Part I: Numerical results. *J. Atmos. Sci.*, 50, 3477-3503.

Neelin J. D., and F.-F. Jin, 1993: Modes of interannual tropical ocean-atmosphere interaction - a unified view. Part II: Analytical results in the weak-coupling limit. *J. Atmos. Sci.*, 50, 3504-3522.

Nitta T., and S. Yamada, 1989: Recent warming of tropical sea surface temperature and its relationship to the Northern Hemisphere circulation. *J. Meteor. Soc. Japan*, 67, 375-383.

Philander G. H, 1990: El Nino, La Nina, and the Southern Oscillation, *Academic Press*, pp 293.

Philander G. H., and A. Fedorov, 2003: Is El Niño sporadic or cyclic? *Annual Review of Earth and Planetary Sciences*, 31, 579-594.

Timmermann A., F.-F. Jin, and J. Abshagen, 2003: A nonlinear theory for El Nino bursting. *J. Atmos. Sci.*, 60, 152-165.

Trenberth K. E. and J. W. Hurrel, 1994: Decadal atmosphere-ocean variations in the Pacific. *Climate Dyn.*, 9, 303-319.

Wang B. and S.-I. An, 2001: Why the properties of El Niño changed during the late 1970s. *Geophys. Res. Lett.*, 28, 3709-3712.

Chapter 5

Changes in ENSO and associated overturning circulations from enhanced greenhouse gases [4]

5.1 Introduction

The global atmospheric and tropical oceanic surface temperatures increased in the past century by $> 0.5°C$ (Jones and Moberg, 2003; Anthes et al, 2006). This warming is, at least in part, a result of emissions of greenhouse gases (GHGs) from human activities (IPCC, 2001). The climate change caused by the emissions of GHGs from human activities will also change the tropical Pacific climate state. ENSO, the strongest interannual signal in the tropical Pacific, changes its characteristics with the change in the background climatology (Fedorov and Philander, 2001; An and Wang, 2000; Ye and Hsieh, 2006). Our primary interest here is to study how changes in GHGs from the pre-industrial level to the year 2000 level would impact ENSO.

There is debate in the climate literature as to whether the low-frequency change of

[4] A version of this chapter has been submitted to *Journal of Climate* for publication. Ye, Z. and Hsieh, W. W. (2006) Changes in ENSO and associated overturning circulations from enhanced greenhouse gases.

ENSO in the tropical Pacific is generated within the tropics by tropical internal instability (Knutson and Manabe, 1998), or uncoupled atmospheric noise (Thompson and Battisti, 2001; Flügel et al, 2004), or whether it involves the interaction between the extratropics and the tropics (Gu and Philander, 1997; Kleeman et al, 1999; Barnett et al, 1999). The zonal overturning circulation in the equatorial Pacific directly transports water mass and heat energy between the western warm pool and the eastern cool upwelling area in the tropical Pacific, while the shallow meridional overturning circulation conveys water mass and heat energy between tropical Pacific and subtropical Pacific. McCreary and Lu (1994) and Liu (1994) investigated the fundamental dynamics of the shallow meridional overturning circulation using simple layered thermocline models. They postulated that the subtropical water reaches the equator from the northeast subtropics via low-latitude western boundary currents or via an interior path directly linking the northeast subtropics to the central tropics.

There is also debate on whether the climate is changing into El Niño-like warming or La Niña-like cooling in the tropical Pacific. Cane et al (1997) found that the SST had a cooling trend in the eastern tropical Pacific from the 1900-1991 observations. However, the Intergovernmental Panel on Climate Change (IPCC) (2001) found that the trend for SST was El Niño-like in the tropical Pacific in many models. Meehl and Washington (1996) also noted an El Niño-like climate change in their coupled general circulation climate model (CGCM) with CO_2 doubling. This chapter will use the observed SST from 1900-1999 which was constructed using the most recently available International Comprehensive Ocean-Atmosphere Data Set (ICOADS) SST data and improved statistical methods that allow stable reconstruction using sparse data, including a modified historical bias correction for the 1939-1941 period.

The shallow meridional overturning circulation has been slowing down in the last decades during the period 1950-1999 (McPhaden and Zhang, 2002), though it rebounded during the short period 1998-2003 with respect to the period 1992-1998 (Zhang and McPhaden, 2004). According to Zhang and McPhaden (2006), there appeared to be a strong decadal variability superimposed on a linear weakening trend in the period 1953-2001. They found the shallow meridional overturning circulation in the tropical and subtropical Pacific to be highly anti-correlated with SST anomalies in the central and eastern tropical Pacific in the observational datasets over the period 1953-2001, and explored this relationship in the simulations of 20th century climate from 14 state-of-the-art coupled climate models, though the model results were unclear. The models had difficulty simulating this observed relation because they did not adequately simulate the ocean's response to remote forcing from the subtropical Pacific due to an underestimation of the extratropical winds (Solomon and Zhang, 2006). Using a coupled model, Merryfield and Boer (2005) found that anthropogenic forcing may have contributed to the observed slowdown of the shallow meridional overturning circulation. The zonal Walker circulation driven by convection in the western equatorial Pacific and subsidence in the east shows a weakening trend since the mid-19th century due to anthropogenic forcing (Vecchi et al, 2006). Here we will investigate the slowdown in the oceanic zonal and shallow meridional circulations using the multi-model ensemble based on 12 CGCMs in the 4th Assessment Report of the Intergovernmental Panel on Climate Change (IPCC-AR4) .

There is much uncertainty in how ENSO will change its characteristics (e.g. the amplitude and frequency) under increased GHG in the CGCMs. Guilyardi (2006) assessed the ENSO-mean state-seasonal cycle interactions in 23 coupled ocean-atmosphere models by comparing the pre-industrial control and the stabilized $2\times CO_2$ and $4\times CO_2$ scenario runs.

The ENSO amplitude was found to be an inverse function of both the mean trade winds and the relative strength of the seasonal cycle, but the relation was less clear for the ENSO frequency. Van Oldenborgh et al (2005) found very little influence of global warming on ENSO from the results of 17 models. Merryfield (2006) compared the differences in ENSO amplitude, period, and pattern under pre-industrial conditions and under CO_2 doubling: The amplitude changes were not strongly related to the magnitude or pattern of surface warming. A narrow (wide) wind stress response was associated with ENSO amplitude decrease (increase). The models exhibited a mean fractional decrease in ENSO period by about 5%, and an increase in the amplitude of SST variations in the central tropical Pacific. On the other hand, Meehl et al (2006) found that ENSO events decreased in magnitude in the future warmer climate ($2\times CO_2$, $4\times CO_2$ and other scenarios). Collin et al (2005) showed that the most likely scenario is for no large amplitude change toward mean El Niño or La Niña-like condition in the 20 models submitted to the coupled model inter-comparison project (CMIP) by comparing the 80-year control simulation with fixed CO_2 level and the 80-year simulation in which CO_2 was increased from the control value at a rate of 1% per year compounded. In this chapter, the changes in ENSO under the committed CO_2 level (i.e. the year 2000 CO_2 level) are examined. Finally, we point to the differences between this work and previous studies: While I have also used the datasets from IPCC-AR4, most previous studies trying to detect changes in ENSO used the data from the experiments under CO_2 doubling (2xCO2) or Special Report on Emissions Scenarios A2 (SRES-A2), instead of the PIcntrl and Commit experiments used here. Previous works tended to focus on the magnitude and frequency of ENSO oscillations, while here the focus is on the changes in the nonlinearity and in the tropical zonal and shallow meridional overturning circulations of ENSO.

ENSO displays considerable asymmetry between its warm phase (El Niño) and its cold phase (La Niña) (An, 2004; Rodgers et al, 2004). The asymmetry is due to the nonlinearity of the ENSO system, as the nonlinear dynamic heating in the tropical Pacific ocean heat budget is essential in producing decadal changes in ENSO nonlinearity and asymmetry (Jin et al, 2003; An and Jin, 2004). Changes in the asymmetry and nonlinearity of ENSO and associated overturning circulations are also addressed in our study.

The observed SST and the ensemble model data are described in Sec. 5.2 and Sec. 5.3, respectively. By comparing the ensemble model simulations under the pre-industrial GHG conditions and under the present conditions, we identified climate change in the tropical Pacific (Sec. 5.4), changes in the ENSO SST and zonal wind stress anomalies (Sec. 5.5), and changes in the ENSO ocean circulation (Sec. 5.6). A diagnostic analysis of the ocean surface temperature equation gave some explanation for the enhanced ENSO asymmetry (Sec. 5.7).

5.2 Observed SST

The NOAA extended reconstructed SST data (Smith and Reynolds, 2004) were used, with the data divided into the 1900-1949 and 1950-1999 periods. The climatological difference between the two periods suggests that the SST in the eastern-central tropical Pacific has increased by at least 0.3°C (Fig. 5.1). The climatological difference pattern resembles the El Niño pattern, with the maximum positive value in the eastern equatorial Pacific. The SST trend during 1900-1999 is also El Niño-like (Fig. 5.2).

Prior to calculating the composite maps for El Niño and La Niña episodes, a three-month running mean was applied after the climatological seasonal cycle and linear trend were removed in each period. We examined the composite maps of SST anomalies for El

Niño and La Niña episodes during each period (Fig. 5.3). El Niño and La Niña episodes were defined based on the Niño-3.4 index (i.e. the averaged SST anomalies over the region 5°S-5°N, 120°W-170°W exceeding ±1 standard deviation). Compared to the 1900-1949 period, a prominent eastward shift of positive SST anomalies appears over the eastern equatorial Pacific during El Niño in the 1950-1999 period. The maximum anomaly "H" has shifted from 120°W (5.3a) to east of 90°W (Figs. 5.3c), although the real center of mass of the anomaly pattern does not shift so far. During La Niña, a westward shift of negative SST anomalies is evident in the latter period, i.e. the shift during La Niña is in opposite direction compared to that during El Niño (5.3b and d). These shifts obviously enhanced the El Niño-La Niña asymmetry and nonlinearity in the latter period. To derive an index for the asymmetry, the SST composite (Fig. 5.3) for El Niño and that for La Niña were added together at each grid point, then the root-mean-square (RMS) deviation (averaged over the tropical Pacific) is a measure of the asymmetry, with a zero value indicating the La Niña pattern to be completely symmetrical to the El Niño pattern. The RMS deviation was 0.11°C for the period 1900-1949 and 0.19°C for 1950-1999, confirming the enhanced asymmetry in the latter period. This change in the asymmetry has a longer time scale (50 years) compared to the decadal change in ENSO asymmetry found after the late 1970s (Ye and Hsieh, 2006; Wu and Hsieh, 2003; An, 2004). To find a possible cause for this longer time scale change in ENSO, we will examine the effects of GHG forcing in the following sections.

5.3 Model data

Model data from the IPCC-AR4 database were downloaded from the archive hosted by the Program for Climate Model Diagnosis and Intercomparison (PCMDI). The 12 CGCMs

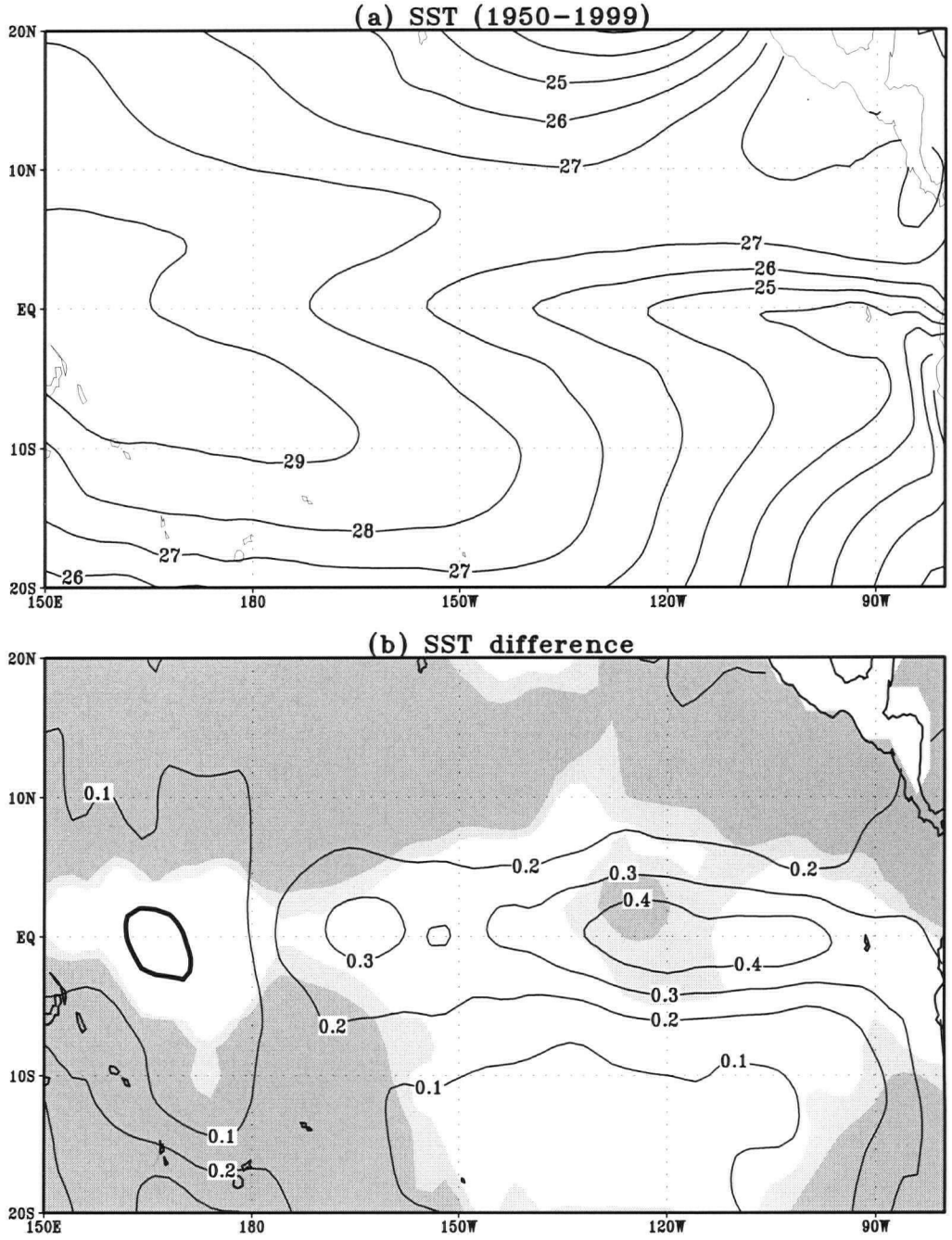

Figure 5.1: (a) The observed mean SST (in °C) during 1950-1999, and (b) the mean SST of 1950-1999 minus that of 1900-1949, with the 5% and 10% significance levels based on the t-test (von Storch and Zwiers, 1999, p. 115) shown in dark and light gray respectively.

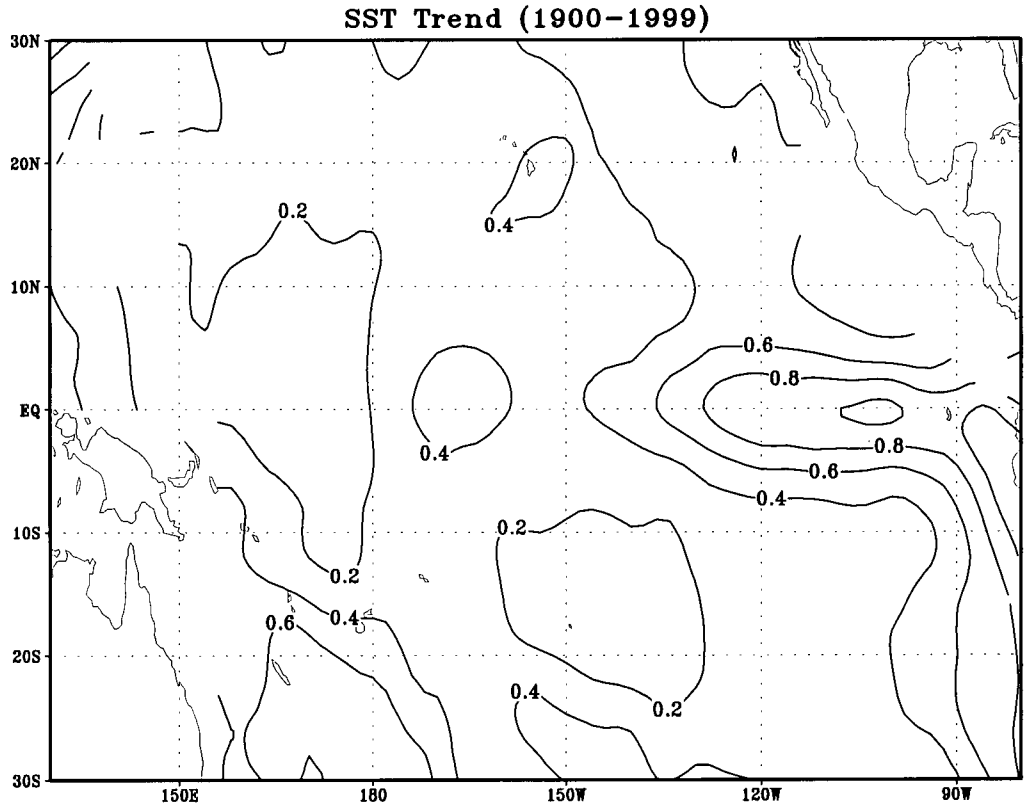

Figure 5.2: The trend in monthly mean SST anomalies for 1900 to 1999 in degrees Celsius per century (from NOAA ERSST).

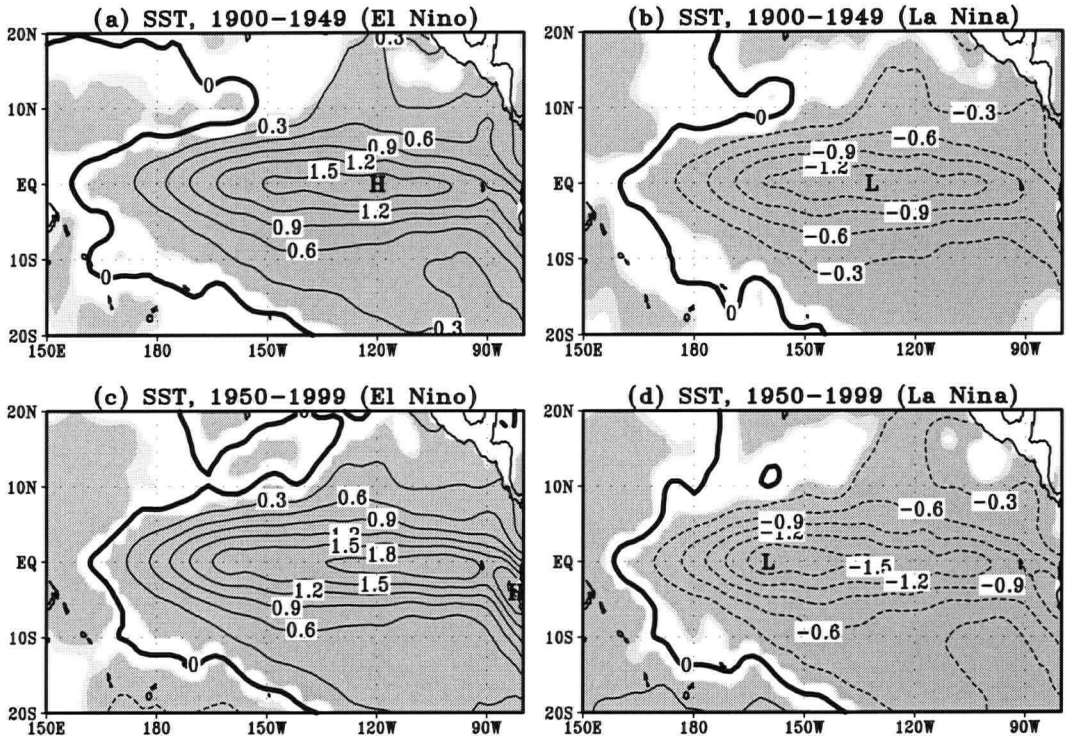

Figure 5.3: Composite maps of SST anomalies (in °C) during El Niño (left column) and during La Niña (right column), with (a) and (b) for the 1900-1949 regime, and (c) and (d) for 1950-1999. "H" and "L" mark the location of the highest and lowest values, respectively, and the 5% and 10% significance levels based on the t-test are shown in gray.

used here are the CCCMA-CGCM3-1, CNRM-CM3, CSIRO-MK3-0, GFDL-CM2-0, GISS-MODEL-E-R, IAP-FGOALS1-0-G, INMCM3-0, IPSL-CM4, MIROC3-2-MEDRES, MIUB-ECHO-G, MRI-CGCM2-3-2A and UKMO-HADCM3 (Table 5.1). The documentation for the models is available on the website `http://www-pcmdi.llnl.gov/ipcc/model_documentation/ipcc_model_documentation.php`. We consider the pre-industrial control runs (PIcntrl) and the Commit runs (Commit). PIcntrl is the pre-industrial climate simulation with GHG-induced forcing fixed at the level of year 1850, whereas Commit simulates committed climate change using the forcing (GHG + aerosols) at year 2000 levels. For each simulation run, 100 years of data were taken from each of the 12 models.

Model	Institution (country)	Atmosphere resolution	Ocean resolution
CGCM3.1 (T47)	CCCMA (Canada)	T47L31	1.85°×1.85°L29
CNRM-CM3	Meteo-France/CNRM (France)	T63L45	2°×0.5°L31
CSIRO-MK3.0	CSIRO (Australia)	T63L18	1.875°×0.84°L31
GFDL-CM2.0	GFDL (USA)	2.5°×2°L24	1°×0.33°L50
GISS-ER	NASA/GISS (USA)	5°×4°L20	5°×4°L13
IAP-FGOALS-g1.0	LASG/IAP (China)	T42L26	1°×1°L33
INM-CM3.0	INMCM (Russia)	5°×4°L21	2.5°×2°L33
IPSL-CM4	IPSL (France)	2.5°×3.75°L19	2°×0.5°L31
MIROC3.2 (medres)	CCSR/NIES/FRCGC (Japan)	T42L20	1.4°×0.5°L43
MIUB-ECHO-g	MIUB/ (Germany)	T30 L19	T42L20
MRI-CGCM2.3.2A	MRI (Japan)	T42L30	2.5°×0.5°L23
UKMO-HadCM3	HadleyCentre (UK)	3.75°×2.5°L19	1.25°×1.25°L20

Table 5.1: The models used in present Chapter, including their configurations near the equator.

For all models, the tropical Pacific SST and zonal wind stress (WS) were analyzed. The zonal current in 2°S-2°N and the meridional current in 30°S-30°N from the sea surface to 450 m depth were also analyzed. The meridional currents averaged over 100 m to 300 m depth were used to detect the shallow meridional overturning circulation in the region 30°S-30°N in the Pacific. The temperature and vertical velocity in the equatorial Pacific region (5°S-5°N, 0-50m) were also used in the diagnostic analysis.

For each model, the monthly mean SST, WS, ocean upper level velocities were interpolated onto a 5° longitude by 4° latitude regular grid (identical to that used in the GISS-ER model) using bi-linear interpolation. Anomalies were computed with respect to the mean seasonal cycle in each specific model simulation.

5.4 Climate change simulated

In this section, we focus on the human-induced impacts on the SST in the tropical Pacific and the three large-scale circulations (Fig. 5.4) in the upper tropical and subtropic Pacific from 30°S to 30°N area. The three circulations are shown in the schematic figure with shade area standing for the northern Pacific water in upper layer (Fig. 5.4).

The climate change induced by the anthropogenic forcing were computed by subtracting the multi-model ensemble mean in the PIcntrl experiment from that in the Commit experiment. The warm pool in the western tropical Pacific and the cool tongue in the eastern tropical Pacific were both reproduced well in the mean climate in the Commit experiment (Fig. 5.5a), although there is a cool model bias (up to 1°C) in the east-central equatorial Pacific Ocean and an exaggerated westward extent of the cold tongue (cf. Fig. 5.1a). These biases have been recognized as a common problem in most of the state-of-the-art coupled models which have a double Inter-Tropical Convergence Zone (ITCZ) (Zhang and Wang,

2006; Dai, 2006). Xie et al (2006) found that the interaction between the low-cloud and SST over the eastern tropical Pacific played an important role in generating and maintaining the single ITCZ in their numerical model. The difference between the means of the two experiments shows nearly 1°C warming over all of tropical Pacific (Fig. 5.5b), with the warming pattern vaguely resembling the El Niño pattern which has the maximum centered in the eastern-central equatorial Pacific. While every model revealed an El Niño-like pattern of SST change (Fig. 5.6), there is considerable variability in the exact location of, e.g., the maximum warming center which ranged from the eastern to the western equatorial Pacific. Therefore the standard deviation of the SST change in Fig. 5.5c is large. The large spatial spread (in tropical western/eastern Pacific) in the maximum SST anomalies in the simulated ENSO behavior was also found by Saji et al (2006), in the simulated twentieth-century data from 17 models in IPCC-AR4 dataset. Their results showed that the models exhibited poor ability in simulating ENSO's seasonality and in the phase locking to the annual cycle. Only one of 17 models appears to resemble to the observed temporal evolution.

The difference between the means of the two experiments also showed a positive zonal WS pattern in the western tropical Pacific (Fig. 5.5e), which also resembles the zonal WS anomaly pattern found during El Niño (shown later). The enhanced GHG forcing decreased the mean easterlies (Fig. 5.5d) along the western equatorial Pacific (Fig. 5.5e). This agrees with the finding that the Walker circulation has been slowing down in the tropical atmosphere since the mid-19th century (Vecchi et al, 2006), as the trade wind blowing across the tropical Pacific from east to west is associated with the bottom branch of the zonal Walker circulation. Fig. 5.5e also showed a strengthening of the easterlies south of 10°S. The inter-model variability of the zonal WS change (Fig. 5.5f) revealed that the models were most consistent with each other along the equatorial belt.

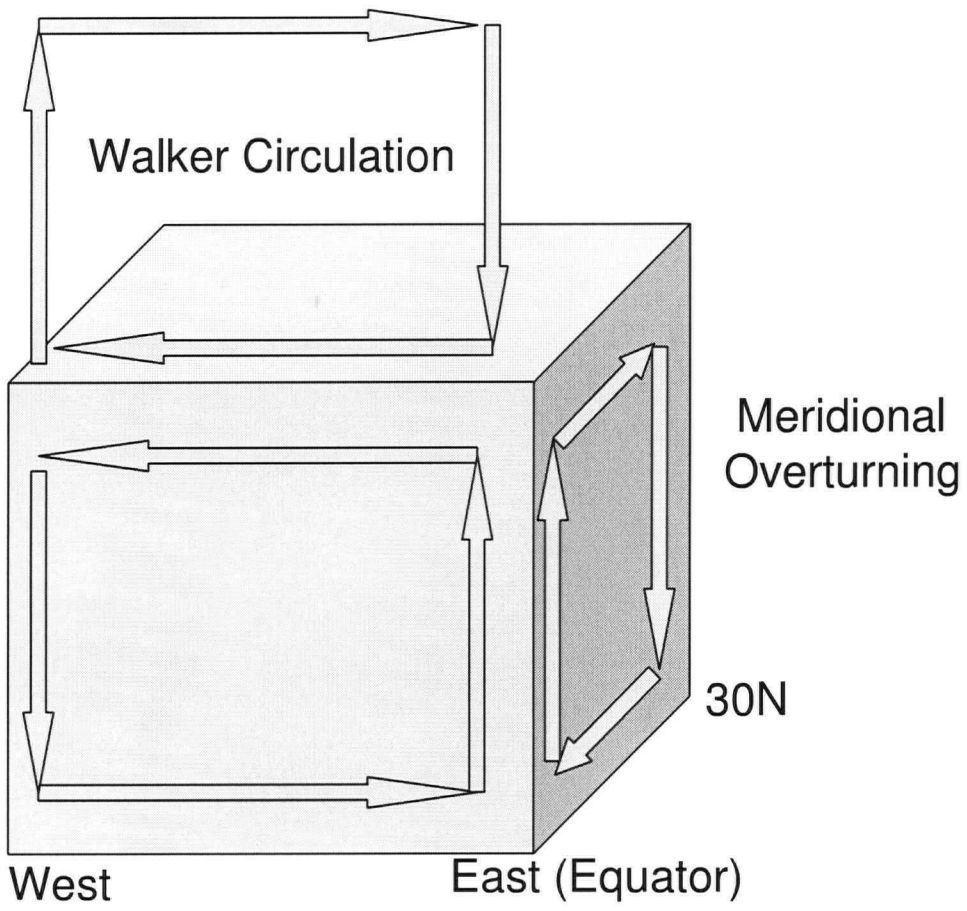

Figure 5.4: Schematic view of upper ocean (0-500 m depth) circulations in the Pacific from 0° to 30°N.

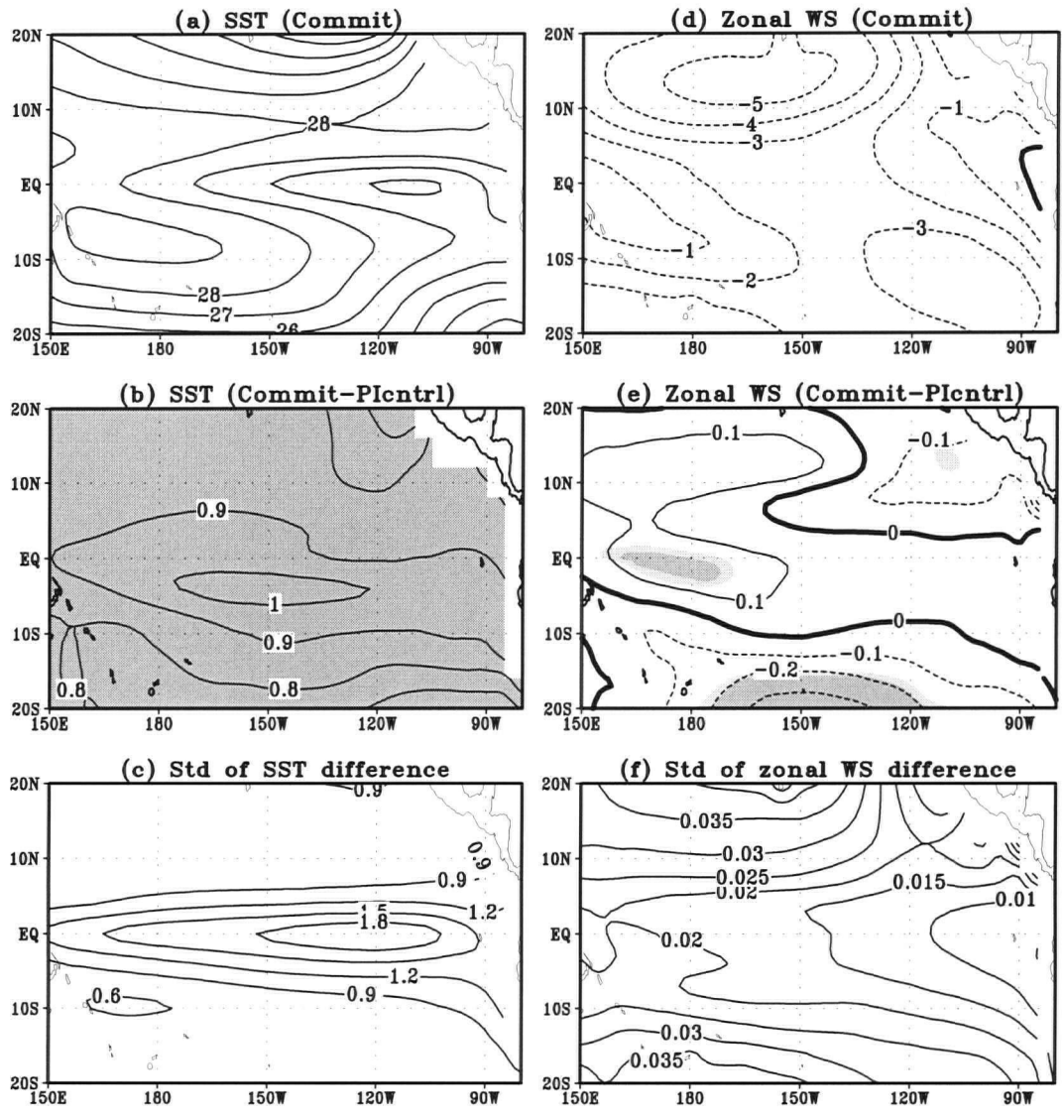

Figure 5.5: The multi-model ensemble mean for the Commit runs, its difference from the mean for the PIcntrl runs, and the standard deviation of the difference: (a) mean SST (°C), (b) the difference in the mean SST, (c) the standard deviation of the SST difference, (d) the mean zonal WS (0.01 Pa), (e) the difference in the mean zonal WS, and (f) the standard deviation of the WS difference. The 5% and 10% significance levels from the *t*-test are shown in gray in (b) and (e).

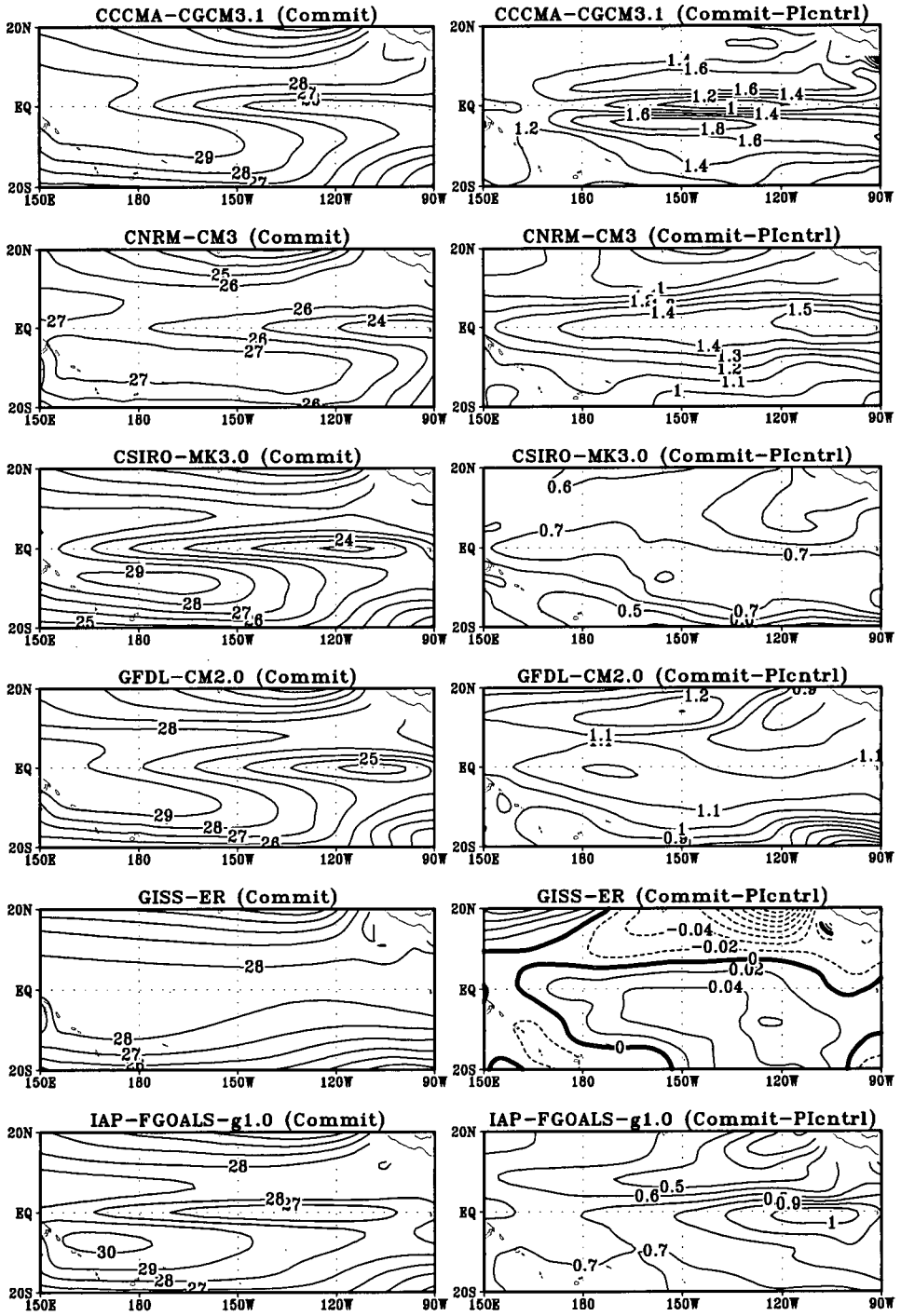

Figure 5.6: SST mean (°C) for the Commit runs (left) and its difference from the mean in the PIcntrl runs (right) for 12 individul models.

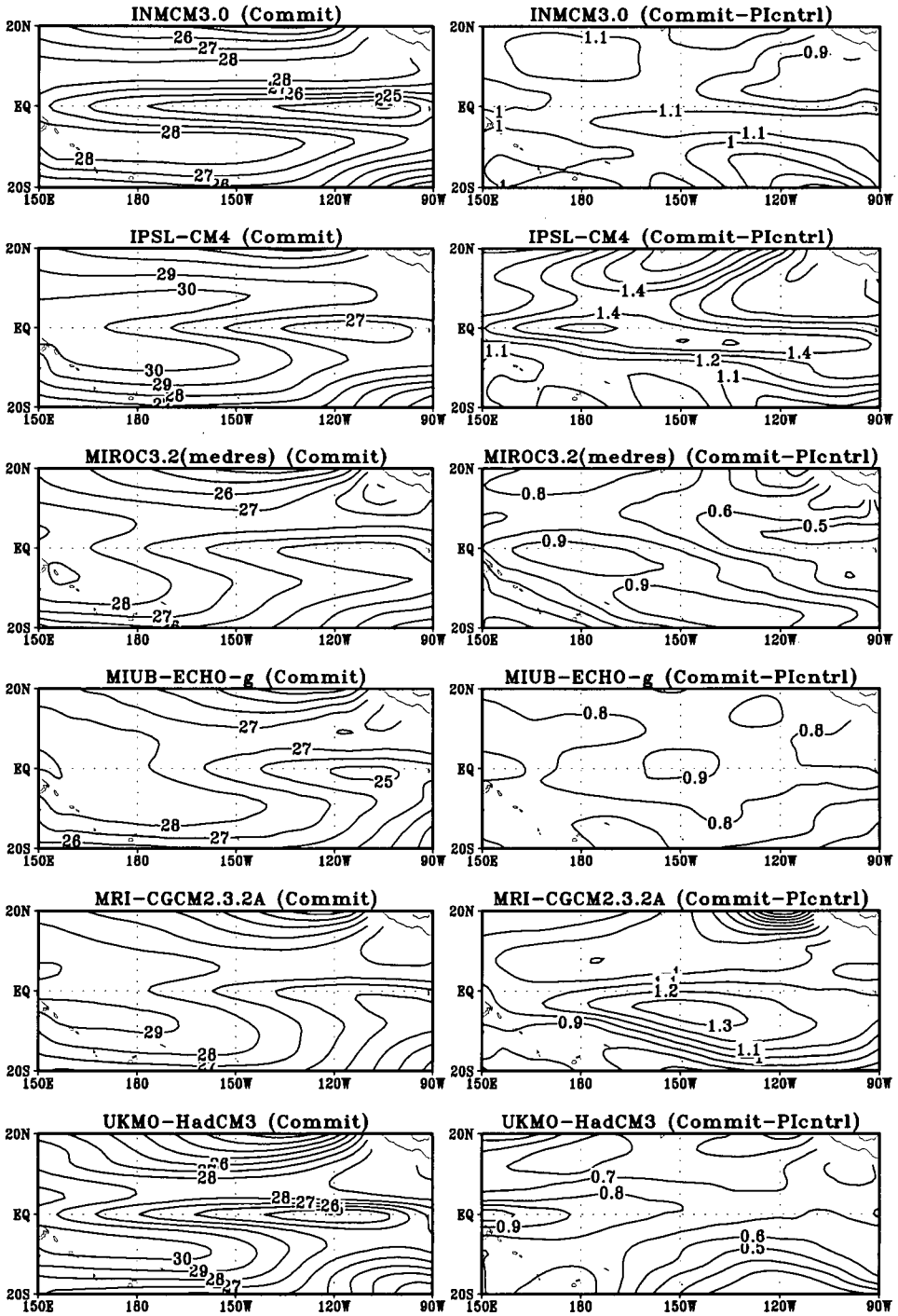

Figure 5.6 (Continued)

The zonal current along the equator (averaged over 2°S to 2°N) showed general consistency among the 12 individual models (Fig. 5.7). Although the simulated equatorial undercurrent along the thermocline is not as strong as the observed values (maximum is up to 100 cm s^{-1} in the observations) in most of the models in the subsurface layer, all models have simulated the equatorial undercurrent (left panels of Fig. 5.7). The differences between the Commit run and PIcntrl run also showed general consistency among the 12 models (right panels of Fig. 5.7). The zonal current in all models have eastward zonal current anomalies near the surface and westward zonal current anomalies near the subsurface. In the other words, the zonal equatorial overturning circulations tend to slow down in all 12 models in the Commit runs compared to the PIcntrl runs.

In the multi-model ensemble mean of the zonal current, the equatorial undercurrent along the thermocline in the subsurface layer (Fig. 5.8a) is not as strong as observed current (with a maximum of about 100 cm s^{-1}). The overturning equatorial circulation has weakened as shown in the difference between the means from the Commit and PIcntrl experiments (Fig. 5.8b), while the undercurrent has shifted upward in the Commit runs, as Vecchi et al. (2006) have also noted an upward trend in the undercurrent position in the GFDL-CM2.1 simulation data during 1861-2000. As the observed Walker circulation in the tropical atmosphere has been weakening in recent decades, Vecchi et al. felt that global warming was a likely causative factor in the weakening of the wind pattern. Here the simulated results confirm that the overturning oceanic circulation in the equatorial Pacific has also been weakening between PIcntrl and Commit.

Next consider the meridional currents which are important for interactions between the tropics and the extratropical Pacific, as studies have shown that extratropical effects influence the tropical ENSO (Gu and Philander, 1997; Kleeman et al, 1999). Observations

indicated that the cool water in the subtropical Pacific, especially in the eastern area, is subducted down and moved to the tropics by the shallow meridional overturning circulation in the upper Pacific (McPhaden and Zhang, 2004). The Pacific overturning circulation can be presented by the meridional oceanic velocity in the tropical and subtropical Pacific. The difference in the mean subsurface current (Fig. 5.8d) between the Commit and PIcntrl runs shows the Pacific shallow meridional overturning circulation (Fig. 5.8c) tending to slow down, especially in the western tropical Pacific. The recent observed evidence suggests that there does exist such a slowdown of the shallow meridional overturning circulation in the upper Pacific Ocean since the 1970s (McPhaden and Zhang, 2002). Although McPhaden and Zhang (2004) found that the shallow meridional overturning circulation rebounded during 1998-2003, their latest result showed that there was a slowdown trend overlying the decadal variability in the shallow meridional overturning circulation during 1953-2000 (Zhang and McPhaden, 2006). Figs. 5.8c and d indicate that this slowdown in the shallow meridional overturning circulation is at least partially due to the increased GHG forcing. Fig. 5.8d also shows that the slowdown of the overturning circulation occurs along the interior path. In Fig. 5.8d, the changes in the 100-300 m mean meridional velocity within 7°N/S are likely in response to changes in equatorial zonal wind (Fig. 5.5e), while the changes in the shallow meridional overturning circulation beyond the equatorial belt are associated with wind changes outside the equatorial belt (Nonaka et al, 2002).

The difference in the mean between the Commit runs and PIcntrl runs also show that the GHG-induced changes are El Niño-like patterns in the tropical Pacific SST. In the next two sections, El Niño-like patterns are also found in the changes of the zonal WS, zonal overturning circulation and shallow meridional overturning circulation. The observed El Niño-like pattern in SST (Fig. 5.1b) therefore appears at least in part contributed by the

GHG forcing.

5.5 Changes in the ENSO SST and zonal WS

The data from GISS-ER and IAP-FGOALS-g1.0 are excluded in the analysis from now on due to no ENSO variability in the GISS-ER model (Guilyardi, 2006) and the very small seasonal cycle with the unrealistic regular interannual cycle in the IAP-FGOALS-g1.0 model (Guilyardi, 2006; Van Oldenburg et al, 2005). To identify El Niño and La Niña episodes in the model data, the simulated SST anomalies in the tropical Pacific (150°E-80°W, 20°S-20°N) were smoothed by a 25-month running mean, [as the period of the simulated ENSO was greater than 2 years in all 10 coupled models (Guilyardi, 2006)], then the leading PC of the smoothed SST anomalies was defined as a proxy ENSO index for each model run, with El Niño/La Niña defined based on the proxy ENSO index exceeding ± 1 standard deviation. Composite maps of El Niño and La Niña for various variables (without the 25-month running mean smoothing) were computed for each individual model. The multi-model ensemble mean for each variable was then calculated from the individual composite maps.

ENSO is an interactive thermodynamic system between the atmosphere and ocean, where the atmosphere dynamically forces the ocean by the surface WS, while the ocean thermally drives the atmosphere by heating/cooling. Multi-model ensemble means of composite maps for SST and zonal WS anomalies over the tropical Pacific are shown in Fig. 5.9. A pronounced shift in the zonal location of positive SST anomalies during El Niño occurred in the Commit runs relative to the PIcntrl runs (Figs. 5.9a and c). The shift is in the same direction as observed (Figs. 5.3a and c), but there is model bias since the model SST anomalies are located further west than the observed during El Niño, as noted by Capotondi

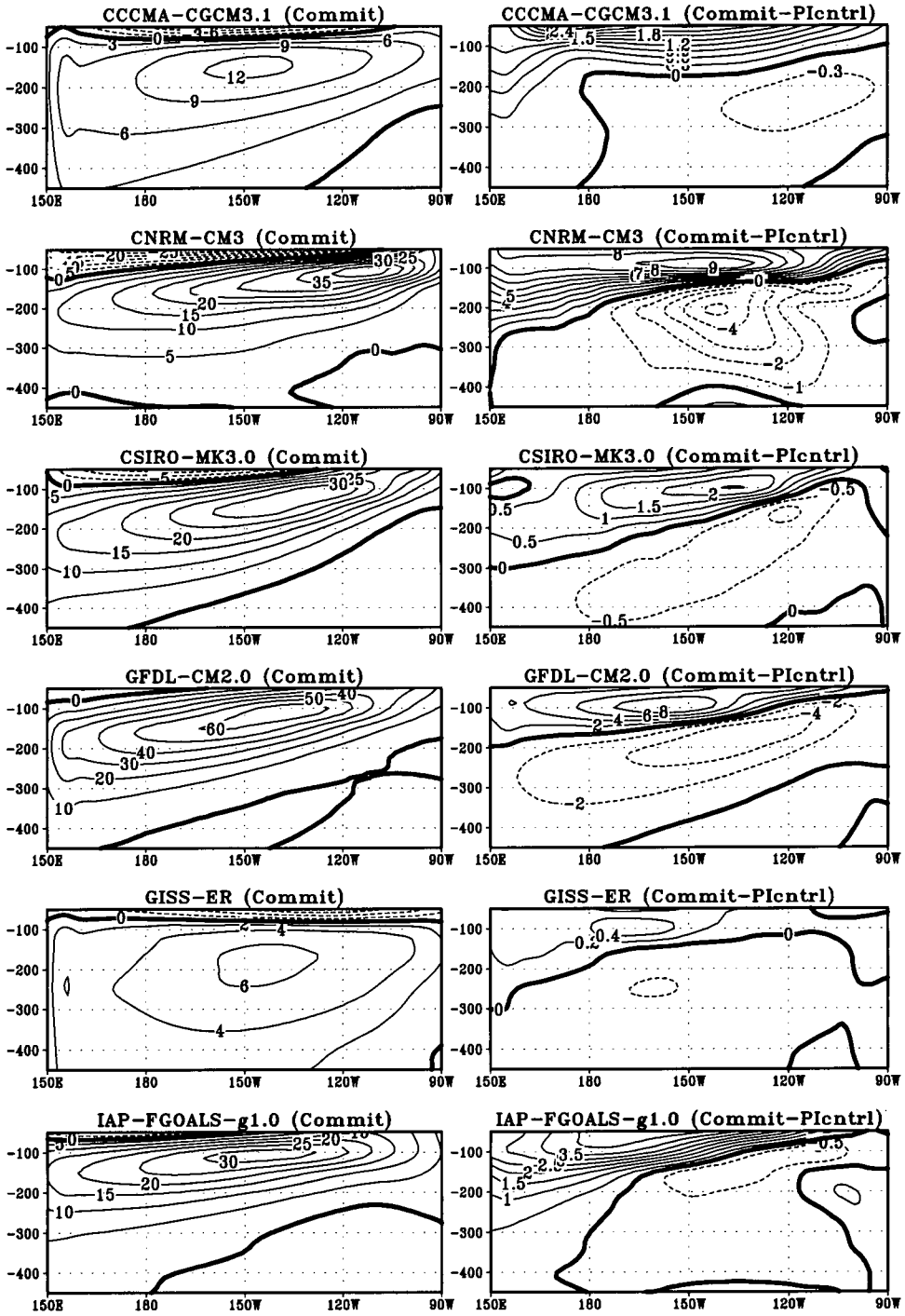

Figure 5.7: The zonal mean velocity (averaged over 2°S and 2°N in cm s^{-1}) for the Commit runs (left) and its difference from that in the PIcntrl runs (right) for 12 individual models.

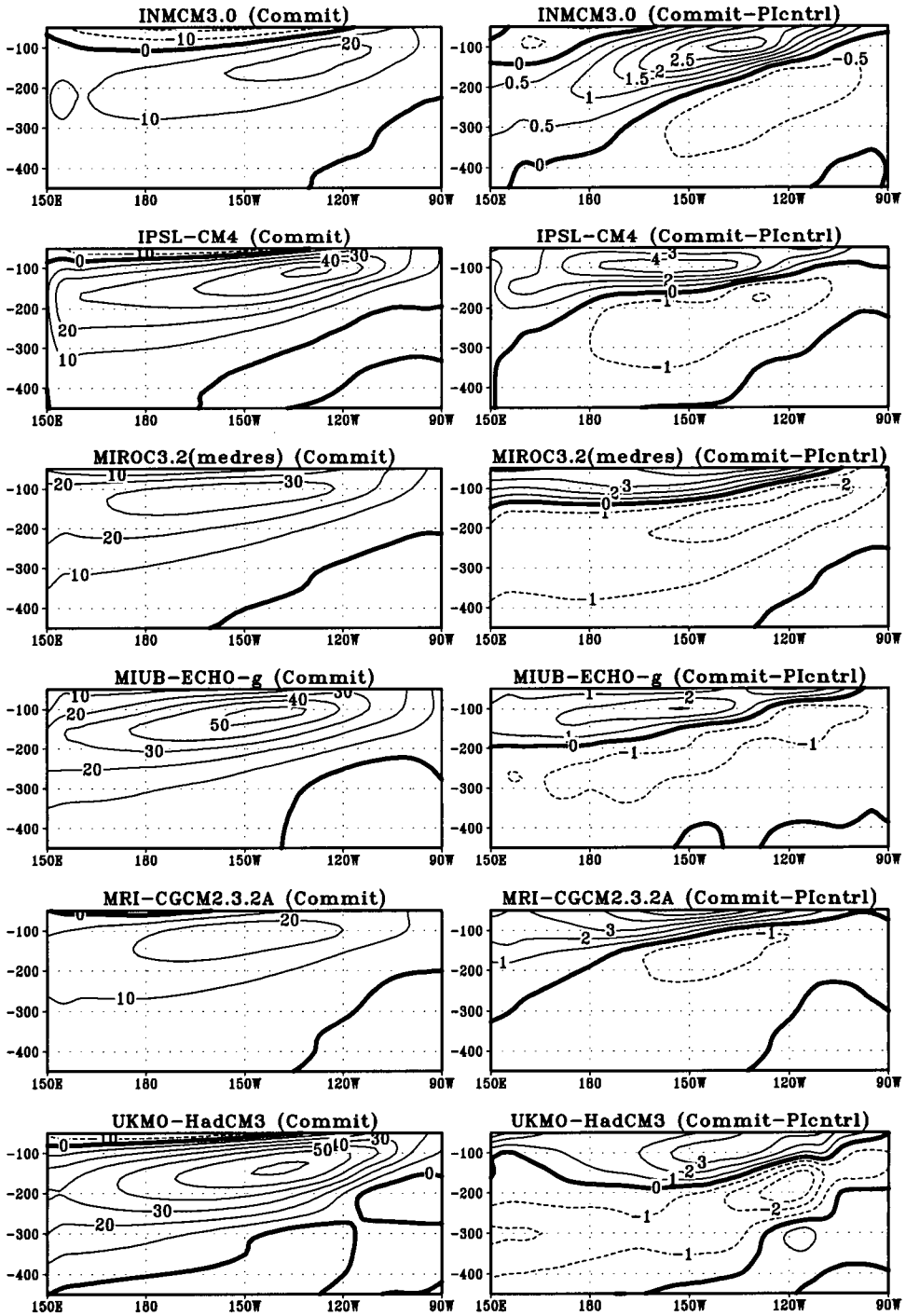

Figure 5.7 (Continued)

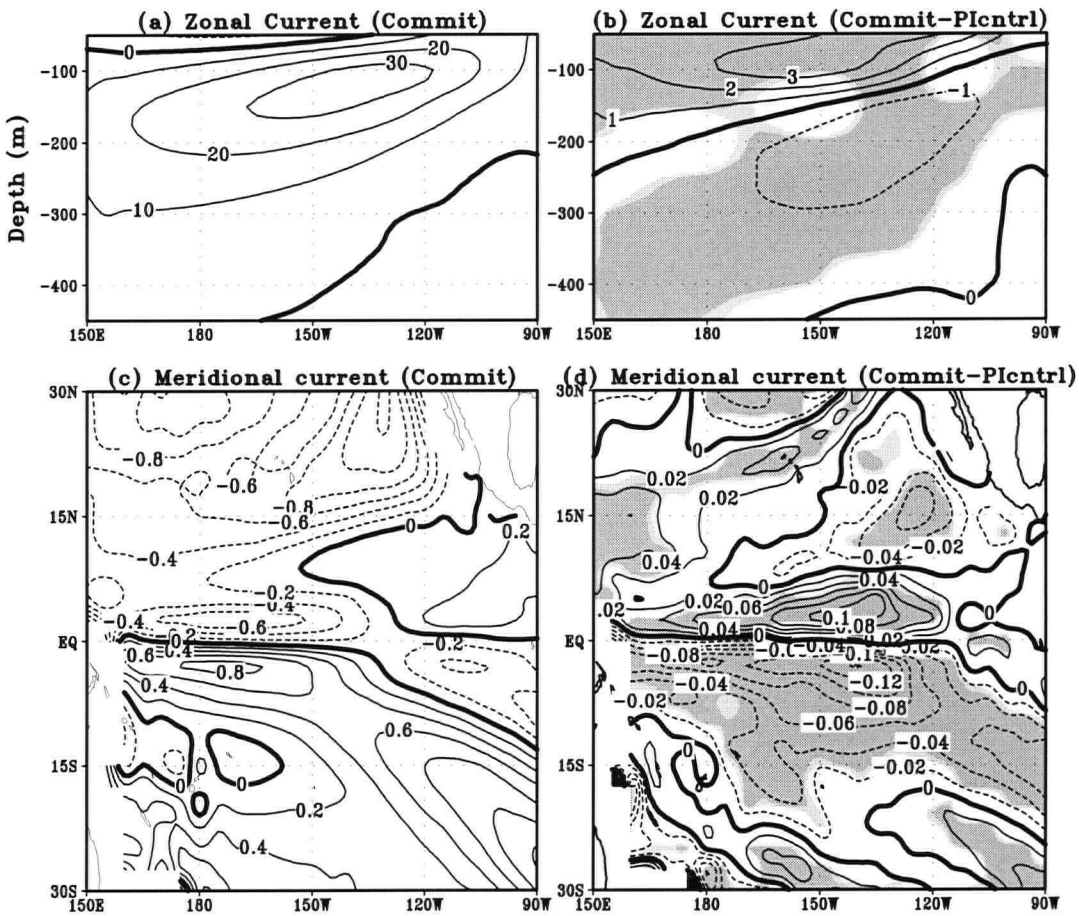

Figure 5.8: The multi-model ensemble mean of velocity (in cm s^{-1}) for the Commit runs and its difference from that in the PIcntrl runs: (a) the mean zonal velocity (averaged over 2°S and 2°N), (b) the difference in the mean zonal velocity, (c) the mean meridional velocity averaged over 100 - 300 m depth, and (d) the difference in the mean meridional velocity. The 5% and 10% significance levels from the t-test are shown in gray in (b) and (d).

et al (2006). During La Niña, the shift of the negative SST anomalies is undistinguished between the Commit and PIcntrl runs (Figs. 5.9b and d), missing the westward shift of anomalies in the observational data (Figs. 5.3b and d). The RMS index of the asymmetry between El Niño and La Niña was computed to be 0.045 °C averaged for the PIcntrl runs and 0.057 °C for the Commit runs. Although these values are considerably weaker than the observed values given in Sec. 5.2, they indicate the increase of ENSO asymmetry with increased GHG.

For the zonal WS during El Niño, there was eastward shift and strengthening of the westerly anomaly center along the equator (as indicated by "H") in the Commit runs relative to the PIcntrl runs (Figs. 5.9e and g), while during La Niña, the easterly WS anomalies along the equator showed no obvious shift (5.9f and h). The contrast in the WS shift between El Niño and La Niña meant that the asymmetry and nonlinearity of ENSO were enhanced in the Commit runs. The RMS index of asymmetry for the zonal WS was 0.078 (in 0.01Pa) for the PIcntrl runs and 0.100 (in 0.01 Pa) for the Commit runs. The change in the asymmetry and nonlinearity of ENSO in these experiments is similar to the observed change after the late 1970s on the decadal time scale (Wu and Hsieh, 2003; An, 2004).

5.6 Changes in the ENSO ocean circulation

In the vertical section showing zonal currents along the equator, during El Niño the westward subsurface zonal current anomaly strengthened slightly and "L" shifted eastward and upward in the Commit runs relative to the PIcntrl runs (Figs. 5.10a and c); in contrast, during La Niña, "H" in the eastward subsurface zonal current anomaly shifted slightly to the west (Figs. 5.10b and d). Thus the asymmetry in the zonal current anomalies between El Niño and La Niña strengthened in the Commit runs relative to the PIcntrl runs, as the

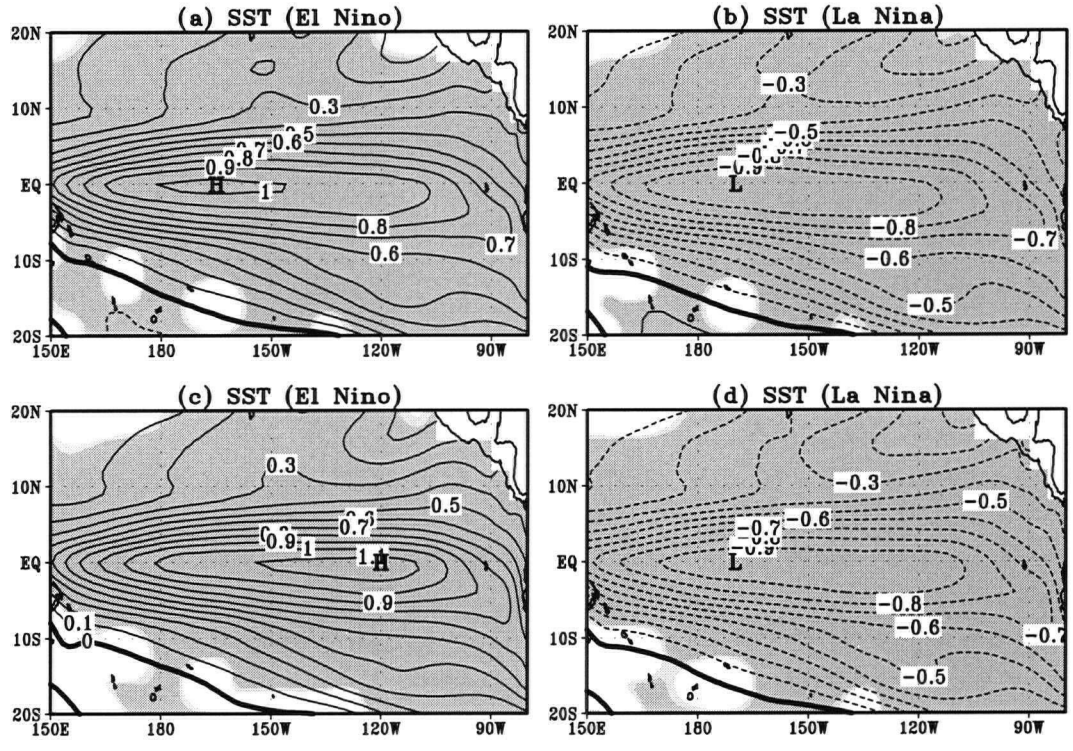

Figure 5.9: Multi-model ensemble mean of SST (°C) and zonal WS (0.01 Pa) composites for El Niño (left panels) and La Niña (right panels), with (a), (b), (e), (f) for the PIcntrl runs and (c), (d), (g), (h) for the Commit runs. "H" and "L" mark the location of the highest and lowest values, respectively, and the 5% and 10% significance levels from the t-test are shown in gray.

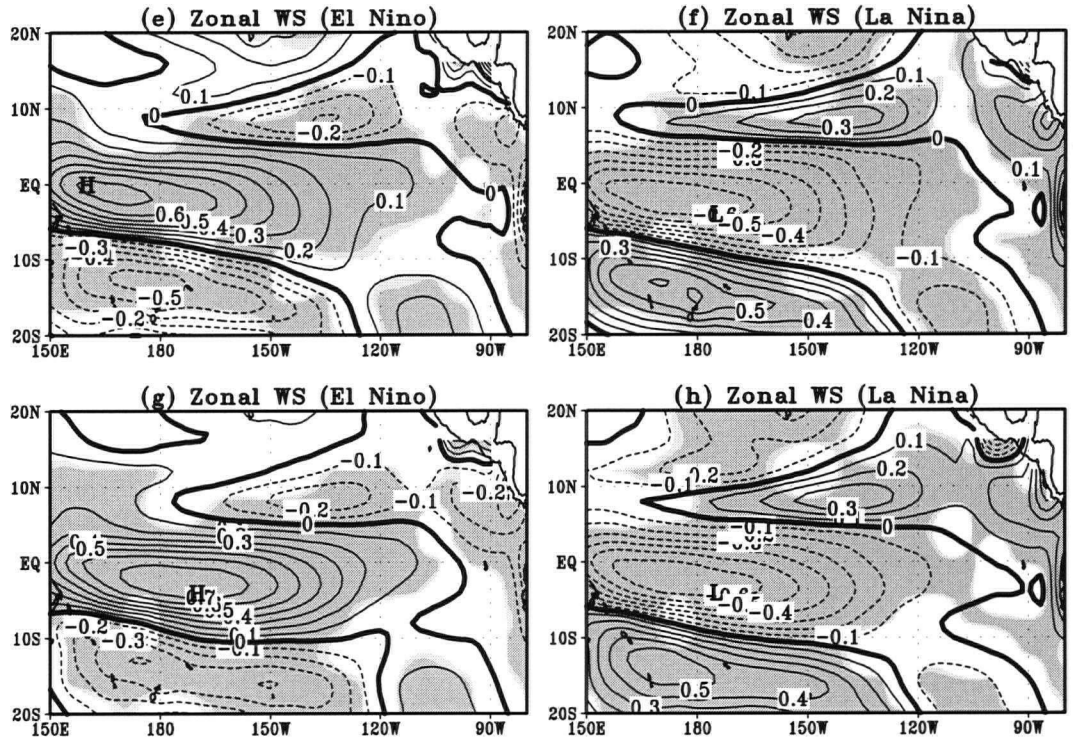

Figure 5.9 (Continued)

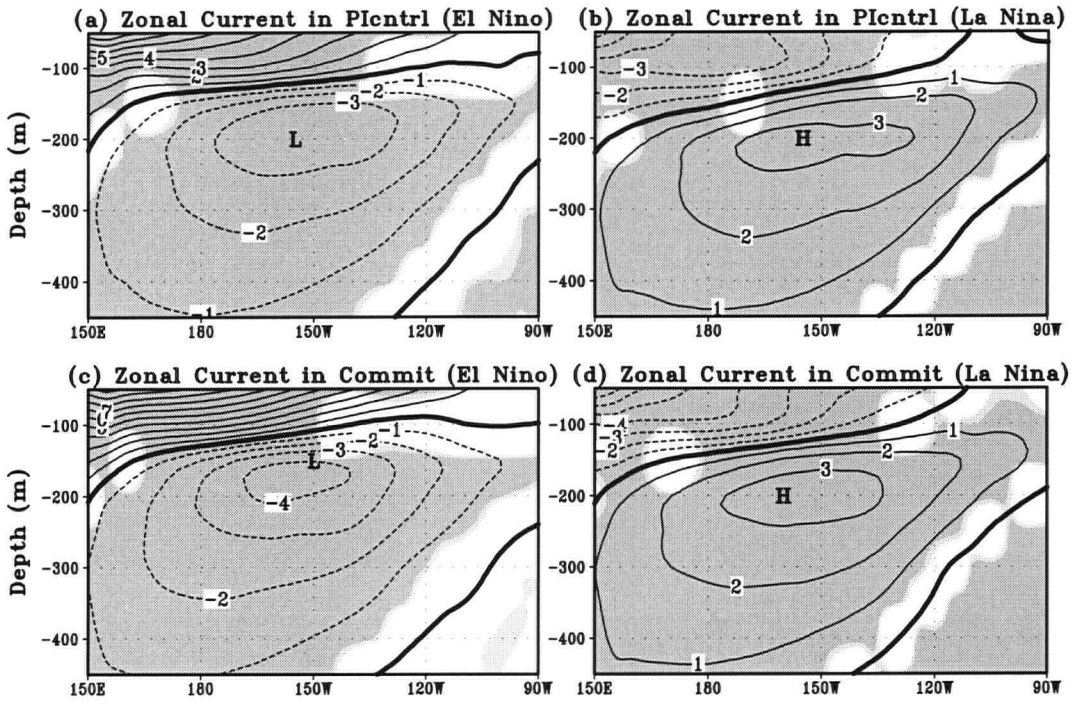

Figure 5.10: Vertical section along the equator showing the multi-model ensemble mean of zonal velocity anomalies (cm s^{-1}) (averaged between 2°S and 2°N) for the composite El Niño (left panels) and La Niña (right panels), with (a) and (b) for the PIcntrl runs, and (c) and (d) for the Commit runs. The 5% and 10% significance levels from the t-test are shown in gray.

RMS index of asymmetry was 0.77 cm s^{-1} for the PIcntrl runs and 1.01 cm s^{-1} for the Commit runs.

In both the El Niño and La Niña composites (Fig. 5.11), the subsurface meridional currents averaged between 100 - 300 m depth clearly showed the interior path (McCreary and Lu, 1994, Liu, 1994) running from the eastern subtropical Pacific Ocean to the central tropical Pacific Ocean. In the equatorial area, the location of "L" (the strongest southward current anomaly) during El Niño was found to have shifted eastward by 10° in the Commit

runs relative to the PIcntrl runs (Figs. 5.11a and c), whereas during La Niña, "H" showed no obvious shift between Figs. 5.11b and d. The RMS index of asymmetry (computed between 5°S-5°N) was 0.20 cm s^{-1} for the PIcntrl runs and 0.32 cm s^{-1} for the Commit runs. Hence the asymmetry in the subsurface meridional current anomalies between El Niño and La Niña was enhanced in the Commit runs relative to the PIcntrl runs.

5.7 Diagnostic analysis of the surface temperature equation

The ocean surface temperature anomaly equation can be written as

$$\begin{aligned} \frac{\partial T}{\partial t} &= -\left(\overline{u}\frac{\partial T}{\partial x} + \overline{v}\frac{\partial T}{\partial y} + \overline{w}\frac{\partial T}{\partial z} + u\frac{\partial \overline{T}}{\partial x} + v\frac{\partial \overline{T}}{\partial y} + w\frac{\partial \overline{T}}{\partial z}\right) \\ &\quad -\left(u\frac{\partial T}{\partial x} + v\frac{\partial T}{\partial y} + w\frac{\partial T}{\partial z}\right) + \text{residuals}, \end{aligned} \tag{5.1}$$

where T, u, v, w are, respectively, anomalies of the SST, zonal, meridional and vertical ocean velocities with respect to the climatological mean variables (indicated by the overbar), and "residuals" include the SST diffusion, subgrid-scale effects, etc. (An and Jin, 2004). The first bracketed term on the right hand side of (5.1) represents the linear dynamic heating (LDH) in the surface ocean, and the second bracketed term, the nonlinear dynamic heating (NDH).

Since the vertical ocean velocities of the models MIUB-ECHO-g and UKMO-HadCM3 were not available, these two models were excluded in the subsequent analysis. The temperature equation was applied to the surface ocean layer, where the average of the SST and velocities values over 0-50 m depth was used to represent the surface layer. The vertical temperature gradient was computed from the difference between the temperature at 0 m and that at 50 m depth. Averaged over time, the SST tendency contributed by the LDH terms is very small compared to the contribution from the NDH terms. Among the three

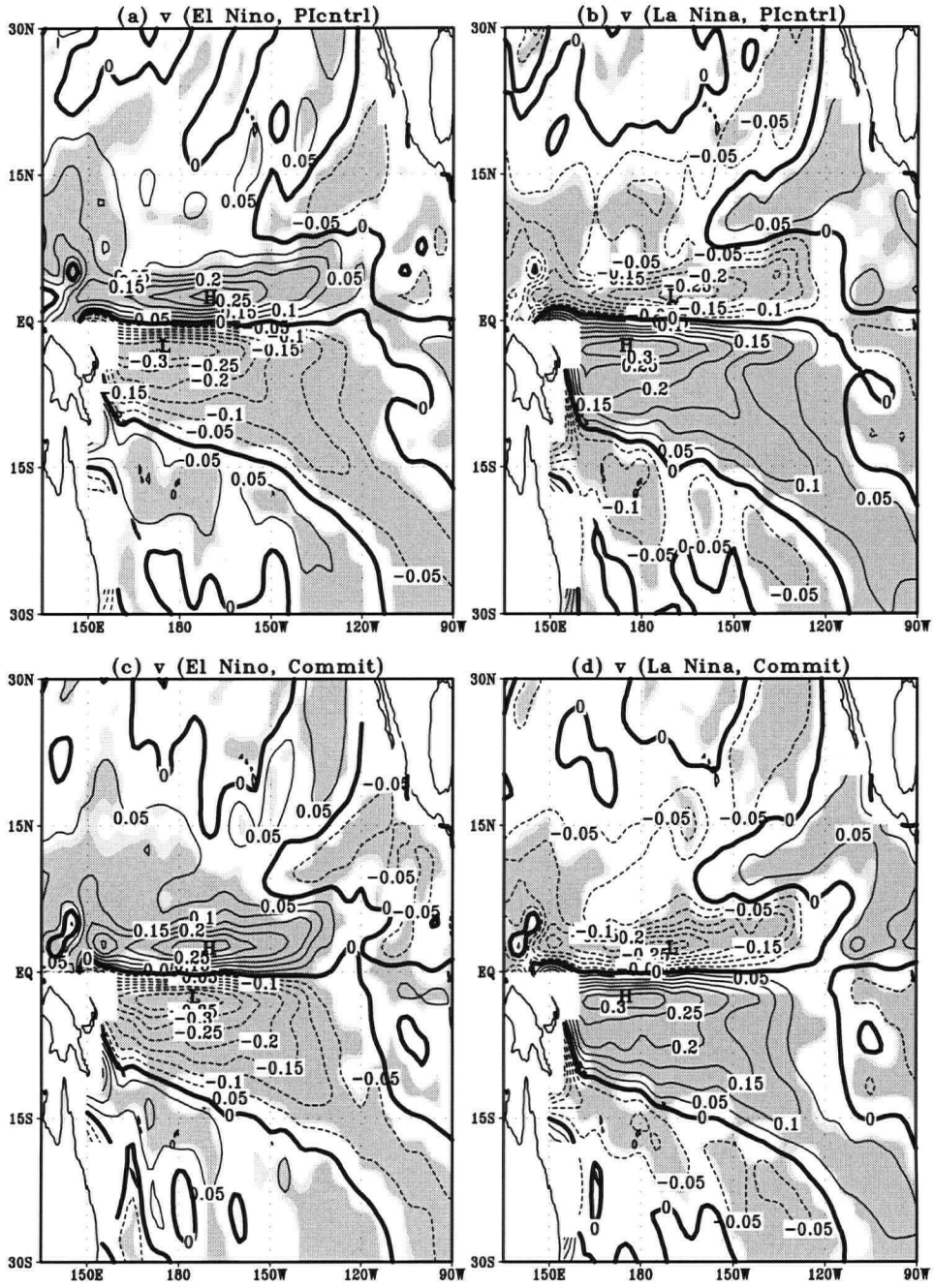

Figure 5.11: Multi-model ensemble mean of subsurface meridional velocity anomalies (cm s^{-1}) (averaged over 100-300 m depth) for the composite El Niño (left panels) and La Niña (right panels), with (a) and (b) for the PIcntrl runs, and (c) and (d) for the Commit runs. The 5% and 10% significance levels from the t-test are shown in gray.

NDH terms, the vertical term $-w\frac{\partial T}{\partial z}$ is dominant (Figs. 5.12e and g; f and h). The NDH is about 30% stronger in the Commit runs than in the PIcntrl runs (Figs. 5.12f or h). The enhanced NDH in the Commit runs does not correspond to enhanced upwelling, instead the weakened upwelling (Figs. 5.12c and d) are consistent with the finding in Sec. 5.4 that the equatorial overturning circulation weakened in the Commit runs.

The multi-model ensemble composites during El Niño and La Niña for the NDH in the ocean surface-layer are shown in Fig. 5.13. During both El Niño and La Niña, the NDH anomalies are positive along the equatorial Pacific (Fig. 5.13). This feature of the NDH anomalies is known to cause the asymmetry between El Niño and La Niña, as the warm NDH anomalies enhance the warm El Niño events and weaken the cool La Niña events (An and Jin, 2004). There is very substantial strengthening of the positive NDH anomaly in the equatorial belt and an eastward shift by about 25° in the anomaly center (marked by "H") in the Commit runs during El Niño (Figs. 5.13a and c). However, during La Niña, the changes in the NDH anomalies are relatively small between the Commit runs and PIcntrl runs (Figs. 5.13b and d). That the large changes in the magnitude and position of the NDH anomalies between Commit and PIcntrl runs only occurred during El Niño reflects the nonlinear nature of the change in the NDH under enhanced GHG.

The NDH anomalies are mainly caused by the vertical NDH anomalies ($-w\frac{\partial T}{\partial z}$), as can be seen from the similarity between the total NDH anomaly (Figs. 5.13c and d) and the vertical NDH anomaly (Figs. 5.14a and c) during El Niño and La Niña. The substantial change in the vertical NDH anomalies during El Niño in the Commit runs relative to the PIcntrl runs (Figs. 5.14b) is caused by the enhanced vertical temperature gradient anomalies (Figs. 5.14f) and the eastward shift of downwelling anomalies in the central equatorial Pacific (Figs. 5.14i and j). However, during La Niña, the change in the vertical NDH anomalies

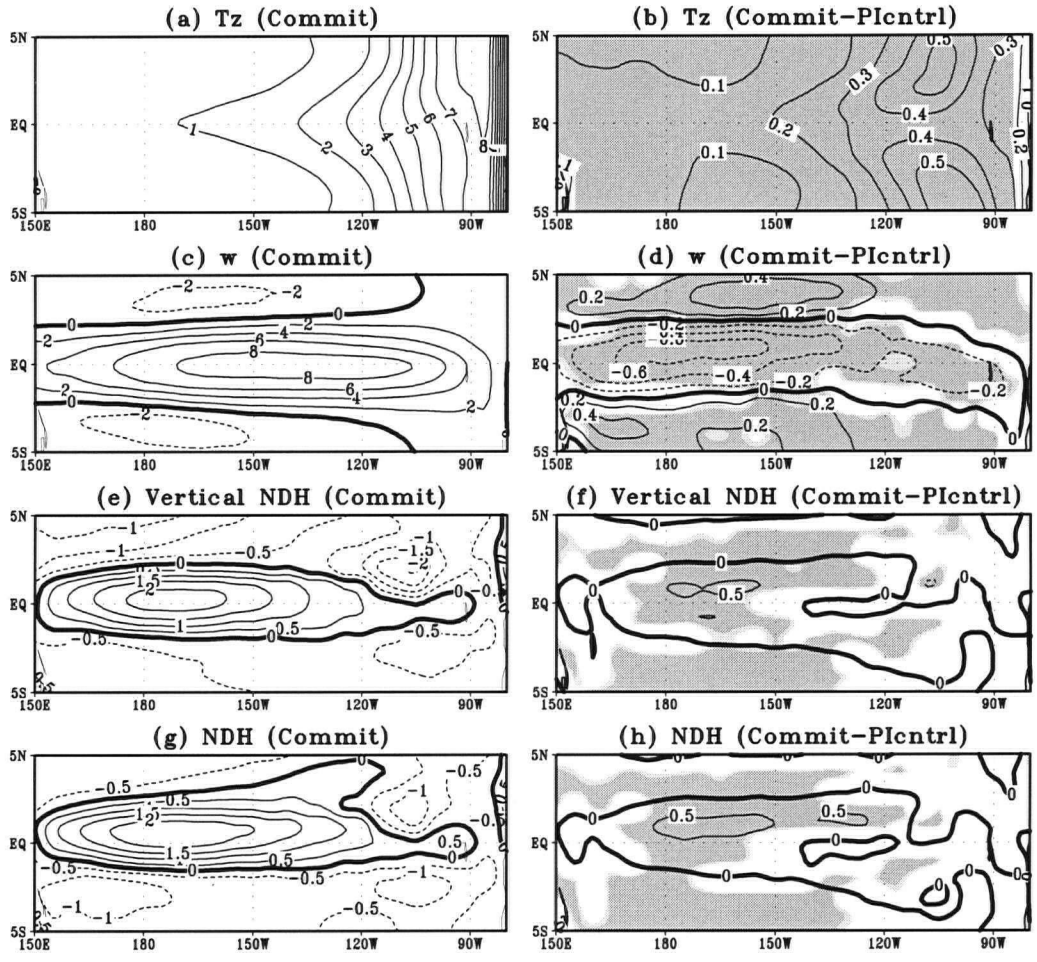

Figure 5.12: Multi-model ensemble mean of vertical temperature gradient (°C/50m, a and b), vertical velocity (10^{-6} m s^{-1}, c and d), vertical nonlinear dynamic heating anomalies (°C $month^{-1}$, e and f) and total nonlinear dynamic heating anomalies (°C $month^{-1}$, g and h) for the Commit runs (left panels) and the change from the PIcntrl runs (right panels), in the ocean surface-layer. The 5% and 10% significance levels from the t-test are shown in gray.

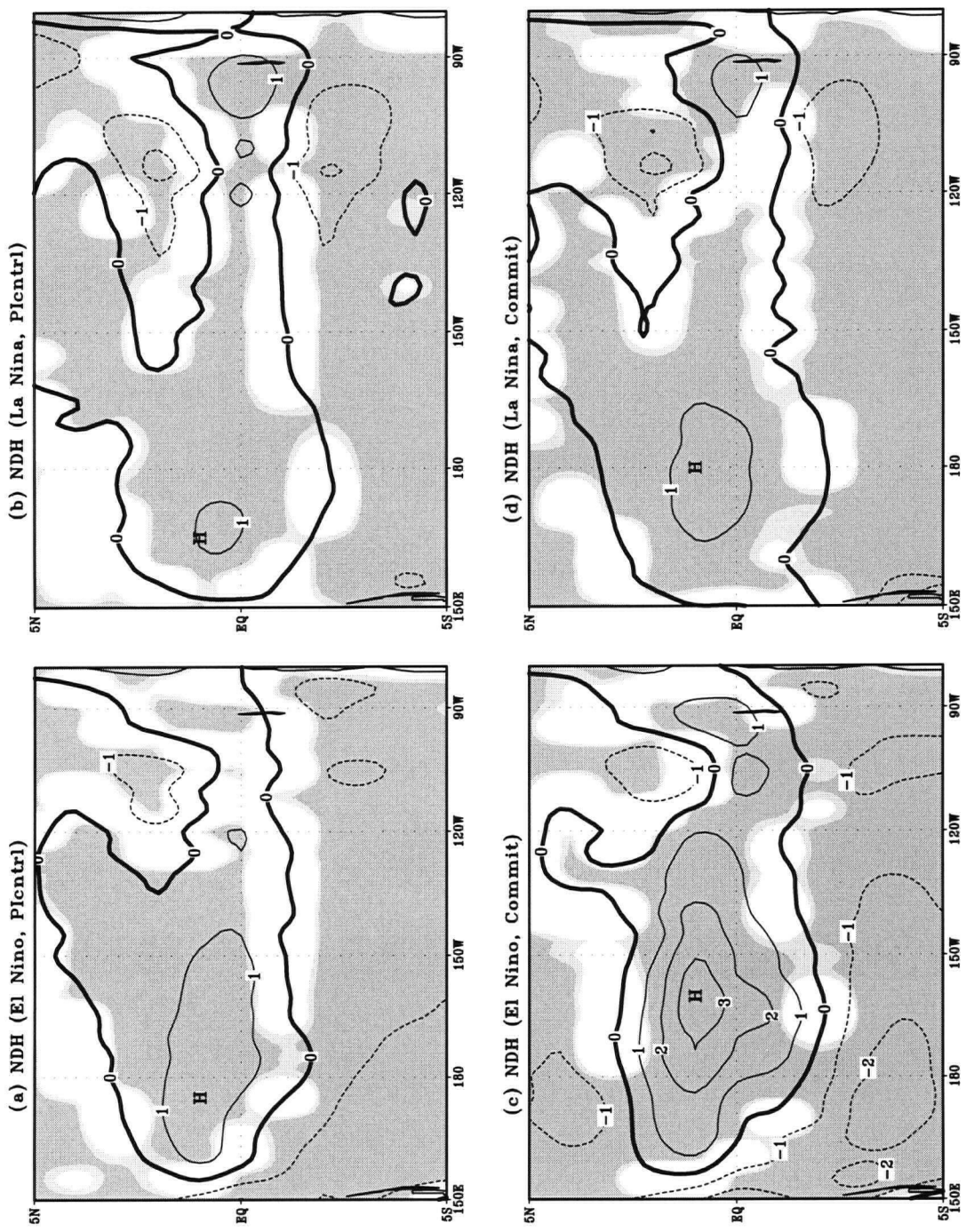

Figure 5.13: Multi-model ensemble mean of surface-layer nonlinear dynamic heating (°C month^{-1}) for the composite El Niño (left panels) and La Niña (right panels), with (a), (b) for the PIcntrl runs, and (c), (d) for the Commit runs. The 5% and 10% significance levels from the t-test are shown in gray.

is relatively minor (5.14c and d). The reason for the east-west dipolar pattern seen in $\frac{\partial T}{\partial z}$ during El Niño in Figs. 5.14e and f is that most of models have a maximum warm SST anomalies in the western or central equatorial Pacific due to model bias.

5.8 Conclusion

The El Niño-like warming in the tropical Pacific seen in the observed SST record (1900-1999) was confirmed by the multi-model results comparing the climate from year 2000 GHG(+aerosol) forcing (Commit) with the pre-industrial climate (PIcntrl). Both the equatorial zonal overturning circulation and the shallow meridional overturning circulation weakened with increased GHG. The idea that the GHGs might play a role on the slowdown of the zonal and shallow meridional overturning circulations received strong support from the multi-model ensemble means. This conclusion also matches the finding that the Walker circulation in the atmosphere has been weakening since the mid-19th century due to the anthropogenic forcing (Vecchi et al, 2006).

In the observed SST data, the positive anomalies during El Niño were located further east in the 1950-1999 composite than in the 1900-1949 composite, whereas the negative anomalies during La Niña were shifted in the opposite direction. From the model data, the positive SST anomalies during El Niño also shifted eastward in the Commit runs relative to the PIcntrl runs, whereas the negative SST anomalies during La Niña were not shifted zonally. Hence both the model and observed SST results were consistent with increasing asymmetry between El Niño and La Niña as GHG increased. The increase in the asymmetry is associated with an increase in the nonlinearity of ENSO (Jin et al, 2003; An and Jin, 2004), with the nonlinear dynamical heating (NDH) terms producing the asymmetry between El Niño and La Niña. A diagnostic analysis of the ocean surface temperature

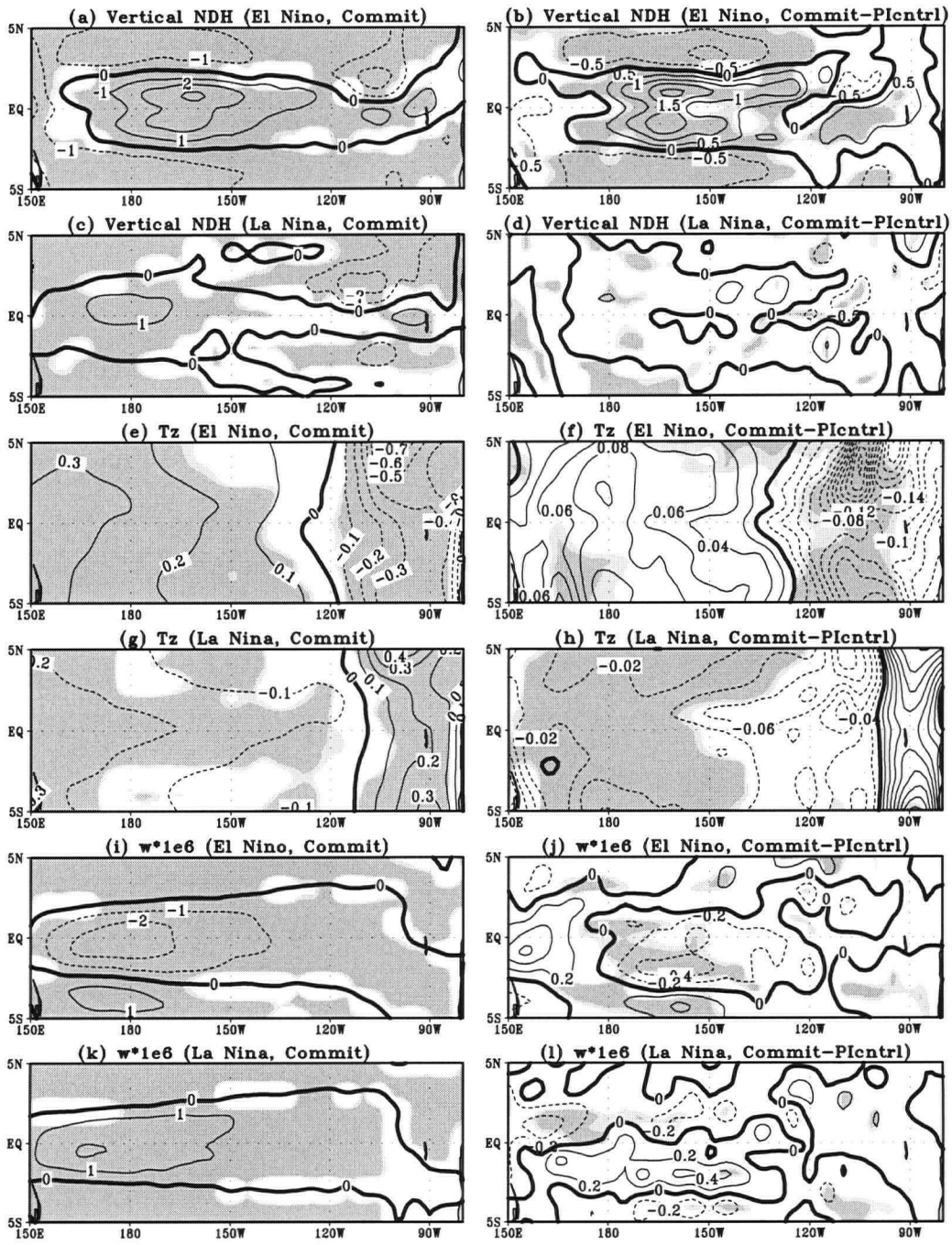

Figure 5.14: Multi-model ensemble mean of the (a-d) surface vertical nonlinear dynamic heating (°C month^{-1}), (e-h) vertical temperature gradient anomalies (°C/50m), and (i-l) vertical velocity anomalies (10^{-6} m s^{-1}) during El Niño and La Niña for the Commit runs (left panels) and the difference between the Commit and PIcntrl runs (right panels). The 5% and 10% significance levels from the t-test are shown in gray.

tendency equation revealed the vertical NDH term to be most dominant, with the positive vertical NDH anomalies in the equatorial Pacific enhanced substantially in the Commit runs during El Niño, caused by the increased vertical temperature gradient anomalies and the eastward shift of downwelling anomalies. Under increased GHG, the enhanced positive NDH anomalies during El Niño when time-averaged over the whole record would change the SST mean state by an El Niño-like pattern, which could override other mechanisms trying to induce a La Niña-like change in the mean state (Cane et al., 1997).

For the simulated equatorial zonal circulation associated with ENSO, the zonal undercurrent anomalies during El Niño strengthened slightly and shifted eastward in the Commit runs relative to the PIcntrl runs, whereas the undercurrent anomalies during La Niña shifted slightly westward. For the simulated shallow meridional overturning circulation in the Pacific, the interior path from the eastern subtropical Pacific to the central equatorial region was clearly seen during both El Niño and La Niña. The enhanced GHG simulations showed that the asymmetry between El Niño and La Niña was enhanced in the anomalies of the SST, the zonal wind stress, the equatorial undercurrent and the shallow meridional overturning circulation.

5.9 References

An S.-I., 2004: Interdecadal changes in the El Niño La-Niña asymmetry. *Geophys. Res. Lett.*, 31, L23210. DOI:10.1029/2004GL021699.

An S.-I., and F.-F. Jin, 2004: Nonlinearity and asymmetry of ENSO. *J. Climate*, 17, 2399-2412.

An S.-I. and B. Wang, 2000: Interdecadal change of the structure of the ENSO mode and

its impact on the ENSO frequency. *J. Climate* 13, 2044-2055.

Anthes R. A., R. W. Corell, G. Holland, J. W. Hurrell, M. C. MacCracken, and K. E. Trenberth, 2006: Hurricanes and Global Warming-Potential Linkages and Consequences. *Bull. Amer. Meteor. Soc.*, 87, 623-628.

Barnett T. P., D. W. Pierce, M. Latif, D. Dommenget and R. Saravanan, 1999: Interdecadal interactions between the tropics and midlatitudes in the Pacific basin. *Geophys. Res. Lett.*, 26, 615-618. DOI:10.1029/1999GL900042.

Cane M. A., A. C. Clement, A. Kaplan, Y. Kushnir, D. Pozdnyakov, R. Seager, S. E. Zebiak and R. Murtugudde, 1997: Twentieth-century sea surface temperature trends. *Science*, 275, 957-960.

Capotondi A., A. T. Wittenberg, and S. Masina, 2006: Spatial and temporal structure of tropical Pacific interannual variability in 20th century coupled simulations. *Ocean Modeling*, in press.

Collins M. and the CMIP Modelling Groups, 2005: El Niño- or La Niña-like climate change?. *Climate Dyn.*, 24, 89-104.

Dai A., 2006: Precipitation characteristics in eighteen coupled climate models. *J. Climate*, 19, 4605-4630.

Fedorov A. V. and S. G. H. Philander, 2001: A stability analysis of tropical ocean-atmosphere interactions: Bridging measurements and theory for El Niño). *J. Climate*, 14, 3086-3101.

Flügel M., P. Chang and C. Penland, 2004: The role of stochastic forcing in modulating ENSO predictability. *J. Climate*, 17, 3125-3140.

Gu D. and S. G. H. Philander, 1997: Interdecadal climate fluctuations that depend on exchanges between the tropics and extratropics. *Science*, 275, 805-807.

Guilyardi E., 2006: El Niño-mean state-seasonal cycle interactions in a multi-model ensemble. *Climate Dyn.*, 26, 329-348. DOI:10.1007/s00382-005-0084-6.

IPCC TAR (Intergovernmental Panel on Climate Change, Third Assessment Report), 2001: *Climate Change 2001: The Scientific Basis*, J. T. Houghton, Y. Ding, D. J. Griggs, M. Noguer, P. J. van der Linden, X. Dai, K. Maskell, and C. A. Johnson (Eds.), *Cambridge Univ. Press.*

Jin F.-F., S.-I. An, A. Timmermann and J. Zhao, 2003: Strong El Niño vents and nonlinear dynamical heating. *Geophys. Res. Lett.* 30, 1120. OI:10.1029/2002GL016356.

Jones P. D., and A. Moberg, 2003: Hemispheric and large-scale surface air temperature variations: an extensive revision and an update to 2001. *J. Climate*, 16, 206-223.

Kleeman R., J. P. McCreary and B. A. Klinger, 1999: A mechanism for generating ENSO decadal variability. *Geophys. Res. Lett.*, 26, 1743-1746.

Knutson T. R. and S. Manabe, 1998: Model assessment of decadal variability and trends in the tropical Pacific Ocean. *J. Climate*, 11, 2273-2296.

Liu Z., 1994: A Simple Model of the Mass Exchange between the Subtropical and Tropical Ocean. *J. Phys. Oceanogr.*, 24, 1153-1165.

McCreary J. P., and P. Lu, 1994: Interaction between the Subtropical and Equatorial Ocean Circulations: The Subtropical Cell. *J. Phys. Oceanogr.*, 24, 466-497.

McPhaden M. J., and D. Zhang, 2002: Slowdown of the meridional verturning circulation in the upper Pacific Ocean. *Nature*, 415, 606-608.

McPhaden M. J. and D. Zhang, 2004: Pacific Ocean circulation rebounds, *Geophys. Res. Lett.*, 31, L18301. DOI:10.1029/2004GL020727.

Meehl G. A., H. Teng, and G. W. Branstator, 2006: Future changes of El Nino in two global coupled climate models. *Climate Dyn.*, DOI:10.1007/s00382-005-0098-0.

Merryfield W. J., and G. J. Boer, 2005: Variability of upper Pacific Ocean overturning in a coupled climate model. *J. Climate*, 18, 666-683.

Merryfield W. J., 2006: Changes to ENSO under CO2 doubling in a multi-model ensemble. *J. Clim.*, 19, 4009-4027.

Nonaka M., S.-P. Xie, and J.P. McCreary, 2002: Decadal variations in the Subtropical Cells and equatorial Pacific SST. *Geophys. Res. Lett.*, 29, 10.1029/2001GL013676.

Rodgers K. B., P. Friederichs and M. Latif, 2004: Tropical Pacific decadal variability and its relation to decadal modulations of ENSO. *J. Climate*, 17, 3761-3774.

Saji N. H., S.-P. Xie, and T. Yamagata, 2006: Tropical Indian Ocean variability in the IPCC twentieth-century climate simulations. *J. Climate*, 19, 4397-4417.

Smith T. M. and R. W. Reynolds, 2004: Improved extended reconstruction of SST, 1854-1997). *J. Climate* 17, 2466-2477.

Solomon A. and D. Zhang, 2006: Pacific Subtropical Cell variability in coupled climate model simulations of the late 19th-20th Century. *Ocean Modelling*, in press.

Thompson C. J. and D. S. Battisti, 2001: A linear stochastic dynamical model of ENSO. Part II: Analysis. *J. Climate* 14, 445-466.

Van Oldenborgh G.J., S.Y. Philip, and M. Collins, 2005: El Nino in a changing climate: a multi-model study. *Ocean Sci.*, 1, 81-95.

Vecchi G. A., B. J. Soden, A. T. Wittenberg, I. M. Held, A. Leetmaa and M. J. Harrison, 2006: Weakening of tropical Pacific atmospheric circulation due to anthropogenic forcing. *Nature*, 44, 73-76.

von Storch H., and F. W. Zwiers, 1999: *Statistical Analysis in Climate Research.* Cambridge Univ. Press, 484 pp.

Wu A. and W. W. Hsieh, 2003: Nonlinear interdecadal changes of the El Niño-Southern Oscillation. *Climate Dyn.*, 21, 719-730. DOI:10.1007/s00382-003-0361-1.

Xie S.-P., T. Miyama, Y. Wang, H. Xu, S.P. de Szoeke, R.J. Small, K.J. Richards, T. Mochizuki and T. Awaji, 2006: A regional ocean-atmosphere model for eastern Pacific climate: Towards reducing tropical biases. *J. Climate*, in press.

Ye Z. and W. W. Hsieh, 2006: The influence of climate regime shift on ENSO. *Climate Dyn.*, 26, 823-833. DOI:10.1007/s00382-005-0105-5.

Zhang D. and M.J. McPhaden, 2006: Decadal variability of the shallow Pacific meridional overturning circulation: relation to tropical sea surface temperatures in observations and climate change models. *Ocean Modelling*, DOI:10.1016/j.ocemod.2005.12.005. in press.

Zhang G. J. and H. Wang, 2006: Toward mitigating the double ITCZ problem in NCAR CCSM3. *Geophys. Res. Lett.*, 33, L06709, DOI:10.1029/2005GL025229.

Chapter 6

Summary and Conclusions

6.1 Summary and Conclusions

This thesis began with a study on the influence of climate regime shift on ENSO. Eastward shifts in the location of the zonal wind stress anomalies were found in the observational data during strong El Niño episodes after the mid 1970s climate regime shift. Similar shifts appeared in the surface shortwave and latent heat fluxes in the observations. The simulated results from a modified Zebiak-Cane coupled model reproduced such shifts when a 1981-1995 climatology was used instead of a 1961-1975 climatology in the numerical model. Further sensitive experiments illustrated that the change in the atmospheric climatology, which caused the eastwards shifts in the westerly anomalies and convergence heating rate anomalies, is the major cause, with the change in the upper ocean climatology being of minor importance. The analysis of the model convergence heating rate Q_c (which depends on the mean surface wind convergence and links to the latent heating rate) indeed showed that the strong shift found in Q_c was the probable cause for the changes in ENSO. These results are consistent with the observed heat flux.

While the change in the surface background wind resulted in the eastward shifts in the surface wind anomalies and convergence heating rate anomalies during strong El Niño, during strong La Niña the eastward shifts were not evident in the 1981-1995 regime. Thus

the asymmetry between the El Niño state and the La Niña state has been enhanced in the 1981-1995 regime, which also implies enhanced nonlinearity in the ENSO system. Also consistent with observations are the enhanced predictability and lengthened ENSO period found when the model was run with the 1981-1995 climatology. All these agreements with observations suggest that despite the uncertainties in using climatologies calculated from relatively short records, using the 1981-1995 climatology in the coupled model did induce changes in ENSO properties consistent with the observed changes.

The predictability analysis of the 2100-yr simulated SST and wind stress (WS) in the intermediate coupled model reveals that changes in ENSO properties under climate regime shifts are closely linked to changes in ENSO nonlinearity. The change in ENSO predictability occurs with the change in ENSO nonlinearity as well as with the change in ENSO period. Stronger nonlinearity is associated with longer period and better predictability. In the Lorenz 3-component chaos system, by adjusting the model parameters to change the nonlinearity of the system, a similar behavior was found. Thus in both the ENSO and Lorenz systems, stronger nonlinearity corresponds to longer period and enhanced predictability.

The role of the surface zonal current was clearly distinct in the NLPCA modes associated with the two regimes: for the pre-1980s, the surface zonal current tended to be an intensifier of ENSO, while that for the post-1980s played a role in ENSO transition.

An analysis of historical SST provided evidence for the El Niño-like warming trend in the tropical Pacific during 1900-1999. This El Niño-like warming trend was confirmed by the IPCC AR4 multi-model data by comparing the climate from year 2000 GHG(+aerosol) forcing (Commit) with the pre-industrial climate (PIcntrl). Analysis showed that both the equatorial zonal overturning circulation and the shallow meridional overturning circulation tended to slow down with increased GHG, as expected since the Walker circulation in the

atmosphere has been weakening since the mid-19th century due to anthropogenic forcing (Vecchi et al, 2006). It is also consistent with the conclusion that the shallow meridional overturning circulation had a slowdown trend during 1953-2000 (McPhaden and Zhang, 2002; Zhang and McPhaden, 2006)

The historical SST records showed that the positive SST anomalies during El Niño appeared further east in the 1950-1999 composite than in the 1900-1949 composite, whereas the negative SST anomalies during La Niña were shifted in the opposite direction. From the ensemble mean of the IPCC AR4 multi-model data, the positive SST anomalies during El Niño also shifted eastward in the Commit runs relative to the PIcntrl runs, whereas the negative SST anomalies during La Niña were not shifted zonally. Hence both the model and observed SST results were consistent with increasing asymmetry between El Niño and La Niña as GHG increased. The increase in the asymmetry is associated with an increase in the nonlinearity of ENSO (Jin et al, 2003; An and Jin, 2004), with the nonlinear dynamical heating (NDH) terms producing the asymmetry between El Niño and La Niña. A diagnostic analysis of the ocean surface temperature tendency equation revealed the vertical NDH term to be most dominant, with the positive vertical NDH anomalies in the equatorial Pacific enhanced substantially in the Commit runs during El Niño, caused by the enhanced vertical temperature gradient anomalies and the eastward shift of downwelling anomalies. The enhanced GHG simulations showed that the asymmetry between El Niño and La Niña was enhanced in the anomalies of the SST, the zonal wind stress, the equatorial undercurrent and the shallow meridional overturning circulation.

There is much scope for further research: Consideration of double or even quadruple CO_2 forcing in IPCC scenario experiments would further illustrate the potential for future climate change. The nonlinear nature of the coupled ocean-atmosphere system means that

changes of this magnitude on the ENSO system would be much larger than the Commit runs.

We have only speculated on the mechanism responsible for the shift in the surface net shortwave radiation flux and in the latent heat flux. Lack of data is the primary reason for our poor understanding of the mechanism during decadal climate variability. Greater availability of long satellite datasets plus other measurements would allow us to study more detailed decadal variability of surface net shortwave radiation flux, longwave radiation flux, latent heat flux, and sensible heat flux over the tropical Pacific, and to understand the underlying mechanism.

The main interest of this thesis focuses on the tropical Pacific; further work could extend to the Indian Ocean and the Atlantic Ocean.

6.2 References

An S.-I., and F.-F. Jin, 2004: Nonlinearity and asymmetry of ENSO. *J. Climate*, 17, 2399-2412.

Jin F.-F., S.-I. An, A. Timmermann and J. Zhao, 2003: Strong El Niño vents and nonlinear dynamical heating. *Geophys. Res. Lett.* 30, 1120. OI:10.1029/2002GL016356.

McPhaden M. J., and D. Zhang, 2002: Slowdown of the meridional verturning circulation in the upper Pacific Ocean. *Nature*, 415, 606-608.

Vecchi G. A., B. J. Soden, A. T. Wittenberg, I. M. Held, A. Leetmaa and M. J. Harrison, 2006: Weakening of tropical Pacific atmospheric circulation due to anthropogenic forcing. *Nature*, 44, 73-76.

Zhang D. and M.J. McPhaden, 2006: Decadal variability of the shallow Pacific meridional overturning circulation: relation to tropical sea surface temperatures in observations and climate change models. *Ocean Modelling*, `DOI:10.1016/j.ocemod.2005.12.005`. in press.

Appendix A

The Zebiak-Cane coupled model

A.1 Coupled Model Equations

Atmosphere

The dynamics follow Gill (1980), i.e., steady-state, linear shallow-water equations on an equatorial beta plane. Linear dissipation in the form of Rayleigh friction and Newtonian cooling is used. The circulation is forced by a heating anomaly that depends partly on local heating associated with SST anomalies and partly on the low-level moisture convergence (parameterized in terms of the surface wind convergence). The convergence feedback is incorporated into the model using an iterative procedure in which the heating at each iteration depends on the convergence field from the previous iteration. The feedback is nonlinear because the moisture-related heating is operative only when the total wind field is convergent, and this depends not only on the calculated convergence anomaly, but also on the specified mean convergence. On an equatorial β-plane the equations for the atmosphere (at iteration n) are as follows (Zebiak and Cane, 1987):

$$\epsilon u_a^n - \beta_o y v_a^n = -\frac{1}{\rho_o}\frac{\partial p^n}{\partial x}, \tag{A.1}$$

$$\epsilon v_a^n + \beta_o y u_a^n = -\frac{1}{\rho_o}\frac{\partial p^n}{\partial y}, \tag{A.2}$$

$$\frac{\epsilon}{\rho_o} p^n + c_a^2\left[\frac{\partial u_a^n}{\partial x} + \frac{\partial v_a^n}{\partial y}\right] = -Q_s - Q_1^{n-1}, \tag{A.3}$$

where

$$Q_s = (\alpha T)\ \exp[(\overline{T} - 30^oC)/16.7^oC], \tag{A.4}$$

$$Q_1^n = \beta[M(\overline{c} + c^n) - M(\overline{c})], \tag{A.5}$$

$$c^n = -\frac{\partial u_a^n}{\partial x} - \frac{\partial v_a^n}{\partial y},$$

$$M(x) = \begin{cases} 0, & x \leq 0 \\ x, & x > 0. \end{cases}$$

u_a and v_a are the zonal and meridional component of surface wind anomaly, respectively, p is the surface pressure anomaly, ρ_o is the air reference density, $c_a = 60$ ms^{-1}, and $\epsilon =$ (2 days)$^{-1}$ is the damping coefficient (taken to be the same for momentum and thermal damping). $\overline{T}(x, y, t)$ is the prescribed monthly mean sea surface temperature (SST), and T the SST anomalies. $\overline{c}(x, y, t)$ is the prescribed monthly mean surface wind convergence, and c^n the anomalous convergence at iteration n. (x, y) is the horizontal spatial position and t is time. β_o is latitudinal derivative of the Coriolis parameter, α and β are both empirical coefficients, $\alpha = 0.031$ m^{2}s^{-3} ^{o}C^{-1}, $\beta = 1.6 \times 10^4$ m^{2}s^{-2}.

Ocean

The model ocean basin is rectangular and extends from 120^{o}E to 80^{o}W and from 29^{o}N to 29^{o}S. The dynamics of the model begin with the linear reduced-gravity equations. Since seasonal responses and large-scale features of the wind field are of interest, the low-frequency, long zonal-scale approximation is made:

$$\partial/\partial t = \partial/\partial x = O(\epsilon_o), \qquad \epsilon_o << 1.$$

Scaling analysis reveals that $v = O(\epsilon_o)$, $h = u = O(u)$ and the governing equations for the ocean are

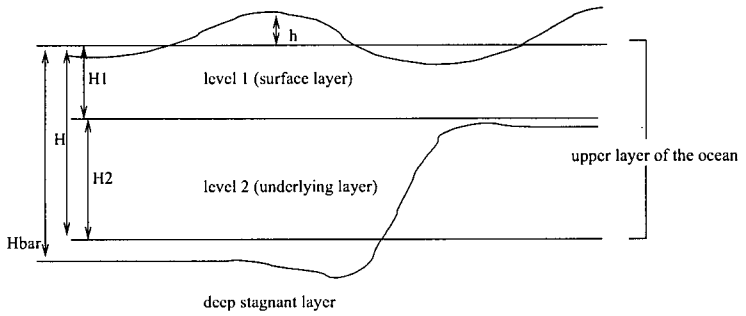

Figure A.1: Ocean model levels

$$\frac{\partial u}{\partial t} - \beta_o y v = -g' \frac{\partial h}{\partial x} + \frac{\tau^{(x)}}{\rho H} - ru, \tag{A.6}$$

$$\beta_o y u = -g' \frac{\partial h}{\partial y} + \frac{\tau^{(y)}}{\rho H} - rv, \tag{A.7}$$

$$\frac{\partial h}{\partial t} + H[\frac{\partial u}{\partial x} + \frac{\partial v}{\partial y}] = -rh, \tag{A.8}$$

where

$$\mathbf{u} = H^{-1}[H_1 \mathbf{u}_1 + H_2 \mathbf{u}_2],$$

with the subscripts 1 and 2 refer to the surface layer and underlying layer, respectively. $g' = g\Delta\rho/\rho$, $\Delta\rho$ is the density difference between the two layers, ρ is the mean density in the upper layer, and $\Delta\rho/\rho = 0.0057$ (i.e., an equivalent depth $H_e = 86$ cm). H_1 is the surface layer depth, H is the averaged upper layer thickness, and h is the sea level heigh (see Fig. A.1). u and v are the zonal and meridional components of the velocity vector $\mathbf{u}$, respectively. $\tau^{(x)}$ and $\tau^{(y)}$ are the zonal and meridional components of the surface wind stress anomalies, respectively. Rayleigh friction damping with decay time r^{-1} has been included.

The equations governing the shear between layers 1 and 2 are

$$
\begin{aligned}
r_s u_s - \beta_o y v_s &= \frac{\tau^{(x)}}{\rho H_1}, \\
r_s v_s + \beta_o y u_s &= \frac{\tau^{(y)}}{\rho H_1},
\end{aligned}
$$

where the horizontal currents shear is defined by

$$
\mathbf{u_s} = (u_s, v_s) \equiv \mathbf{u}_1 - \mathbf{u}_2.
$$

The temperature equation for the surface layer is

$$
\frac{\partial T}{\partial t} = -\mathbf{u}_1 \cdot \nabla(\overline{T}+T) - \overline{\mathbf{u}}_1 \cdot \nabla T - \{M(\overline{w}_s + w_s) - M(\overline{w}_s)\} \times \frac{\partial \overline{T}}{\partial z} - M(\overline{w}_s + w_s)\frac{T - T_e}{H_1} - \alpha_s T,
$$

where the entrainment velocity is calculated by

$$
w_s = H_1 \left[\frac{\partial u_1}{\partial x} + \frac{\partial v_1}{\partial y} \right].
$$

$\overline{\mathbf{u}}_1(x, y, t)$ and $\overline{w}_s(x, y, t)$ are, respectively, the mean horizontal currents and upwelling velocity in the surface layer. $\overline{T}(x, y, t)$ is the prescribed mean SST, $\frac{\partial \overline{T}(x)}{\partial z}$ is the prescribed mean vertical temperature gradient, and α_s =(125 days)$^{-1}$ is the diffusion coefficient. The entrainment temperature anomaly, T_e, is defined by

$$
T_e = \gamma T_{sub} + (1 - \gamma)T,
$$

where, in the original Zebiak and Cane (1987) model, T_{sub} has the form given by (2.5).

In this thesis, the relation between T_{sub} and h is replaced by a neural network model. First Zebiak and Cane ocean model was forced by the observed Florida State University (FSU) WS (Bourassa et al, 2001) from 1964 to 1998, and the model thermocline depth anomalies h and current anomalies were extracted. T_{sub} was inversely calculated from the temperature equation (2.1) using the observed SST (Smith and Reynolds, 2004) for T and

the model anomalous currents. PCA was separately applied to the simulated upper layer depth anomalies $h(x, y, t)$, and to $T_{\text{sub}}(x, y, t)$ to extract the leading PCs.

$$h(x, y, t) = \sum_n a_n(t)\, f_n(x, y)\,,$$

$$T_{\text{sub}}(x, y, t) = \sum_n c_n(t)\, e_n(x, y)\,,$$

where n indicates the nth mode. For the thermocline depth anomaly h, the first three PCA modes accounted for 63% (32%, 22%, 9% for the three leading PCA modes, respectively) of the variance, while for the T_{sub}, the first three modes accounted for 64% (36%, 15%, 13% for the three leading PCA modes, respectively) of the variance. The NN used has three input neurons, namely the first three principal components (PCs) $a_n(t)$ for h, and the single output neuron is one of the three leading PCs $c_n(t)$ for T_{sub}, i.e., a different NN model was used to predict each predictand c_n, using three a_n as predictors, with no time lag between the predictors and the predictand. Data from 1964 to 1998 was used to train the NN models, The optimal NN T_{sub} models were obtained by randomly dividing the data into training and test data in 30 times. Then the NN models were used to replace equation (2.5) in the coupled model.

Coupling

The ocean component is forced by surface wind stress anomalies. A standard bulk formula is used to generate stress anomalies from the combination of surface wind anomalies produced by the atmosphere model and the background mean winds. The ocean dynamics time step is 10 days.

The atmosphere model is steady-state and in the coupled model, the wind field is determined at 10-day increments. Time dependence is allowed only in the moisture convergence component of the heating. The change in moisture convergence heating is computed at each

time step, and the assumed background convergence is the total convergence at the previous time step, rather than just the mean convergence (i.e., at time step m, $\bar{c}_m = \bar{c}_{m-1} + c_{m-1}$ in the equation (A.5)). Because of the nonlinearity of the heating parameterization, this time-marching procedure allows the development of small-scale anomalies that can persist and become unrelated to subsequent SST anomaly pattern. To eliminate them, the heating is recalculated periodically using the steady model formulation, based on the current SST anomaly field. (This strategy is similar to the periodical restarts often used with the leapfrog scheme to suppress splitting of the solution.) To summarize, the calculation of the atmospheric heating is split into two parts. The portion related directly to SST gives a wind response in equilibrium with the SST field on a time scale of 10 days. The portion of the heating related to internal moisture convergence feedback operates in a time-stepping sense, and so forces a wind field adjustment on a somewhat shorter time scale.

Parameter values used for the coupled simulation are as follows: r =(2.5 years)$^{-1}$, $c = (g'H)^{1/2} = 2.9$ ms^{-1}, H =150 m, H_1 =50 m, r_s =(2 days)$^{-1}$.

The standard grid for ocean dynamics is 2^o longitude by 0.5^o latitude; the standard grid for SST physics and atmosphere model is 5.625^o longitude by 2^o latitude. The intermediate coupled model domain covers the tropical Pacific from 29°S to 29°N, and from 124°E to 80°W.

A.2 Computational Procedures

Atmosphere

The equations (A.1) to (A.3) are solved by using spectral decomposition in x, and finite differencing in y. Writing

$$(u_a, v_a, p, Q_s, Q_1) = (U_a, V_a, P, \widetilde{Q_s}, \widetilde{Q_1}) \exp(ikx)$$

and substituting into the equations (A.1) to (A.3) gives

$$\epsilon U_a^n - \beta_o y V_a^n = -\frac{ik}{\rho_o} P^n, \tag{A.9}$$

$$\epsilon V_a^n + \beta_o y U_a^n = -\frac{1}{\rho_o}\frac{\partial P^n}{\partial y}, \tag{A.10}$$

$$\frac{\epsilon}{\rho_o} P^n + c_a^2[ikU_a^n + \frac{\partial V_a^n}{\partial y}] = -\widetilde{Q_s} - \widetilde{Q}_1^{n-1}. \tag{A.11}$$

For variable Ψ (e.g., U_a^n, V_a^n, P^n, $\widetilde{Q}_s$ or $\widetilde{Q}_1^n$), we use spatial differencing in the y direction

$$\frac{\partial \Psi}{\partial y} = \frac{\Psi_{j+1} - \Psi_{j-1}}{2\Delta y},$$

$$\frac{\partial^2 \Psi}{\partial y^2} = \frac{\Psi_{j+1} + \Psi_{j-1} - 2\Psi_j}{(\Delta y)^2},$$

where j is the grid index in the y direction, and $\Delta y = 2^{\mathrm{O}}$ latitude. The boundary conditions for the equations are that $V_a = 0$ at the poles. In practice the solution decays rapidly outside the forcing region (which is tropical) so the solution is insensitive to the exact location of the zonal walls (There are two walls at 80^{O}S and 80^{O}N in the atmosphere model). The domain is from 80^{O}S to 80^{O}N in y direction. The spectral decomposition is done using a 64-point fast Fourier transform (FFT), and the domain is the full 360° longitude, giving resolution (in x) of 5.625°.

Ocean

The numerical procedure for solving equations (A.6) to (A.8) is given in detail in Cane and Patton (1984). The solution is obtained by treating the Kelvin wave portion of the solution analytically and calculating the remainder of the solution by finite difference methods on a staggered grid, taking advantage of the fact that this part of the solution has no eastward propagation. The procedure allows large time steps and is limited only by

accuracy considerations. The scheme introduces no spurious sources or sinks of mass or energy.

The nondimensionalized equations can be obtained from equations (A.6) to (A.8):

$$\frac{\partial u}{\partial t} - yv + \frac{\partial h}{\partial x} = F - ru, \tag{A.12}$$

$$yu + \frac{\partial h}{\partial y} = G - rv, \tag{A.13}$$

$$\frac{\partial h}{\partial t} + \frac{\partial u}{\partial x} + \frac{\partial v}{\partial y} = Q - rh. \tag{A.14}$$

The equations have been nondimensionalized in the usual equatorial way: the time scale is $(c\beta_o)^{-1/2}$ and length scale is $(c/\beta_o)^{1/2}$, where $c = (g'H)^{1/2} = 2.9$ ms^{-1} is a scale for wave speeds. The external forcings F, G and Q are due to the zonal wind stress, meridional wind stress and buoyancy flux, respectively. Rayleigh friction damping with decay time r^{-1} has been included; note that, with the definition

$$(u^*, v^*, h^*, F^*, G^*, Q^*) = \exp(-rt)(u, v, h, F, G, Q),$$

the equations for the starred variables are formally the same as (A.12) to (A.14) with $r = 0$. The numerical model treats friction in this way: assume $r = 0$ for the Kelvin wave analytical solution of the equations (A.12) to (A.14). The solution to the equations (A.12) to (A.14) may be written as

$$(u, v, h) = a_k(x, t)[\Psi_{-1}(y), 0, \Psi_{-1}(y)] + [u'(x, y, t), v'(x, y, t), h'(x, y, t)]$$

where the prime quantities are long Rossby and anti-Kelvin modes, and the first term is the Kelvin wave,

$$\Psi_{-1}(y) = C^{-1} \exp(-y^2/2)$$

with

$$C^2 = \int_{y_S}^{y_N} \exp(-y^2) dy,$$

where y_S and y_N are the southern boundary and northern boundary, respectively. Then the primed part of the solution, consisting of long Rossby and anti-Kelvin modes, propagates only to the west. The equation governing a_k is found by projecting the Kelvin mode on to the equations (A.12) to (A.14):

$$\frac{\partial a_k}{\partial t} + \frac{\partial a_k}{\partial x} = f_K(x,t),$$

where

$$\begin{aligned} f_K &= \frac{(F,G,Q)\cdot(\Psi_{-1},0,\Psi_{-1})}{(\Psi_{-1},0,\Psi_{-1})\cdot(\Psi_{-1},0,\Psi_{-1})} \\ &= \frac{1}{2}\int_{y_S}^{y_N}(F+Q)\Psi_{-1}dy. \end{aligned} \tag{A.15}$$

The differential equations governing the remainder of the solution are found by subtracting the Kelvin wave from the equations (A.12) to (A.14) (with $r = 0$)

$$\frac{\partial u'}{\partial t} - yv' + \frac{\partial h'}{\partial x} = F' = F - f_K\Psi_{-1}, \tag{A.16}$$

$$yu' + \frac{\partial h'}{\partial y} = G, \tag{A.17}$$

$$\frac{\partial h'}{\partial t} + \frac{\partial u'}{\partial x} + \frac{\partial v'}{\partial y} = Q' = Q - f_K\Psi_{-1}. \tag{A.18}$$

The finite-difference version is defined on a staggered grid. With n, i, j indexing time, longitude and latitude, respectively, the equations of motion take the form

$$\begin{aligned} \frac{1}{2\Delta t}(u^n_{i,j} + u^n_{i+1,j} - u^{n-1}_{i,j} - u^{n-1}_{i+1,j}) - \frac{1}{2}y_j(v^{n-1/2}_{i+1/2,j+1/2} + v^{n-1/2}_{i+1/2,j-1/2}) \\ + \frac{1}{2\Delta x}(h^{n-1}_{i+1,j} + h^n_{i+1,j} - h^{n-1}_{i,j} - h^n_{i,j}) = F^{n-1/2}_{i+1/2,j}, \\ \frac{1}{2}(y_j u^n_{i,j} + y_{j+1}u^n_{i,j+1}) + \frac{1}{\Delta y}(h^n_{i,j+1} - h^n_{i,j}) = G^n_{i,j+1/2}, \\ \frac{1}{2\Delta t}(h^n_{i,j} + h^n_{i+1,j} - h^{n-1}_{i,j} - h^{n-1}_{i+1,j}) + \frac{1}{2\Delta x}(u^{n-1}_{i+1,j} + u^n_{i+1,j} - u^{n-1}_{i,j} - u^n_{i,j}) \\ + \frac{1}{\Delta y}(v^{n-1/2}_{i+1/2,j+1/2} - v^{n-1/2}_{i+1/2,j-1/2}) = Q^{n-1/2}_{i+1/2,j}. \end{aligned}$$

The difference scheme is second order accurate in time and space. In the absence of forcing and damping, the finite-difference equations identically conserve mass and energy.

The boundary conditions for the ocean are those of no flow perpendicular to the basin boundaries. Although the model is designed to allow irregular geometry, a rectangular basin is chosen here, with boundaries at 29.75°N, 29.75°S, 124°E, 80°W.

The temperature anomaly equation is evaluated on a spatially uniform grid using forward time differencing. Since the temperature does not influence the dynamical calculation, the accuracy or stability of that calculation is not affected by the temperature prediction scheme. Horizontal advection terms are evaluated using the modified upwind difference scheme. This has the form:

$$(u\frac{\partial T}{\partial x})_{i,j} = \begin{cases} (u_{i,j-1} + u_{i,j})(T_{i,j} - T_{i,j-1})/2\Delta x, & u_{i,j} \geq 0 \\ (u_{i,j} + u_{i,j+1})(T_{i,j+1} - T_{i,j})/2\Delta x, & u_{i,j} < 0 \end{cases} \tag{A.19}$$

$$(v\frac{\partial T}{\partial y})_{i,j} = \begin{cases} (v_{i+1,j} + v_{i,j})(T_{i+1,j} - T_{i,j})/2\Delta y, & v_{i,j} \geq 0 \\ (v_{i-1,j} + v_{i,j})(T_{i,j} - T_{i-1,j})/2\Delta y, & v_{i,j} < 0 \end{cases} \tag{A.20}$$

where i and j are the grid indices in the y and x directions, respectively. The diffusive character of this scheme can be shown with a simple temperature equation:

$$\frac{\partial T}{\partial t} = -\overline{\mathbf{u}}_1 \cdot \nabla T - \alpha_s T.$$

The initial condition has Gaussian SST anomalies ($T(x,y) = 5.0\exp(-(x-x_0)^2-(y-y_0)^2)$) with $\overline{\mathbf{u}}_1 = 10$ cm/s in the zonal direction. Fig. A.2 shows that the diffusion due to the advection term scheme (A.19) is much weaker than that due to the diffusive term $-\alpha_s T$. The difference scheme is second-order accurate, and is transportable and conservative — it advects only in the direction of the flow, and does not produce artificial sources. These features of the scheme are important because in part of the domain (that is, away from

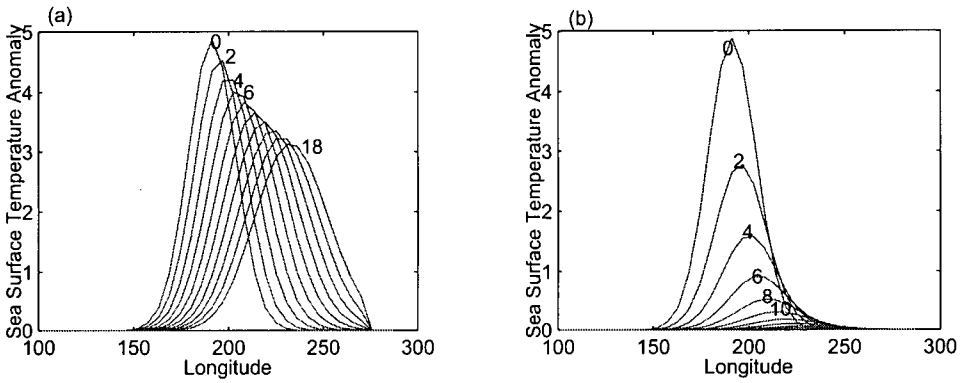

Figure A.2: The SST anomalies at the equator at different model times (0, 2, 4, ..., 18 months) with (a) α_s =0 day^{-1}; (b) α_s =(125 days)$^{-1}$.

the upwelling zones) there are no local advective processes, and therefore are sensitive to deficiencies in the numerical scheme. Equation (A.19) and (A.20) are numerically stable only if $\Delta t \leq$MIN$(\Delta x/u_{max}, \Delta y/v_{max})$ where u_{max} and v_{max} are the largest zonal and meridional velocity components. This sets an upper bound on Δt which diminishes with increasing velocities. The temperature and current field are evaluated on a grid with $\Delta y = 2^{\circ}$ latitude and $\Delta x = 5.625^{\circ}$ longitude. This seemingly peculiar choice anticipates the coupled model calculations, in which the atmosphere model uses such a grid, Within the domain of the ocean, then, there are 27 grid points in x and 30 points in y, though the calculation is done only between 19°N and 19°S (20 points). Since the grid for the dynamical variables (u, v, h) is finer, domain average of these variables are used in evaluating the terms in the temperature equation. A domain is made up of 15 points on the finer grid, making the domains adjacent and nearly non-overlapping.

With the above choice for Δx and Δy, it is necessary to reduce Δt from the value 10 days used by the dynamical model. A value of 2.5 days was used, which guarantees stability for zonal currents less than 2.8 m/s and meridional currents less than 1 m/s. Thus

the temperature equation is iterated 4 times for each time step in the dynamical model, with the variables (u, v, h) held fixed.

A.3 References

Bourassa M. A., S. R. Smith and J. J. O'Brien, 2001: A new FSU winds and flux climatology. 11th Conference on Interations of the Sea and Atmosphere. San Diego, CA, *Amer. Meteor. Soc.*, 912.

Cane M. A. and R.J. Patton, 1984: A numerical model for low-frequency equatorial dynamics. *J. Phys. Oceanogr.*, 14, 1853-1863.

Gill A. E., 1982: *Atmosphere-Ocean Dynamics.* Academic Press, 662pp.

Smith T. M. and R. W. Reynolds, 2004: Improved extended reconstruction of SST, 1854-1997). *J. Climate* 17, 2466-2477.

Zebiak S. E. and M. A. Cane, 1987: A model El Niño-Southern Oscillation. *Mon. Wea. Rev.*, 115, 2262-2278.

Zebiak S. E., 1984: Tropical atmosphere-ocean interaction and the El Niño/Southern Oscillation phenomenon. Ph.D. thesis, M.I.T., 261pp.

Appendix B

Nonlinear principal component analysis (NLPCA)

B.1 Open curves

As PCA finds a straight line which passes through the 'middle' of the data cluster, the obvious next step is to generalize the straight line to a curve (Hsieh, 2004). Kramer (1991) proposed a neural-network (NN) based nonlinear PCA (NLPCA) model where the straight line is replaced by a continuous open curve for approximating the data.

The fundamental difference between NLPCA and PCA is that PCA only allows a linear mapping $u(t) = \mathbf{a} \cdot \mathbf{x}(t)$ between $\mathbf{x}$ and the PC u, while NLPCA allows a nonlinear mapping. To perform NLPCA, the feed-forward NN (Bishop, 1995) in Fig. B.1a contains 3 hidden layers of neurons between the input and output layers of variables.

The NLPCA is basically a standard feed-forward NN with 4-layers of transfer functions mapping from the inputs to the outputs. One can view the NLPCA network as composed of two standard 2-layer feed-forward NNs placed one after the other. The first 2-layer network maps from the inputs $\mathbf{x}$ through a hidden layer to the bottleneck layer with only one neuron u, i.e. a nonlinear mapping $u = f(\mathbf{x})$. The next 2-layer feedforward NN inversely maps from the nonlinear PC (NLPC) u back to the original higher dimensional $\mathbf{x}$-space, with

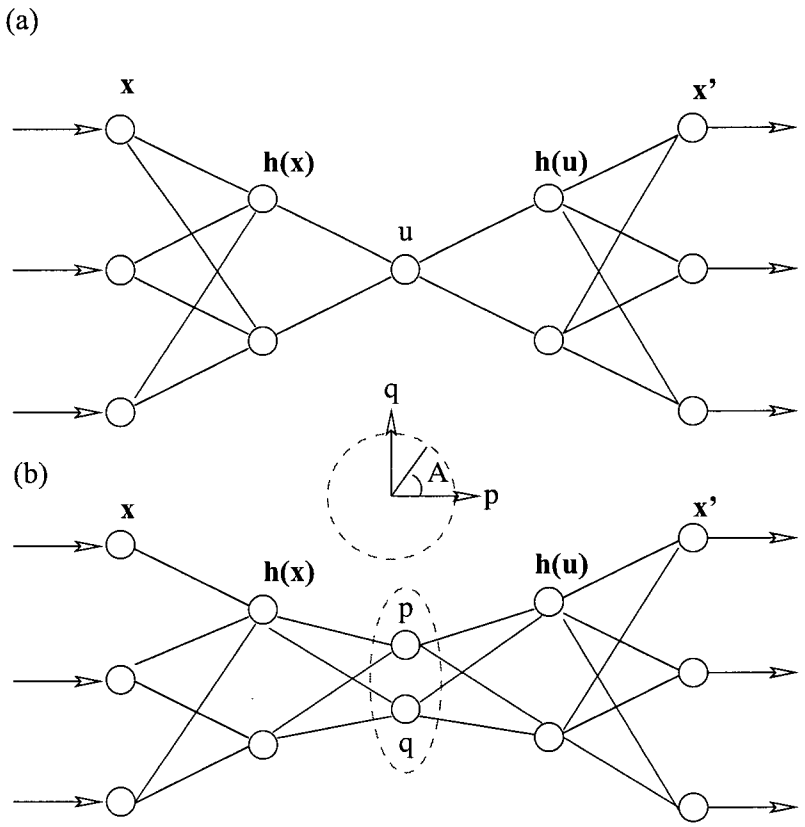

Figure B.1: (a) A schematic diagram of the NN model for calculating the NLPCA. There are 3 layers of hidden neurons sandwiched between the input layer $\mathbf{x}$ on the left and the output layer $\mathbf{x}'$ on the right. Next to the input layer is the encoding layer, followed by the 'bottleneck' layer (with a single neuron u), which is then followed by the decoding layer. A nonlinear function maps from the higher dimension input space to the 1-dimension bottleneck space, followed by an inverse transform mapping from the bottleneck space back to the original space represented by the outputs, which are to be as close to the inputs as possible by minimizing the cost function $J = \langle \|\mathbf{x} - \mathbf{x}'\|^2 \rangle$. Data compression is achieved by the bottleneck, with the bottleneck neuron giving u, the nonlinear principal component (NLPC). (b) A schematic diagram of the NN model for calculating the NLPCA with a circular node at the bottleneck (NLPCA(cir)). Instead of having one bottleneck neuron u, there are now two neurons p and q constrained to lie on a unit circle in the p-q plane, so there is only one free angular variable A, the NLPC. This network is suited for extracting a closed curve solution.

the objective that the outputs $\mathbf{x}' = \mathbf{g}(u)$ be as close as possible to the inputs $\mathbf{x}$, (thus the NN is said to be auto-associative). Note $\mathbf{g}(u)$ nonlinearly generates a curve in the $\mathbf{x}$-space, hence a 1-dimensional approximation of the original data. To minimize the MSE (mean square error) of this approximation, the cost function $J = \langle \|\mathbf{x} - \mathbf{x}'\|^2 \rangle$ is minimized to solve for the weight and bias parameters of the NN. Squeezing the input information through a bottleneck layer with only one neuron accomplishes the dimensional reduction.

In Fig. B.1a, the transfer function f_1 maps from $\mathbf{x}$, the input column vector of length l, to the first hidden layer (the encoding layer), represented by $\mathbf{h}^{(x)}$, a column vector of length m, with elements

$$h_k^{(x)} = f_1((\mathbf{W}^{(x)}\mathbf{x} + \mathbf{b}^{(x)})_k)\,, \tag{B.1}$$

where (with the capital bold font reserved for matrices and the small bold font for vectors), $\mathbf{W}^{(x)}$ is an $m \times l$ weight matrix, $\mathbf{b}^{(x)}$, a column vector of length m containing the bias parameters, and $k = 1, \ldots, m$. Similarly, a second transfer function f_2 maps from the encoding layer to the bottleneck layer containing a single neuron, which represents the nonlinear principal component u,

$$u = f_2(\mathbf{w}^{(x)} \cdot \mathbf{h}^{(x)} + \overline{b}^{(x)})\,. \tag{B.2}$$

The transfer function f_1 is generally nonlinear (usually the hyperbolic tangent or the sigmoidal function, though the exact form is not critical), while f_2 is usually taken to be the identity function.

Next, a transfer function f_3 maps from u to the final hidden layer (the decoding layer) $\mathbf{h}^{(u)}$,

$$h_k^{(u)} = f_3((\mathbf{w}^{(u)}u + \mathbf{b}^{(u)})_k)\,, \tag{B.3}$$

$(k = 1, \ldots, m)$; followed by f_4 mapping from $\mathbf{h}^{(u)}$ to $\mathbf{x}'$, the output column vector of length

l, with

$$x'_i = f_4((\mathbf{W}^{(u)}\mathbf{h}^{(u)} + \overline{\mathbf{b}}^{(u)})_i)\,. \tag{B.4}$$

The cost function $J = \langle \|\mathbf{x} - \mathbf{x}'\|^2 \rangle$ is minimized by finding the optimal values of $\mathbf{W}^{(x)}$, $\mathbf{b}^{(x)}$, $\mathbf{w}^{(x)}$, $\overline{b}^{(x)}$, $\mathbf{w}^{(u)}$, $\mathbf{b}^{(u)}$, $\mathbf{W}^{(u)}$ and $\overline{\mathbf{b}}^{(u)}$. The MSE between the NN output $\mathbf{x}'$ and the original data $\mathbf{x}$ is thus minimized. The NLPCA was implemented using the hyperbolic tangent function for f_1 and f_3, and the identity function for f_2 and f_4, so that

$$u = \mathbf{w}^{(x)} \cdot \mathbf{h}^{(x)} + \overline{b}^{(x)}\,, \tag{B.5}$$

$$x'_i = (\mathbf{W}^{(u)}\mathbf{h}^{(u)} + \overline{\mathbf{b}}^{(u)})_i\,. \tag{B.6}$$

Furthermore, the normalization conditions is adopted: $\langle u \rangle = 0$ and $\langle u^2 \rangle = 1$. These conditions are approximately satisfied by modifying the cost function to

$$J = \langle \|\mathbf{x} - \mathbf{x}'\|^2 \rangle + \langle u \rangle^2 + (\langle u^2 \rangle - 1)^2\,. \tag{B.7}$$

The total number of (weight and bias) parameters used by the NLPCA is $2lm + 4m + l + 1$, though the number of effectively free parameters is two less due to the constraints on $\langle u \rangle$ and $\langle u^2 \rangle$.

The choice of m, the number of hidden neurons in both the encoding and decoding layers, follows a general principle of parsimony. A larger m increases the nonlinear modelling capability of the network, but could also lead to overfitted solutions (i.e. wiggly solutions which fit to the noise in the data). If f_4 is the identity function, and $m = 1$, then (B.6) implies that all x'_i are linearly related to a single hidden neuron, hence there can only be a linear relation between the x'_i variables. Thus, for nonlinear solutions, $m \geq 2$ is needed. It is also possible to have more than one neuron at the bottleneck layer. For instance, with two bottleneck neurons, the mode extracted will span a 2-D surface instead of a 1-D curve.

The nonlinear optimization was carried out by the MATLAB function 'fminu', a quasi-Newton algorithm. Because of local minima in the cost function, there is no guarantee that the optimization algorithm reaches the global minimum. Hence a number of runs with random initial weights and bias parameters was made. Also, 20% of the data was randomly selected as validation data and withheld from the training of the NNs. Runs where the MSE was larger for the validation dataset than for the training dataset were rejected to avoid overfitted solutions. Then the run with the smallest MSE was selected as the solution.

In general, the most serious problem with NLPCA is the presence of local minima in the cost function. As a result, optimizations started from different initial parameters often converge to different minima, rendering the solution unstable or nonunique. Regularization of the cost function by adding weight penalty terms is an answer.

The purpose of the weight penalty terms is to limit the nonlinear power of the NLPCA, which came from the nonlinear transfer functions in the network. The transfer function tanh has the property that given x in the interval $[-L, L]$, one can find a small enough weight w, so that $\tanh(wx) \approx wx$, i.e. the transfer function is almost linear. Similarly, one can choose a large enough w, so that tanh approaches a step function, thus yielding Z-shaped solutions. If the use of excessive weights is penalized, the degree of nonlinearity can be limited in the NLPCA solution. This is achieved with a modified cost function

$$J = \langle \|\mathbf{x} - \mathbf{x}'\|^2 \rangle + \langle u \rangle^2 + (\langle u^2 \rangle - 1)^2 + P \sum_{ki} (W_{ki}^{(x)})^2 , \tag{B.8}$$

where P is the weight penalty parameter. A large P increases the concavity of the cost function, and forces the weights $\mathbf{W}^{(x)}$ to be small in magnitude, thereby yielding smoother and less nonlinear solutions than when P is small or zero. Hence, increasing P also reduces the number of effectively free parameters of the model.

The percentage of the variance explained by the NLPCA mode is simply

$$100\% \times \left(1 - \frac{\langle \|\mathbf{x} - \mathbf{x}'\|^2 \rangle}{\langle \|\mathbf{x} - \overline{\mathbf{x}}\|^2 \rangle}\right), \tag{B.9}$$

with $\overline{\mathbf{x}}$ being the mean of $\mathbf{x}$.

In effect, the linear relation $u(t) = \mathbf{a} \cdot \mathbf{x}(t)$ in PCA is now generalized to $u = f(\mathbf{x})$, where f can be any nonlinear continuous function representable by a feed-forward NN mapping from the input layer to the bottleneck layer; and instead of $\langle \|\mathbf{x}(t) - \mathbf{a}u(t)\|^2 \rangle$, $\langle \|\mathbf{x} - \mathbf{g}(u)\|^2 \rangle$ is minimized. The residual, $\mathbf{x} - \mathbf{g}(u)$, can be input into the same network to extract the second NLPCA mode, and so on for the higher modes.

That the classical PCA is indeed a linear version of this NLPCA can be readily seen by replacing all the transfer functions with the identity function, thereby removing the nonlinear modelling capability of the NLPCA. Then the forward map to u involves only a linear combination of the original variables as in the PCA.

With the NLPCA, for a given value of the NLPC u, one can map from u to the PCs. This is done by assigning the value u to the bottleneck neuron and mapping forward using the second half of the network in Fig. B.1a. Each of the PCs can be multiplied by its associated PCA (spatial) eigenvector, and the three added together to yield the spatial pattern for that particular value of u. Unlike PCA which gives the same spatial anomaly pattern except for changes in the amplitude as the PC varies, the NLPCA spatial pattern generally varies continuously as the NLPC changes. Fig. B.2 is an example of NLPCA for the combined SST and WS anomalies in the tropical Pacific. The detailed procedure was given in Section 2.4.1.

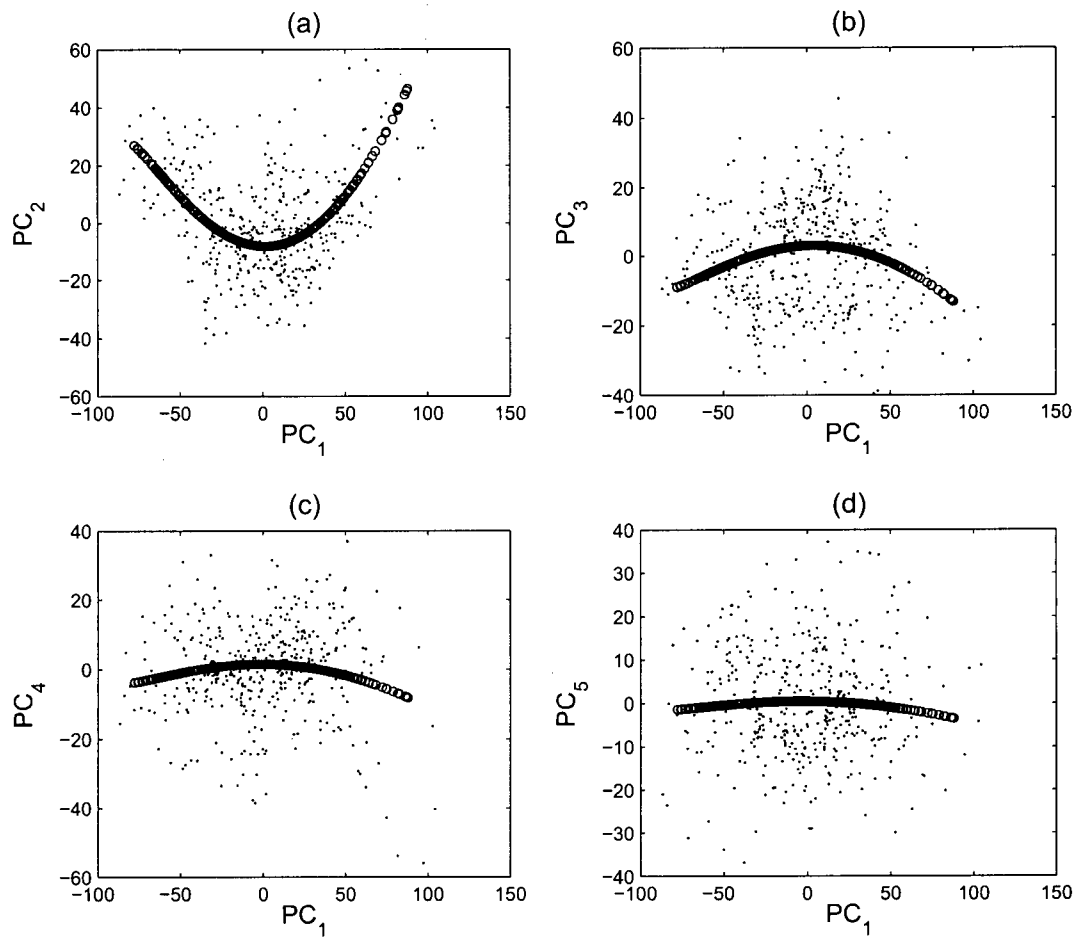

Figure B.2: First NLPCA mode for the combined SST and WS anomalies in the tropical Pacific (125°E-70°W, 30°S-30°N) during 1961-1995. The first NLPCA mode is indicated by the (overlapping) small circles, with the input data shown as dots. The input data were the first six PCs from combined PCA of the SST and WS anomalies (with each variable first normalized by its standard deviation). The NLPCA solution is shown projected onto (a) the PC1-PC2 plane, (b) the PC1-PC3 plane, (c) the PC1-PC4 plane, and (d) the PC1-PC5 plane.

B.2 Closed curves

The NLPCA is capable of finding a continuous open curve solution, but there are many geophysical phenomena involving waves or quasi-periodic fluctuations, which call for a continuous closed curve solution. Kirby and Miranda (1996) introduced a NLPCA with a circular node at the network bottleneck [henceforth referred to as the NLPCA(cir)], so that the nonlinear principal component (NLPC) as represented by the circular node is an angular variable A, and the NLPCA(cir) is capable of approximating the data by a closed continuous curve. Fig. B.1b shows the NLPCA(cir) network, which is almost identical to the NLPCA of Fig. B.1a, except at the bottleneck, where there are now two neurons p and q constrained to lie on a unit circle in the p-q plane, so there is only one free angular variable A, the NLPC.

At the bottleneck in Fig. B.1b, analogous to u in (B.5), the pre-states p_o and q_o is calculated by

$$p_o = \mathbf{w}^{(x)} \cdot \mathbf{h}^{(x)} + \overline{b}^{(x)}, \quad \text{and} \quad q_o = \tilde{\mathbf{w}}^{(x)} \cdot \mathbf{h}^{(x)} + \tilde{b}^{(x)}, \tag{B.10}$$

where $\mathbf{w}^{(x)}, \tilde{\mathbf{w}}^{(x)}$ are weight parameter vectors, and $\overline{b}^{(x)}$ and $\tilde{b}^{(x)}$ are bias parameters. Let

$$r = (p_o^2 + q_o^2)^{1/2}, \tag{B.11}$$

then the circular node is defined with

$$p = p_o/r, \quad \text{and} \quad q = q_o/r, \tag{B.12}$$

satisfying the unit circle equation $p^2 + q^2 = 1$. Thus, even though there are two variables p and q at the bottleneck, there is only one angular degree of freedom from A (Fig. B.1b), due to the circle constraint. The mapping from the bottleneck to the output proceeds as in Appendix A, with (B.3) replaced by

$$h_k^{(u)} = \tanh((\mathbf{w}^{(u)} p + \tilde{\mathbf{w}}^{(u)} q + \mathbf{b}^{(u)})_k). \tag{B.13}$$

When implementing NLPCA(cir), *Hsieh* [2001a] found that there are actually two possible configurations: (i) A restricted configuration where the constraints $\langle p \rangle = 0 = \langle q \rangle$ are applied, and (ii) a general configuration without the constraints. With (i), the constraints can be satisfied approximately by adding the extra terms $\langle p \rangle^2$ and $\langle q \rangle^2$ to the cost function. If a closed curve solution is sought, then (i) is better than (ii) as it has effectively two fewer parameters. However, (ii), being more general than (i), can more readily model open curve solutions like a regular NLPCA. The reason is that if the input data mapped onto the p-q plane covers only a segment of the unit circle instead of the whole circle, then the inverse mapping from the p-q space to the output space will yield a solution resembling an open curve. Hence, given a dataset, (ii) may yield either a closed curve or an open curve solution. Its generality comes with a price, namely that there may be more local minima to contend with. The number of parameters is $2lm + 6m + l + 2$, though under configuration (i), the number of effectively free parameters is two less, due to the imposed constraints. Unlike NLPCA which reduces to PCA when only linear transfer functions are used, NLPCA(cir) does not appear to have a linear counterpart. The NLPCA(cir) analysis is shown in Fig. B.3 for the combined SST, zonal surface current and sea level height in the tropical Pacific. The detailed procedure was given in Section 4.2.

B.3 References

Bishop C. M., 1995: Neural Networks for Pattern Recognition, *Clarendon Press*, 482 pp.

Hsieh W. W., 2004: Nonlinear multivariate and time series analysis by neural network methods. *Rev. Geophys.*, 42, RG1003. DOI:10.1029/2002RG000112.

Kirby M. J. and R. Miranda, 1996: Circular nodes in neural networks. *Neural Comp.*, 8,

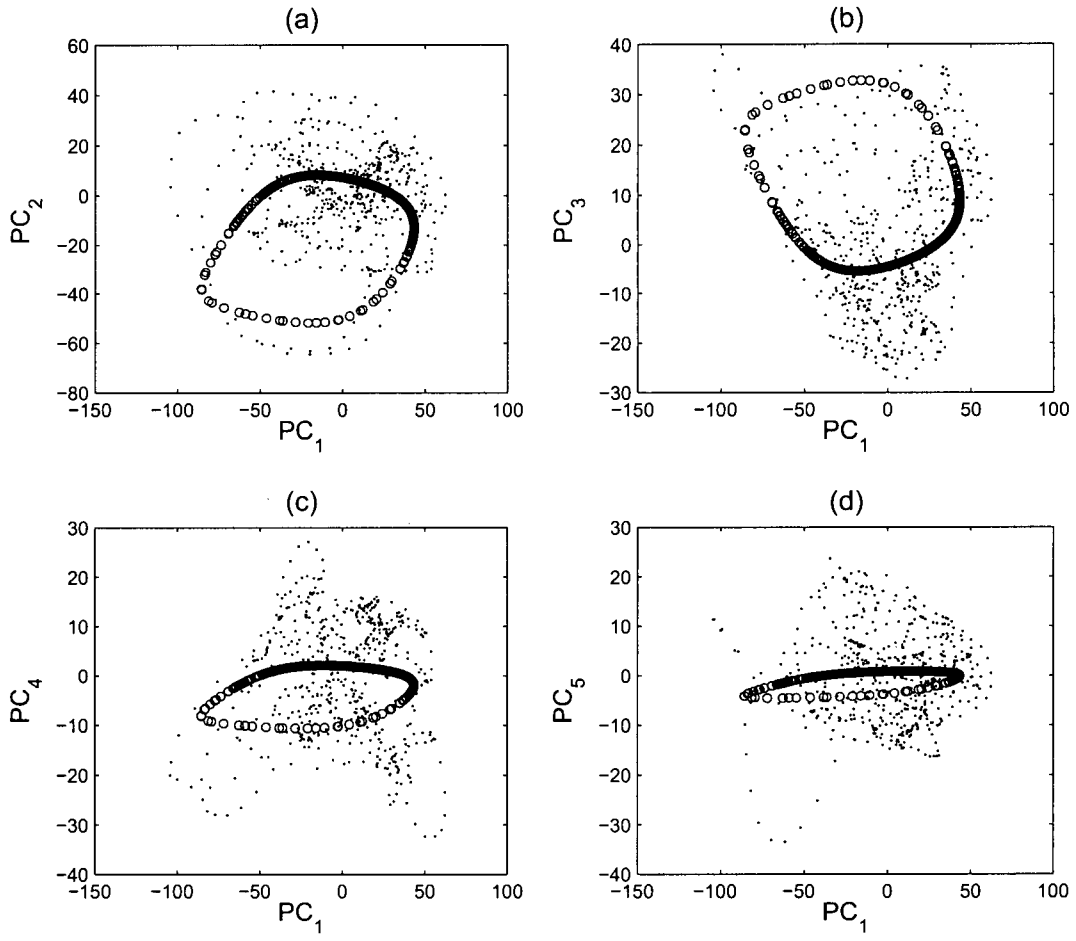

Figure B.3: First NLPCA(cir) mode from the combined SST, zonal surface current and sea level height anomalies in the tropical Pacific (120°E-70°W, 20°S-20°N) during 1958-2001. The first NLPCA(cir) mode is indicated by the (overlapping) small circles, with the input data shown as dots. The input data were the first six PCs from a combined PCA of the SST, zonal surface current and sea level height anomalies (with each variable first normalized by its standard deviation). The NLPCA(cir) solution is a closed curve in the six-dimensional PC space. The NLPCA(cir) solution is shown projected onto (a) the PC1-PC2 plane, (b) the PC1-PC3 plane, (c) the PC1-PC4 plane, and (d) the PC1-PC5 plane.

390-402.

Kramer M. A., 1991: Nonlinear principal component analysis using autoassociative neural networks. *AIChE. J.*, 37, 233-243.